High-resolution spectroscopy and novel crystal-field methods for rare-earth based quantum information processing

S. P. Horvath

Department of Physics and Astronomy
University of Canterbury

UC
UNIVERSITY OF
CANTERBURY
Te Whare Wānanga o Waitaha
CHRISTCHURCH NEW ZEALAND
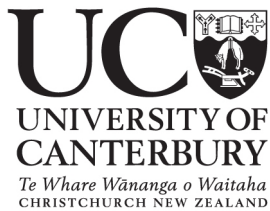
Submitted in partial fulfilment of the requirements for the degree of
Doctor of Philosophy in Physics

Under the supervision of M. F. Reid and J.-P. R. Wells

Abstract

Rare-earth doped insulators have been widely recognized as excellent candidate materials for optical quantum computing and information processing. This is principally due to a combination of optical coherence times of up to milliseconds and ground-state hyperfine coherence times of seconds exhibited by rare-earth $4f^N$ states. A key contender among rare-earth doped materials is $Er^{3+}:Y_2SiO_5$, for which homogeneous linewidths as narrow as 50 Hz have been reported, and for which transitions between the ground and first excited states fall within the 1.5 μm telecommunications wavelength band. However, attempts to utilize this material for spin-wave storage have been hampered by the complexity of the excited-state hyperfine structure, which inhibits the necessary theoretical work required to predict the location of zero first-order zeeman transitions. To address this, a novel crystal-field fitting method was developed to allow an accurate analysis of the C_1 point-group symmetry sites of Y_2SiO_5.

This work was complemented with spectral hole-burning spectroscopy, which revealed ground-state hyperfine level storage with a lifetime of 1.6 ± 0.4 seconds for the $^4I_{15/2}Z_1 \rightarrow {}^4F_{9/2}D_1$ transition. This type of storage time is uncharacteristic for erbium without an external magnetic field, since spin-flips of the unpaired electron in nearby Er^{3+} ions are typically understood to lead to fast hole filling.

The development process of the theoretical and experimental tools required to perform the above work enabled several additional investigations. In particular, the novel crystal-field fitting methods were applied to the S_4 site of $Ce^{3+}:LiYF_4$ and to the C_{2v} site of $Sm^{3+}:Na^+/Li^+:CaF_2/SrF_2$. These studies consisted of excellent tests for the developed methods yet also amounted to interesting investigations in their own respect.

Similarly, the experimental work afforded an opportunity to directly determine the hyperfine splittings of the $^5I_8Z_1 \rightarrow {}^5F_5D_1$ transition in $Ho^{3+}:KY_3F_{10}$. This was achieved using high-resolution excitation spectroscopy. Furthermore, the experimentally determined hyperfine structure could be accurately reproduced using a crystal field model.

Finally, a lifetime measurement of the $^6H_{7/2}$ state of $Sm^{3+}:LiYF_4$ was conducted. By utilizing an infrared free-electron laser, pico-second pump-probe spectroscopy allowed for a direct measurements of one of the shortest lifetimes of an RE^{3+}

doped insulator reported in the literature to date. This confirmed the previously suggested two-gradient modification required for the energy-gap law at very short time scales.

Acknowledgements

I would like to thank both of my supervisors Professor Mike Reid and Professor Jon-Paul Wells for always being available for discussion as well as guidance and encouragement throughout this thesis. I am thankful for the freedom that I was given to pursue my interests, while providing valuable input as required.

I would like to acknowledge the financial support provided by the University of Canterbury in the form of a Canterbury scholarship.

I am also very greatful to Dr. Philippe Goldner for the help he provided in getting various experiments working during his visit to the department. With out his expertise, getting the spectral hole-burning experiment to the state it is in now, would have been difficult.

Significant thanks also goes to the technical staff members of the department. Specifically, Stephen Hemmingsen, Wayne Smith and Rob Thirkettle for assistance with countless mechanical and instrumentation queries. Similarly, I am thankful to the electronics technical staff, Graeme MacDonald, Matt Panell, and Geoff Graham, and our IT manager Dr. Orlon Petterson, for assistance on numerous occasions.

Additionally, I am grateful to Professor Bryce Williamson from the Chemistry department for the use of his 7 Tesla superconducting magnet and the assistance that he provided in getting it up and running.

Thanks also goes to Dr. Alex Salkeld for his meticulous proof reading of this thesis.

I am also greatful to the fellow graduate students of the department of Physics and Astronomy for the countless interesting discussions, and the very supportive and helpful environment.

Finally, I would like to thank my parents, Paula and Erwin, without the support and encouragement of whom I would have been unlikely to have completed this work.

Contents

1

Introduction and motivation

Over the past two decades there has been a widespread effort to enhance classical computation and communication by incorporating quantum mechanical concepts [1]. These developments have been spurred by quantum algorithms that promise to vastly outperform even the largest classical computers employing only modest quantum computing hardware. Furthermore, proposed communication protocols based on quantum cryptography are, at least in principle, completely secure. The development of suitable algorithms, the associated information theory, and the required physical systems, are collectively referred to as quantum information processing (QIP).

Despite the comprehensive effort to physically realize such systems, scalable implementations have to date remained elusive [2]. One of the key obstacles faced by physical implementations of QIP systems is the difficulty of maintaining an ensemble of superposition states over a prolonged period of time, while simultaneously maintaining the ability to manipulate this ensemble to conduct specific QIP operations. This is referred to as the "closed box" requirement, and amounts to the demand that the physical system used to implement the quantum state must either by design have very few channels of interaction with the remaining universe, and/or actively dampen allowed interactions. The rate of degradation of superposition states by any interaction is quantified by the concept of coherence time, which, consequently, is one of the key indicators of merit for proposed QIP schemes.

Rare-earths doped into insulating crystals are well suited for QIP applications, since the f-shell electrons are shielded from interaction with the environment sur-

rounding the ion by the outer $5s$ and $5p$ electrons. In spectroscopic terms, this leads to exceptionally narrow homogeneous linewidths and correspondingly long coherence times for transitions between states of the $4f^N$ configuration [3]. Additionally, many rare-earth elements have isotopes with non-zero nuclear spin; thus, QIP schemes can be designed to exploit ground state nuclear spin states with lifetimes of days and coherence times of hours.

Rare-earth doped crystals have been used for a variety of applications in QIP [4]. However, the focus of this work is related to their use in optical quantum memories. The motivations for developing optical quantum memories are multifold; we begin with an example in optical quantum computing. Initial proposals of photonic quantum computation were limited by the scalability of strong nonlinear couplings between photons and atomic systems; however, in 2001 Knill, Laflamme, and Milburn proposed a scheme, henceforth referred to as the KLM scheme, that allowed for efficient and scalable quantum computation with linear optics [5]. To be physically implemented, the KLM scheme requires beam splitters, phase shifters, single photon sources, and high-efficiency single photon detectors. The most challenging of these components are on-demand single photon sources. Presently, single photon sources are implement by optically pumping a non-linear crystal to achieve spontaneous parametric down-conversion. However, the probabilistic nature of this process means that any QIP implementation that requires multiple single photon sources to fire simultaneously will run into severe scalability issues. This shortcoming can be overcome by coupling existing spontaneous parametric down-conversion single photon sources with optical quantum memories. Optical quantum memories are systems that can faithfully store and on-demand retrieve single photon wave packets [6]. Thus, a system can be realized in which quantum memories are probabilistically loaded with single photon sources, and then read out as required by the QIP algorithm.

Additionally, any practical quantum cryptography system will also require optical quantum memories. While entangled photons are easy to transmit on the scale of a typical laboratory, any distribution beyond a few hundred kilometers is impractical due to scattering and diffraction losses, be it in fiber or free-space [7, 8]. This limitation can be overcome by employing a network of quantum repeaters [9, 10]. Such a network is made up of a set of trusted nodes, which are used to perform entanglement swapping between pairs of single photons transmitted from

adjacent nodes. Thus, by repeating this process across all nodes of the network, entanglement can be achieved between the terminal points of the network. However, since a given pair of photons is unlikely to arrive at a node simultaneously, one requires an optical quantum memory to store the first photon until the arrival of the second photon allows for the entanglement swapping to be performed.

Furthermore, recent experiments in optical quantum memories using europium-doped yttrium orthosilicate have demonstrated coherence times of up to six hours, which opens the possibility of transporting quantum information by physically moving the memory, rather than by employing flying qubits to distribute the quantum information [11]. Coherence times of this length also open the possibility of fundamental tests of physics. For example, a quantum memory with a coherence time of days would enable tests of entanglement across distances several orders of magnitude greater than previously achieved, or tests of entanglement between two non-inertial frames of reference.

1.1 Rare-earth based optical quantum memories

Rare-earth doped crystals have been studied in great detail and have seen use in a remarkable number of optical applications, such as photoluminescence, solid state lasers, and scintillators. As a consequence, the technologies associated with both the material fabrication and suitable excitation sources are widely available and relatively cheap to manufacture [12]. As noted previously, the key property of rare-earths that makes them desirable for coherent applications are the very narrow homogeneous linewidths observed for $4f^N \rightarrow 4f^N$ transitions. Linewidths as narrow as 100 Hz have been observed in europium-doped yttrium orthosilicate [13] and 50 Hz in erbium doped yttrium orthosilicate [14]. The coherence properties of rare-earth doped insulating crystals were originally studied in the context of classical information storage and processing, a possibility first proposed by Mossberg [15]. As a result, much of the coherent spectroscopy, both in terms of material characterization and the development of experimental techniques, was conducted before rare-earths were first considered for application to QIP [16]. Furthermore, rare-earth doped crystals were successfully used for implementations of optical classical memories [17–20], and various optical signal processing systems [21, 22]. Some of these applications have reached an impressive level of maturity;

for example, the S2 corporation is marketing a 20 GHz bandwidth instantaneous spectrum analyzer [23–26]. It is this combination of impressive physical properties and the wealth of past work on these materials that makes rare-earth doped crystals ideal candidates for a variety of QIP applications.

Rare-earth based optical quantum memories were inspired by their classical counter-parts, which relied on photon-echo based storage schemes [17]. However it has been shown that traditional two- and three- pulse photon echoes cannot be used for faithfully storing and retrieving single photon wave packets, since the strong optical pulse used for rephasing the state vectors results in amplified spontaneous emission and thus yields inherently noisy photon echoes [27, 28].

In order to employ photon-echo techniques for quantum memories it is consequently necessary to achieve rephasing without the application of optical pulses. The first technique to achieve this stems from a proposal by Moiseev and Kröll in 2001 [29]. While the original proposal was applied to Doppler broadened atomic gases, a later proposal extended the principles to a modified form of photon echoes with rare-earth doped crystals [30]. This storage scheme relied on inhomogeneous broadening being induced externally; thus, by reversing the inhomogeneous broadening, the experimenter can, on demand, rephase the state vectors and yield an echo. This modified echo technique is referred to as controlled reversible inhomogeneous broadening (CRIB). Thus, even though the detuning and rephasing mechanism of ions differed from traditional photon echoes, many of the parameters of merit for a CRIB quantum memory remained unchanged, and it was possible to employ many of the techniques and materials developed for classical information processing with rare-earths. Alexander *et al*. achieved the first physical implementation of CRIB in Eu^{3+}:Y_2SiO_5 by Stark broadening the inhomogeneous profile using an external electric field. This technique has since been used to demonstrate storage efficiencies as high as 70% [31].

More recently, atomic frequency combs (AFC) have been used to to control the ion detuning in echo-based optical quantum memories [32, 33]. This scheme employs optical pumping to an auxiliary state to create a comb of sharp absorption features. This is followed by the absorption of the input photon which collectively excites the atoms that correspond to the fringes of the AFC. The periodicity in frequency space results in a controlled dephasing of the excited atoms and yields a collective emission when they rephase after a time determined by the AFC fringe

spacing. Since this process is intrinsic to the spectrally tailored absorption profile, there is no control of the time between absorption and re-emission once the AFC has been created. This can be remedied by transferring the excitation to a long-lived nuclear spin level of the ground state. Consequently the storage time becomes limited by the coherence time of the nuclear spin state. Additionally, since the readout is performed by the application of a further control pulse that returns the excitation to the excited state, the memory becomes on-demand.

The transfer of a quantum state from the excited state to the ground state nuclear spin levels is referred to as spin-wave storage. While it is essential in order to achieve on-demand AFC memories, it can also be employed to enhance the storage time of a CRIB memory [30, 34]. Spin-wave storage can vastly enhance the coherence time of a memory scheme, since many of the interactions present in the excited state are quenched for the ground-state. The primary remaining source of dechoerence is due to nuclear-spin flips. However, by employing a meticulously chosen magnetic field, the Zeeman interaction, to first order, can be eliminated for ground state hyperfine levels [35, 36]. These regions occur at anti-crossings of the Zeeman levels and are referred to as zero first-order Zeeman (ZEFOZ) transitions. Recently, Zhong *et al*. have achieved a remarkable 6 hour coherence time using this method in Eu^{3+}:Y_2SiO_5.

The objective of this thesis is to develop the necessary theoretical tools to accurately model both the ground and excited states for rare-earths in crystalline hosts commonly employed in QIP applications. This will enable a more comprehensive search of suitable ZEFOZ transitions and possibly allow a search for transitions that minimize other sources of spectral diffusion. At low temperatures, the primary source of dephasing for rare-earth doped crystals is due to nuclear spin flips. For this reason, the host material Y_2SiO_5 is ubiquitous in coherence applications, since oxygen has zero nuclear spin, silicon has a low isotopic abundance of nuclear spins, and yttrium has a small magnetic moment [13]. Y_2SiO_5 has two substitutional sites for rare-earth dopants, both of C_1 symmetry. This makes traditional crystal field fitting intractable, and such sites are generally analysed by using separate effective Hamiltonians for the ground and excited states.

In this thesis, we focus on creating an accurate crystal field model for the complete $4f^N$ configuration of Er^{3+}:Y_2SiO_5 both by novel crystal field fitting routines and by targeted experimental measurements. While the techniques developed have

potential to be of value for other materials, $Er^{3+}:Y_2SiO_5$ is an attractive choice as an initial goal for a number of reasons. Firstly, with a homogeneous linewidth of 50 Hz it has the longest coherence time of any optical transition observed in rare-earths to date [14]. Additionally, transitions between the $^4I_{15/2} \rightarrow {}^4I_{13/2}$ states are in the telecommunications wavelength region of 1.5 μm. Thus, quantum repeaters based on this material would be very practical for integration with existing telecommunication networks. This combination of very promising properties has lead to a widespread study of this material [37–46]. Secondly, with a nuclear spin of $I = 7/2$, the ^{167}Er isotope will result in a total of 240 holes and 57600 antiholes if all optical transitions are allowed [37]. As a consequence, fitting effective spin Hamiltonians separately to the ground and excited state is extremely challenging. As will be outlined below, some of these challenges can be met by moving to a crystal field Hamiltonian for the complete $4f^N$ configuration.

1.2 Crystal field calculations for low symmetry hosts

There are two formalisms commonly used to parameterize experimental spectra in rare-earth spectroscopy. The first approach consists of determining the effective Hamiltonian for the $4f^N$ configuration, referred to as a crystal-field Hamiltonian, which contains terms for the free-ion, the crystal-field, the Zeeman, the hyperfine, and the nuclear quadrupole interactions. By diagonalizing this Hamiltonian the entire energy level spectrum of a system can be characterized. Additionally, in contrast to ab initio calculations, the obtained parameters have a direct physical interpretation. These properties have established crystal field analysis as a standard tool for studying rare-earth doped crystals. However, fitting the required parameters can be rendered intractable by the many degrees of freedom of low point-group symmetry defect centers, such as those encountered in yttrium orthosilicate.

The second formalism consists of defining an effective Hamiltonian, referred to as a spin Hamiltonian, in a basis spanned by spin and nuclear angular momentum eigenstates. This is achieved by diagonalizing free-ion and crystal-field interactions in total angular momentum J, and treating the remaining interactions as second-order perturbations. Spin Hamiltonians are commonly employed for expressing magnetic and hyperfine interactions, as they substantially simplify the fitting procedure. Since the aforementioned QIP applications typically rely on

spin-wave storage in hyperfine levels, and because spin Hamiltonians are particularly well suited for parameterizing low symmetry materials, this second formalism is ubiquitous in the rare-earth QIP literature [47–52]. However, given that the magnetic response and the hyperfine structure is critically dependent on the crystal-field wavefunctions, the spin Hamiltonian parameters of different J-levels will generally be unique and therefore have to be determined by experiment.

As a result, we propose a crystal-field fitting scheme that enhances the accuracy of crystal-field parameters by fitting to spin Hamiltonian data in addition to the conventional energy level data.

1.3 Other applications of rare-earths in low symmetry hosts

While this thesis will focus on the development of both theory and experiment required to model $Er^{3+}:Y_2SiO_5$ due to its promising properties for optical quantum memories, rare-earth doped crystals have also been investigated for a variety of other QIP applications. Foremost among these applications is the use of rare-earths for carrying out both single- and multi- qubit operations. Here the idea is to store qubits in nuclear spin states and perform operations in the excited state. Experiments have been performed with qubits implemented as both ensembles of excited ions [53, 54], and single ions [55, 56]. Gate operations are performed by application optical pulse sequences with excited state qubits interacting by electric dipole-dipole coupling [57, 58]. More recently, stoichiometric crystals of $EuCl_3:6H_2O$, lightly co-doped with other rare-earths, were used to produce qubit ions with very strong electric dipole-dipole coupling [52, 59, 60]. The modelling schemes developed here are of interest to these applications, since an accurate crystal field Hamiltonian would allow one to simultaneously characterize both the ground and excited hyperfine states. Specifically for $EuCl_3:6H_2O$, the dopant site retains C_2 symmetry and hence would be difficult to fit by traditional means.

Finally, the techniques developed for performing crystal field fits for rare-earths in insulating crystals are also useful in a broader context. For example, recent work in which erbium ions were implanted into the channel of a FinFET transistor allowed for the detection of a single erbium ion [61]. The developed fitting procedure could be adapted to perform a crystal field fit using the unique data obtained

with the hybrid optical-electronic detection scheme.

1.4 Document outline

Chapter two of this thesis consists of a review of the theoretical material required to understand crystal-field calculations of $4f^N \to 4f^N$ transitions in rare-earth doped insulators. Subsequently, chapter three begins with a discussion of the computational aspect involved in performing crystal-field calculations. This includes both an outline of some of the existing code commonly used, as well as the programs developed as part of this thesis. After the initial technical discussion, this chapter applies the developed programs to two materials. The first is the fitting of an S_4 point-group symmetry crystal-field Hamiltonian using energy level in addition to g-value data. The second set of materials are $Sm^{3+}:Na^+/Li^+:CaF_2/SrF_2$ for which a C_{2v} point-group symmetry analysis is performed.

Chapter four contains both they key experimental as well as theoretical results of this thesis. Experimentally, the development and results of a spectral-hole burning experiment applied to the $^4I_{15/2} \to {}^4F_{9/2}$ transition of $Er^{3+}:Y_2SiO_5$. The theoretical work then details the process of applying the developed computational methods to the crystal-field analysis of the C_1 point-group symmetry sites of $Er^{3+}:Y_2SiO_5$.

Chapter five and six are primarily experimental chapters. Chapter five details the direct measurement of hyperfine splittings in $Ho^{3+}:KY_3F_{10}$, and the associated analysis. Finally, chapter six lies somewhat outside the scope of the remainder of the thesis and deals with a pico-second pump-probe measurement conducted with a free-electron laser in order to measure the lifetime of the $^6H_{7/2}$ multiplet in $Sm^{3+}:LiYF_4$.

2

The $4f^N$ configuration of rare-earth doped crystals

The rare-earth elements are defined as the lanthanide series of elements in addition to scandium and yttrium, which are chemically similar [62]. While strictly speaking part of the rare-earth series, spectroscopic studies exclude the elements lanthanum and lutetium, since they have an empty and complete $4f$ shell, respectively, and are thus optically inert. In this thesis, we will primarily deal with transitions between states of the $4f$ shell in trivalent rare-earth (RE^{3+}) ions doped into insulating crystalline hosts. Ions in the trivalent oxidation state have separated low-lying electron configurations which result in all valence electrons exclusively occupying the $4f$ shell. Consequently, trivalent rare-earths in crystalline hosts have an electron configuration of $[Xe]4f^N$, where N is the number of valence electrons. Additionally, since the radial extension of the $5s$ and $5p$ orbitals is greater than of the valence $4f$ shell, the f-electrons are shielded from the electric field due to the crystalline environment of the host material [16]. This leads to the very sharp $4f^N \rightarrow 4f^N$ transitions characteristic of RE^{3+} ion doped crystals. A key consequence of the very sharp intra-configurational transitions of the $4f$ shell is that they can be modeled with impressive accuracy using the quantum theory of atomic spectroscopy [63–66].

As will be explored in more detail below, the free-ion spectra are dominated by the Coulomb inter-electron repulsion and the spin-orbit interaction. The Coulomb inter-electron repulsion splits the $4f^N$ configuration into terms which are separated by approximately 10^4 cm^{-1}. The spin-orbit interaction further splits each

term into $2J + 1$ levels with splittings of the order of 10^3 cm^{-1}. These are labeled using term symbols of the form $^{2S+1}L_J$, where S is the total spin angular momentum, L is the total orbital angular momentum, and J is the total angular momentum. For historical reasons L is traditionally specified using the spectroscopic letter notation; that is, $L = 0, 1, 2, 3, \ldots$ is denoted by $S, P, D, F, \ldots$, respectively.

For rare-earths in crystalline hosts, the next largest interaction is the Stark splitting induced by the electric field of the crystalline host. This typically leads to splittings of the order of 100 - 1000 cm^{-1}. The degree to which the degeneracy of each $^{2S+1}L_J$ term is lifted due the crystal field is dependent on the point-group symmetry of the crystalline host. Provided the point-group symmetry of the host is sufficiently low, the $2J + 1$ degeneracy may be completely lifted for RE^{3+} ions with an even number of valence electrons. For Kramers ions, which are defined as ions with an odd number of valence electrons, the crystal field can at most lift the degeneracy of states up to doublets. In order to split the remaining Kramers doublets, one requires a time-asymmetric interaction, such as the Zeeman interaction due to an external magnetic field.

Since the crystal-field interaction is relatively small, it is possible to establish trends across the rare-earth series which, at least qualitatively, hold true for most host materials. The energy level splittings across the rare-earths are generally displayed in what is referred to as a Dieke diagram, which was first compiled for trivalent lanthanide ions in LaCl$_3$ [66]. Although the original diagram by Dieke did not include promethium, due to its nuclear instability, a later study by Carnall *et al*. provided the energy level structure of the complete RE^{3+}:LaCl$_3$ series [67]. This has lead the Dieke diagram to become an indispensable tool for the analysis of spectra of rare-earths. Figure 2.1 shows the updated version due to Carnall *et al*. While the original study calculated the free-ion and crystal-field splittings for a LaCl$_3$ host, the general trends shown in figure 2.1 hold true for other host materials.

Additional interactions that affect the electronic configuration are relativistic corrections and inter-configurational effects, hyperfine interactions that couple the nuclear spin and nuclear quadrupole to the spin of valence electrons, and the Zeeman interaction due to an external magnetic field. To account for this list of interactions, the following effective Hamiltonian will be employed to model the
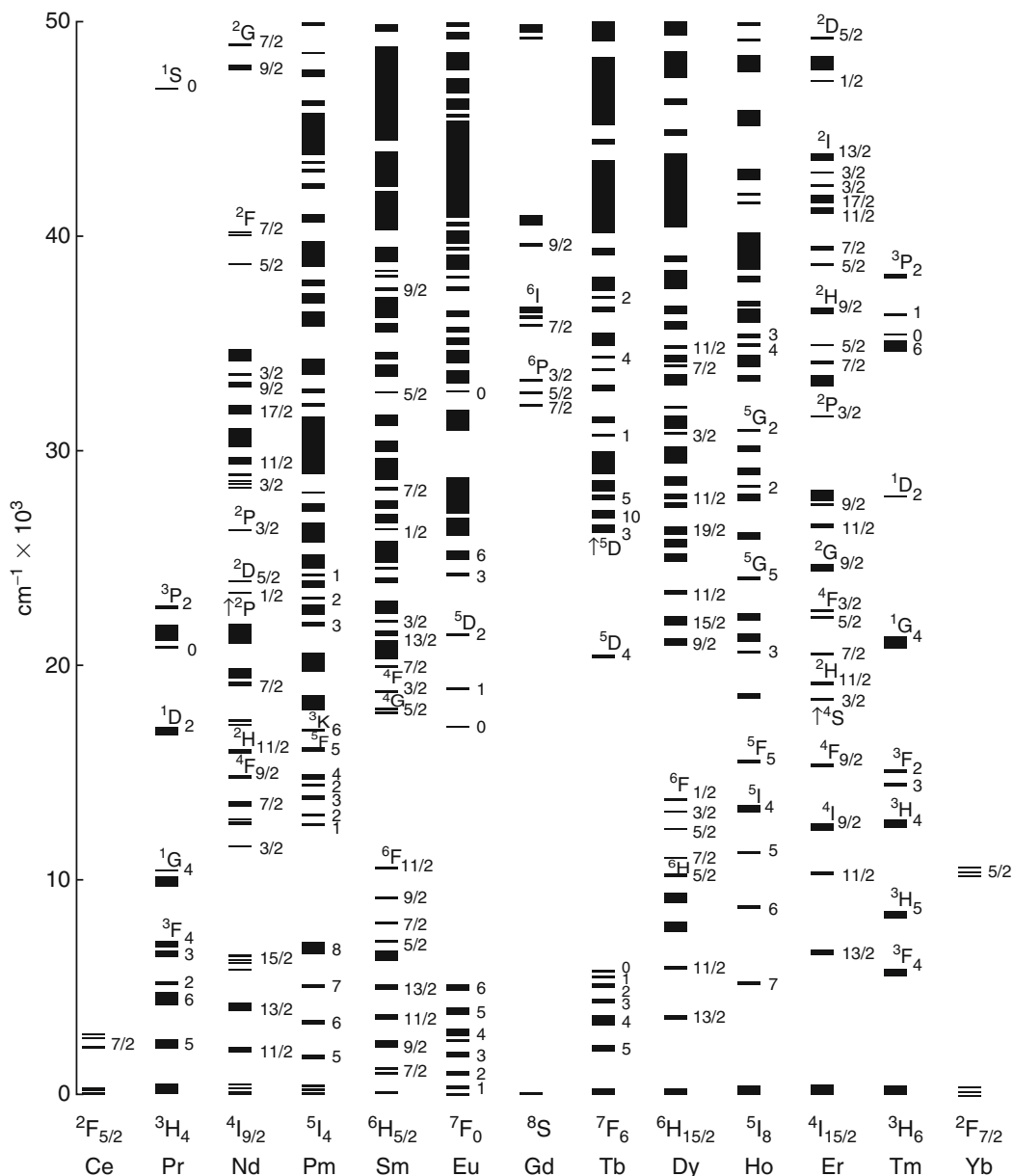
Figure 2.1: The Dieke diagram for elements of the lanthanide series in LaCl$_3$, based on theoretical free-ion and crystal-field splittings [67]. Figure reused, with permission, from reference [68].

complete $4f^N$ configuration:

$$H = H_{\mathrm{FI}} + H_{\mathrm{CF}} + H_{\mathrm{HF}} + H_{\mathrm{Q}} + H_{\mathrm{Z}}. \tag{2.1}$$

Here H_{FI} is the free-ion Hamiltonian which includes relativistic corrections and inter-configuration effects. H_{CF} is the crystal-field Hamiltonian, H_{HF} is the nuclear dipole hyperfine Hamiltonian, and H_{Q} is the nuclear quadrupole Hamiltonian. The final term, H_{Z}, is the Zeeman Hamiltonian. The effective Hamiltonian H is sometimes referred to as the crystal-field Hamiltonian. These respective splittings are shown schematically in figure 2.2.
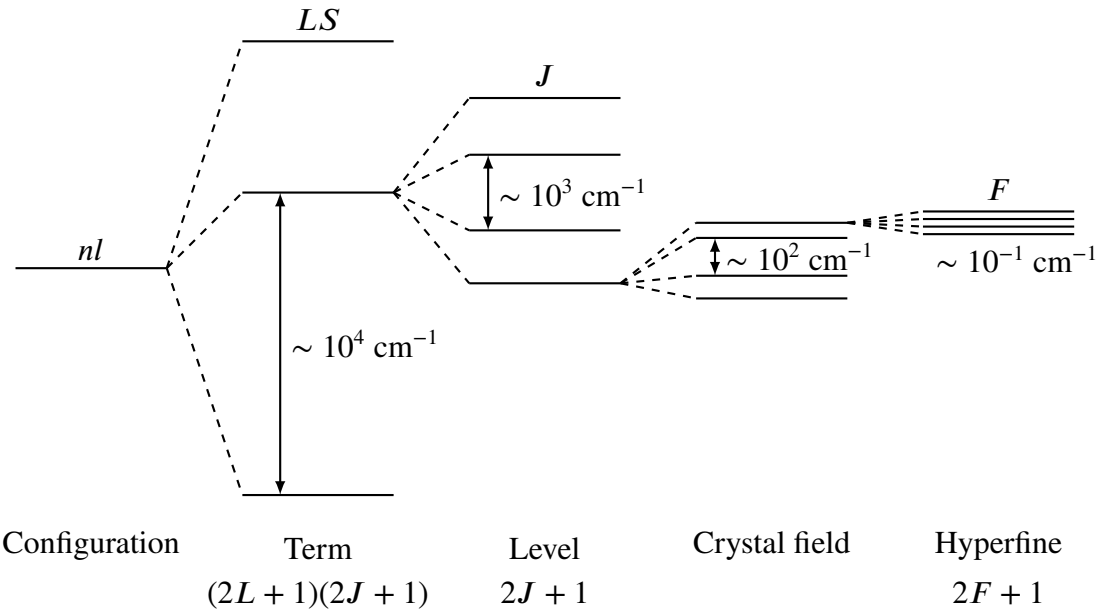
Figure 2.2: Figure adapted from reference [69]. The degeneracy of respective splittings is indicated where it is well defined. For the crystal field levels the residual degeneracy is dependent on the point-group symmetry specific to the host and is thus not shown.

An often used alternative method instead employs an effective Hamiltonian for modelling the Zeeman and hyperfine splittings of particular electronic state by working in a basis of effective spin [16, 70]. This effective Hamiltonian is referred to as a spin Hamiltonian. While group theoretically this method is only allowed for instances where a one-to-one correspondence can be established between the effective spin eigenstates and the basis of the irreducible representation of the crystal-field point-group symmetry, this method has been successfully applied to a much wider range of problems [71]. Furthermore, the fact that it allows for an accurate modelling of intricate Zeeman shifts and hyperfine splittings for very

low point-group symmetry hosts, has established the spin Hamiltonian method as a standard tool in the QIP literature.

We now proceed by outlining both the crystal field and spin Hamiltonian formalisms. We then describe how one can project from the basis of the Hamiltonian H to the spin Hamiltonian basis. This enables one to enhance the accuracy of parameters in H by harnessing magnetic and hyperfine data represented using the spin Hamiltonian formalism. The final section will also treat transition intensity calculations which are required for a direct comparison of a theoretical model with experimental spectra.

It should be pointed out that this chapter primarily amounts to a review of much of the standard literature on the subject of both crystal field and spin Hamiltonians. The material is a necessary prerequisite for the computational models described in chapter 3. However, in many instances technical details are treated minimally. For a more in-depth description of tensor operators, group representation theory, and perturbation theory, some of the classic texts on spectroscopy are Wybourne [65], Judd [64], and, more generally on atomic quantum mechanics, Weissbluth [69]. More modern resources include Henderson and Imbush [72] and the book edited by Liu and Jacquier [73]. For references specific to spin Hamiltonians, the classic text is Abragam and Bleaney [74], while Macfarlane and Shelby is an excellent resource applying spin Hamiltonians to coherent spectroscopy of rare-earths [16].

2.1 Crystal field Hamiltonian

2.1.1 The central field approximation

Following the standard treatment of N electron atoms [64, 65, 69], the non-relativistic atomic Hamiltonian for a point charge nucleus with atomic number Z is given by

$$H_0 = \sum_{i=1}^{N} \left[\frac{p_i^2}{2m} - \frac{Ze^2}{r_i} + \xi(r_i)(s \cdot l)_i \right] + \sum_{i>j} \frac{e^2}{r_{ij}}. \tag{2.2}$$

The first term represents the kinetic energy of the ith electron with momentum p_i and mass m, while the second term is the Coulomb attraction between the nucleus and the ith electron at a radius r_i. The third term is the spin-orbit interaction contribution of the ith electron, for spin angular momentum s and orbital angular

momentum l. The final term accounts for the repulsion between a pair of electrons, separated a distance r_{ij}.

Since the last term in equation (2.2) depends on the coordinates of both the ith and the jth electron, we cannot employ the usual separation of variables into angular and radial components. To proceed, we make two simplifying assumptions. Firstly, we assume that all electrons move independently of one another. Secondly, we assume that, to first order, the inter-electron repulsion experienced by the ith electron can be modeled by a spherically symmetric potential $U(r_i)$, generally referred to as the central field. Any remaining component of the inter-electron repulsion is then treated as a perturbation.

To make this precise, we define the central-field Hamiltonian of the form

$$H_0' = \sum_{i=1}^{N} \left[\frac{p_i^2}{2m} + U(r_i) \right].$$ \hfill (2.3)

Thus we may now take the difference between the atomic Hamiltonian (2.2) and the zero-order Hamiltonian (2.4) to obtain the perturbation potential for the asymmetric component of the inter-electron repulsion in addition to the spin-orbit interaction:

$$H_0 - H_0' = \sum_{i=1}^{N} \left[-\frac{Ze^2}{r_i} - U(r_i) \right] + \sum_{i<j}^{N} \frac{e^2}{r_{ij}} + \sum_{i=1}^{N} \xi(r_i)(s \cdot l)_i.$$ \hfill (2.4)

The first two terms in the above equation result in a constant shift of the entire configuration. Since we are only interested in the intra-configurational structure, these terms are dropped. Thus, provided $H_0 - H_0'$ is small, we can account for any component of the Coulomb electron repulsion that is not of the form $U(r_i)$ by using the following perturbation Hamiltonian

$$H_C = \sum_{i<j}^{N} \frac{e^2}{r_{ij}}.$$ \hfill (2.5)

This will henceforth by referred to as the Coulomb perturbation potential. The final term in equation (2.5) corresponds to the spin-orbit interaction, which we

define as the perturbation Hamiltonian of the form

$$H_{\text{SO}} = \sum_{i=1}^{N} \xi(r_i)(s \cdot l)_i. \tag{2.6}$$

We now proceed by solving the eigenvalue problem of the central-field Hamiltonian of

$$H_0' \Psi_0 = E_0 \Psi_0. \tag{2.7}$$

Since the central field potential $U(r_i)$ is assumed to be independent of other electrons, the eigenfunctions can be separated according to

$$\Psi_0 = \prod_{i=1}^{N} \psi_i(nlm_l) \text{ and } E_0 = \sum_{i=1}^{N} \varepsilon_i(nlm_l). \tag{2.8}$$

This yields N equations of the general form

$$\left[\frac{p^2}{2m} + U(r) \right] \psi(nlm_l) = \varepsilon(nlm_l)\psi(nlm_l). \tag{2.9}$$

Up to the potential function $U(r)$, equation (2.9) is the same as Schrödinger's equation for the hydrogen atom. Consequently, by separating into angular and radial components, we obtain

$$\varphi_{nlm_l}(r, \theta, \phi) = \frac{R_{nl}(r)Y_{lm_l}(\theta, \phi)}{r}. \tag{2.10}$$

Here $R_{nl}(r)$ is the radial eigenfunction and depends on the form of the central field potential $U(r)$. However, the angular components $Y_{lm}(\theta, \phi)$ are the standard spherical harmonics and match the angular part of the hydrogen atom solution. They are defined as

$$Y_{lm}(\theta, \phi) = (-1)^m \left[\frac{(2l+1)(l-1)!}{4\pi(l+m)!} \right]^{\frac{1}{2}} P_l^m[\cos(\theta)]e^{im\phi}, \tag{2.11}$$

where the associated Legendre polynomials can be evaluated using

$$P_l^m(x) = \frac{(1-x^2)^{\frac{1}{2}m}}{2^l l!} \frac{d^{l+m}}{dx^{l+m}}(x^2-1)^l. \tag{2.12}$$

Furthermore, in order to account for the two spin projections $m_s = \pm\frac{1}{2}$ of a spin $s = \frac{1}{2}$ electron, we multiply the orbital eigenfunctions (2.10) by the two-component spinor $\xi(s, m_s)$. Thus, equation (2.10) becomes

$$\psi_{\lambda_i}(r, \theta, \phi) = \frac{R_{nl}(r)Y_{lm_l}(\theta, \phi)}{r}\xi(s, m_s), \qquad (2.13)$$

where λ_i is defined as the set of one-electron quantum numbers $(nlm_l sm_s)$ of the ith electron.

Finally, the spin-orbital wavefunctions $\psi_{\lambda_i}(r, \theta, \phi)$ can be assembled into a totally-antisymmetric N-electron wavefunction. Such a wavefunction is most conveniently expressed by the use of Slater determinants [69], yielding

$$\Psi(\lambda_1, \lambda_2, \cdots, \lambda_N) = \frac{1}{\sqrt{N!}}\begin{vmatrix} \psi_1(\lambda_1) & \psi_2(\lambda_1) & \cdots & \psi_N(\lambda_1) \\ \psi_1(\lambda_2) & \psi_2(\lambda_2) & \cdots & \psi_N(\lambda_2) \\ \vdots & \vdots & & \vdots \\ \psi_1(\lambda_N) & \psi_2(\lambda_N) & \cdots & \psi_N(\lambda_N) \end{vmatrix}. \qquad (2.14)$$

Thus we have solved the zero-order problem and it now remains to perturbativly account for the Coulomb perturbation potential and the spin-orbit interaction.

2.1.2 Classification of states

In order to calculate the matrix elements of the perturbation Hamiltonians, H_{C} and H_{SO}, we must first define the angular momentum coupling scheme used for calculating the basis functions of the N atom system. We begin with the observation that the one-electron energies ε_{nl} are only dependent on the n and l quantum numbers. Hence, all pairs of equivalent nl are degenerate in energy. Thus, as was alluded to in the opening section of this chapter, in order for an nl electron configuration to be split we require the off-diagonal matrix elements of the Coulomb perturbation potential, H_{C}.

In order to calculate the matrix elements of H_{C} and H_{SO} we must define a suitable angular momentum basis. The choice of coupling is generally determined by the relative size of the inter-electron repulsion and the spin-orbit interaction. The two most common coupling schemes are referred to as LS coupling (or Russell-Saunders coupling) and jj coupling. For LS coupling, the orbital and spin angular

momentum operators are summed individually, that is

$$L = \sum_{i=1}^{N} l_i \quad \text{and} \quad S = \sum_{i=1}^{N} s_i. \tag{2.15}$$

The operators L and S are then further summed to obtain the total angular momentum operator

$$J = L + S. \tag{2.16}$$

As shown by Weissbluth [69], the operators corresponding to LS coupling state labels have the following commutation relationships with H_C and H_{SO}:

$$[H_C, L] = 0, \quad [H_C, S] = 0, \quad \text{and} \quad [H_C, J] = 0,$$

whereas

$$[H_{SO}, L] \neq 0 \quad \text{and} \quad [H_{SO}, S] \neq 0.$$

From this we can conclude that LS coupling is a sensible choice for atomic systems in which $H_{SO} \ll H_C$. Since the effect of the Coulomb perturbation potential decreases with respect to increasing atomic number, this condition fails for heavy elements. For elements with a dominant spin-orbit interaction, jj coupling becomes applicable. In this scheme, one sums over the orbital and spin angular momenta of individual electrons, such that one has the following operator

$$j = l + s, \tag{2.17}$$

This leads to the total angular momentum operator being defined according to

$$J = \sum_{i} j_i. \tag{2.18}$$

The reason why this choice of state labels is suitable for spin-orbit dominated atoms can again be made clear by evaluating the commutation relations with H_C and H_{SO}. From Weissbluth [69],

$$[H_{SO}, j] = 0, \quad [H_{SO}, J] = 0, \quad \text{and} \quad [H_C, j] \neq 0.$$

Thus, provided $H_C \ll H_{SO}$, j and J will be good quantum numbers. As noted previously, for the rare-earth series of elements we have $H_C \simeq H_{SO}$. Therefore, neither L and S, nor j can be considered to be good quantum numbers [75].

As a result, we will employ intermediate coupling in order to simplify the calculation. In this scheme one constructs an effective Hamiltonian by using an LS coupled basis. Then, by diagonalizing the Hamiltonian, a new set of eigenstates are found which are linear combinations of the LS eigenstates. Excluding inter-configurational coupling, the intermediate coupled eigenfunctions take the form

$$\Psi(nlJ) = \sum_{lS} a_{LSJ} |nl\,LSJ\rangle. \qquad (2.19)$$

Here the coupling coefficients a_{LSJ} are determined by diagonalizing the effective Hamiltonian in the LS basis [75].

We note that in order to completely define a state in the $4f^N$ configuration, one requires state labels of the form $|nl\tau LSJM\rangle$. To understand the requirement for the extra label, τ, it is necessary to determine the possible LS terms of a given $4f^N$ configuration. Towards this end we observe that a given l orbital has a total of $2(2l+1)$ states, which can be taken as basis for spanning the vector representation of the $U(14)$ group. By considering the subgroup decomposition of the $U(14)$, it becomes apparent that for some N there are degenerate states with equivalent L and S labels. It is the unique labelling of such states that requires the introduction of the extra quantum number τ, which is referred to as the seniority number. For details, the reader is referred to Wybourne [65] and Judd [64].

2.1.3 Free-ion matrix elements

We are now in a position to evaluate the matrix elements of H_C. This is achieved by recasting H_C in tensor operator form; following Judd [64], one obtains

$$H_C = e^2 \sum_k \frac{r_<^k}{r_>^{k+1}} \left(\sum_{i<j}^N C_i^{(k)} \cdot C_j^{(k)} \right). \qquad (2.20)$$

Here, $C_i^{(k)}$ are spherical tensor operators with the subscript i indicating that it is a function of the ith electron, while $r_<$ and $r_>$ are the lesser and greater element of $\{r_i, r_j\}$, respectively. Additionally, $C_q^{(k)}$ the spherical tensor operators are related

according to the relation spherical harmonics

$$C_q^{(k)} = \sqrt{\frac{4\pi}{2k+1}} Y_{kq}(\theta, \phi). \tag{2.21}$$

It is customary to split the matrix elements of H_C into angular and radial components according to

$$\langle l^N \tau LS | H_C | l^N \tau LS \rangle = \sum_k f_k(l, l) F^k(nl, nl). \tag{2.22}$$

The components $F^k(nl, nl)$ are the Slater integrals and for equivalent electrons nl are defined as

$$F^k(nl, nl) = e^2 \int_0^\infty \int_0^\infty \frac{r_<^k}{r_<^{k+1}} [R_{nl}(r_i) R_{nl}(r_j)]^2 \, \mathrm{d}r_i \, \mathrm{d}r_j. \tag{2.23}$$

While these can in principle be calculated using the Hatree-Fock method, for practical models of RE^{3+} ion doped crystals they are treated as experimental parameters. The angular component of the equation (2.20) can be shown to take the form [75]

$$f_k(l, l) = \frac{1}{2}(2l+1)^2 \begin{pmatrix} l & k & l \\ 0 & 0 & 0 \end{pmatrix}^2$$

$$\times \left[\frac{1}{2L+1} \sum_{\tau'L'} \left| \langle l^N \tau LS \, \| \, U^{(k)} \, \| \, l^N \tau' L' S' \rangle \right| - \frac{N}{2l+1} \right]. \tag{2.24}$$

The symmetry properties of the $3j$ symbols, which can be calculated directly using a closed form expression [76], restricts k to values $0, 2, 4, 6$ for $4f$ electrons. The values of the reduced matrix elements of the tensor operator U^k have been compiled by Nielson and Koster [77].

The matrix elements of the spin-orbit interaction, that is H_{SO}, can similarly be split into a radial component and an angular component

$$\left\langle nl^N \tau LSJM \middle| \sum_{i=1}^N \xi(r_i)(l \cdot s)_i \middle| nl^N \tau' L' S' J' M' \right\rangle = \zeta A_{SO}(nl), \tag{2.25}$$

where ζ is the spin-orbit interaction parameter. Again, while ζ can in principle be calculated using the Hartree-Fock method, in practice it is generally treated as a phenomenological parameter. The matrix elements of the angular component in equation (2.25) read [75]

$$A_{\text{SO}} = (-1)^{L+S'+J}\sqrt{(2l+1)(l+1)l}\,\delta_{J,J'}\delta_{M,M'}\begin{Bmatrix} L & S & J \\ S' & L' & 1 \end{Bmatrix}$$
$$\times \langle \tau L S \parallel V^{(11)} \parallel \tau'L'S'\rangle. \tag{2.26}$$

Edmonds provides a closed form expression for the $6j$ symbol [76], while the tensor operator $V^{(11)}$ can be looked up from the tables of Nielson and Koster [77].

While the two dominant interactions of the free-ion Hamiltonian are the electrostatic repulsion and the spin-orbit interaction, there are additional corrective terms for relativistic effects and inter-configuration interactions. We follow Liu [75] in defining the complete free-ion Hamiltonian by

$$H_{\text{FI}} = H_0 + \sum_{k=0,1,2,3} F^k f_k + \zeta A_{\text{SO}} + \alpha L(L+1) + \gamma G(R_7) + \beta G(G_2)$$
$$+ \sum_{i=2,3,4,6,7,8} T^i t_i + \sum_{i=0,2,4} M^i m_i + \sum_{i=2,4,6} P^i p_i. \tag{2.27}$$

The constants α, β, and γ parameterize two-body interactions (Trees parameters) whereas the constants T^i parameterize three-body interactions (Judd parameters), which arise due interactions between configurations that differ coordinates by not more than two and three electrons, respectively. In the case of two body interactions, these contributions can be described by matrix elements of the form $\sum_{i<j} U_i^{(k)} \cdot U_j^{(k)}$ [65], which for k even are accounted for by the Slater parameters, f_k. For k odd, the matrix elements of $\sum_{i<j} U_i^{(k)} \cdot U_j^{(k)}$ can be expanded in terms of $\alpha L(L+1)$, $\gamma G(R_7)$ and $\beta G(G_2)$, where $G(R_7)$ and $G(G_2)$ correspond to the eigenvalues of the Casimir operators of of the groups R_7 and G_2, respectively [65]. The last two terms, M^i and P^i, accommodate higher-order spin-dependent effects.

2.1.4 Crystal field matrix elements

We now consider the effect that the crystalline host has on the spectra of rare-earth ions. The primary influence is due to the electric field of the host material

the symmetry which depends on the crystalline structure of the material. For the $4f$ electrons, the crystal field is generally smaller than the effect of H_C and H_{SO} such that it can be treated as a perturbation on the free-ion states. In this thesis we employ the Wybourne normalisation for crystal-field parameters, which are defined by

$$H_{CF} = \sum_{k,q,i} B_q^k C_q^{(k)}(i). \tag{2.28}$$

Here the summation over i represents the contribution by each electron. The B_q^k parameters are phenomenological and are generally determined by fitting the eigenvalues of the crystal-field Hamiltonian to experimental values. $C_q^{(k)}$ are the previously defined spherical tensor operators (2.21). The values of k and q are determined by the site symmetry of the host crystal. In the case of no symmetry at all, this leads to a total of 27 independent crystal-field parameters. In higher symmetry centres many of these parameters can be omitted. For a detailed review of which parameters are required for various point-group symmetries, the reader is referred to Table 1.7 of Liu [75].

In order to evaluate the matrix elements of the spherical tensor operators in equation (2.28) one can employ the Wigner-Eckart theorem to recast the matrix elements in terms of doubly reduced matrix elements of the unit tensor. For the $4f^N$ configuration, this leads to matrix elements of the following form [75]:

$$\langle l\tau SLJM|H_{CF}|l\tau'S'L'J'M'\rangle = \sum_{k,q} B_q^k (-1)^{J-M} \begin{pmatrix} J & k & J' \\ -M & q & M' \end{pmatrix} D_J^k,$$

(2.29)

where

$$D_J^k = (-1)^{S+L'+J+k} \sqrt{(2J+1)(2J'+1)} \begin{Bmatrix} J & J' & k \\ L' & L & S \end{Bmatrix}$$

$$\times \langle l\tau SL \parallel U^{(k)} \parallel l\tau'S'L'\rangle (-1)^l (2l+1) \begin{pmatrix} l & k & l \\ 0 & 0 & 0 \end{pmatrix}. \tag{2.30}$$

As was the case for the free-ion matrix elements, here the $3j$ and $6j$ symbols can be evaluated directly from their respective closed form representations [76], whereas the unit tensor matrix elements can be obtained from the tabulated values by Nielson and Koster [77].

2.1.5 Magnetic and nuclear interactions

We now briefly outline the operators involved in Zeeman interactions due to an external magnetic field, the coupling of the nuclear dipole moment with the spin moment of valence electrons, and the interaction between the nuclear quadrupole and valence electrons.

The Zeeman Hamiltonian, H_Z, describes the coupling of the spin angular momentum of a valence electron with an external magnetic field of strength B. Following Judd [64], we define

$$H_Z = \mu_B \sum_i^N B \cdot (l_i + 2s_i), \qquad (2.31)$$

where μ_B is the Bohr magneton, and l_i and s_i are the orbital and spin angular momenta of the ith electron, respectively.

The term H_{HF} in equation (3.1) describes the hyperfine interaction of $4f^N$ electrons. This occurs for RE^{3+} elements with non-zero nuclear spin, since the nuclear spin angular momentum can couple to the spin angular momentum of valence electrons. Again following the development of Judd [64], the hyperfine Hamiltonian reads:

$$H_{HF} = \mu_B \left[\frac{\mu \cdot (l - s)}{r^3} + \frac{(\mu \cdot r)(s \cdot r)}{r^5} + \frac{8\pi}{3}\delta(r)\mu \cdot s \right], \qquad (2.32)$$

where $\mu = \gamma \hbar i$ is the nuclear angular-momentum operator and r is the position vector of the electron. Moreover, $\gamma = \mu_N g_I / \hbar$ with μ_N the nuclear magneton. The matrix elements of the hyperfine operator then take the form

$$\langle l\tau SLJMII_z | H_{HF} | l\tau'S'L'J'M'II_z \rangle$$

$$= a_l \sqrt{[J][J'][I](I+1)}\delta_{SS'}\delta_{II'} \times \left[(-1)^{L+S+M+I+M_I+1} \sqrt{[L](L+1)} \begin{Bmatrix} L & L' & 1 \\ J' & J & S \end{Bmatrix} \right.$$

$$\left. - (-1)^{J+M+L+I+M_I} \sqrt{30[L][L'][S](S+1)} \times \begin{pmatrix} L' & 2 & L \\ 0 & 0 & 0 \end{pmatrix} \begin{Bmatrix} S & S' & 1 \\ L & L' & 2 \\ J & J' & 1 \end{Bmatrix} \right]$$

$$\times \sum_{q=-1}^{1} (-1)^q \begin{pmatrix} J & 1 & J' \\ -M & q & M' \end{pmatrix} \begin{pmatrix} I & 1 & I' \\ -M_I & q & M'_I \end{pmatrix}, \qquad (2.33)$$

where the magnetic-dipole hyperfine parameter is defined as equation

$$a_l = 2\mu_B \gamma \hbar \langle r_i^{-3} \rangle. \tag{2.34}$$

Furthermore, we note the square bracket short-form employed throughout equation (2.33) has the definition

$$[x] = 2x + 1.$$

The final interaction we will discuss is the nuclear quadrupole interaction. This arises due to unpaired nucleons exhibiting a quadrupolar charge distribution which couples to the spin angular momentum of valence electrons. Following Wybourne [65], the matrix elements are given by

$$\langle l\tau SLJMIIF| \sum_{i=1}^{N} \left(C_i^{(2)} \cdot Q^{(2)} \right) |l\tau' S'L'JMIIF \rangle$$

$$= e^2 Q \langle r^{-3} \rangle \left(\frac{3/4K(K+1) - I(I+1)J(J+1)}{2I(2I-1)J(2J-1)} \right) \sqrt{\frac{8J(2J-1)}{(2J+3)(2J+1)(2J+1)}}$$

$$(-1)^{l+1}(2l+1) \begin{pmatrix} l & l & 2 \\ 0 & 0 & 0 \end{pmatrix} \langle \tau SLJ||U^{(2)}||\tau' S'L'J \rangle \delta_{SS'}$$

$$= a_Q X_J \left(\frac{3/4K(K+1) - I(I+1)J(J+1)}{2I(2I-1)J(2J-1)} \right), \tag{2.35}$$

where

$$a_Q = e^2 Q \langle r^{-3} \rangle, \tag{2.36}$$

is the electric-quadrupole coupling constant. In equation (2.35), the tensor Q is defined as a matrix element over the space of the nuclear coordinates evaluated with I maximized along the z-direction [65]:

$$Q = \langle II|r_n^2 C_n^{(2)}|II \rangle$$

$$= \begin{pmatrix} I & 2 & I \\ -I & 0 & I \end{pmatrix} \langle I||r_n^2 C_n^{(2)}||I \rangle. \tag{2.37}$$

2.2 Spin Hamiltonian

The Hamiltonian most widely used in the study of magnetic and hyperfine inter-
actions of a specific electronic state is the spin Hamiltonian. It is traditionally
defined as [16].

$$\mathscr{H} = [\mathscr{H}_{FI} + \mathscr{H}_{CF}] + [\mathscr{H}_{HF} + \mathscr{H}_{Q} + \mathscr{H}_{Z} + \mathscr{H}_{z}]. \qquad (2.38)$$

The two terms in the first set of parenthesis are the free-ion and crystal-field terms
as defined by equations (2.27) and (2.28), respectively. Provided the state under
consideration is sufficiently separated from adjacent states, the terms $\mathscr{H}_{FI}$ and $\mathscr{H}_{CF}$
amount to a constant off-set due to the spin-orbit and crystal-field interactions. The
precise hyperfine structure of the state in the presence of a magnetic field can then
be accurately characterized by the interactions listed in the second set of paren-
theses. These terms are, in turn, the nuclear hyperfine interaction, the nuclear
quadrupole interaction, the electronic Zeeman interaction, and the nuclear Zee-
man interaction [16]. The effective Hamiltonian $\mathscr{H}$ for specific electronic state is
referred to as the spin Hamiltonian. The details of the components that contribute
to the matrix elements of these interactions depends on whether one is dealing
with a Kramers ion, as well as the site symmetry of the host material.

For non-Kramers ions in a host of sufficiently low symmetry, the crystal-field
interaction completely lifts the degeneracy of each state. This leads to singlet
states that have a vanishing expectation value for the total angular momentum
operator J_z. Consequently, given the definitions (2.31) and (2.34), a singlet state
will, to first order, have zero Zeeman shift and no hyperfine splitting. However,
there is a second order effect due to mixing with nearby J levels which can be
described using the Hamiltonian [70]

$$\mathscr{H}' = -g_J^2 \mu_B B \cdot \Lambda \cdot B - (2A_J g_J \mu_B B \cdot \Lambda \cdot I + \mathscr{H}_{z}) - (A_J^2 I \cdot \Lambda \cdot I - \mathscr{H}_{Q})$$
$$= -g_J^2 \mu_B B \cdot \Lambda \cdot B + \mathscr{H}_{z}' + \mathscr{H}_{Q}', \qquad (2.39)$$

where

$$\Lambda_{\alpha\beta} = \sum_{n=1}^{2J+1} \frac{\langle n|J_\alpha|n'\rangle \langle n'|J_\beta|n\rangle}{E_{n'} - E_n}. \qquad (2.40)$$

In equation, (2.39) g_J is the Landé g-factor, μ_B is the Bohr magneton, and A_J is

the hyperfine coupling constant for this J level. $|n\rangle$ is the J level for which we are calculating matrix elements $\Lambda_{\alpha\beta}$ and $|n'\rangle$ are the other levels within the same $^{2S+1}L_J$ term. The second term in equation (2.39) is referred to as the second order Zeeman effect and has been combined with the nuclear Zeeman Hamiltonian to form $\mathscr{H}'_z$. Similarly, the fifth term has the same functional form as the nuclear quadrupole and is consequently referred to as the pseudo-quadrupole moment. In the second line of equation (2.39) we have combined this term with $\mathscr{H}_Q$ to obtain $\mathscr{H}'_Q$.

In the case of doublet states one requires a more general spin Hamiltonian of the form

$$\mathscr{H} = \mu_B B \cdot g \cdot S + I \cdot A \cdot S + \mathscr{H}'_Q + \mathscr{H}'_z. \tag{2.41}$$

It should be observed that the quadrupole and nuclear Zeeman Hamiltonians are the modified forms introduced in equation (2.39). That is, they include contributions due to the pseudo-quadrupole moment and the second order Zeeman effect.

Restricting the analysis to scenarios for which g is symmetric, the g tensor can be diagonalized by an Euler rotation R, and has the general form:

$$g = R(\alpha_g, \beta_g, \gamma_g) \begin{bmatrix} g_x & 0 & 0 \\ 0 & g_y & 0 \\ 0 & 0 & g_z \end{bmatrix} R^{\mathrm{T}}(\alpha_g, \beta_g, \gamma_g), \tag{2.42}$$

with g-values g_x, g_y, and g_z and Euler rotation parameters α_g, β_g, and γ_g. The orientation along which the g-tensor is diagonal is referred to as the principal axis of the Zeeman term. Similarly, the hyperfine parameter matrix A, and the parameter matrix associated with the quadrupole interaction $\mathscr{H}_Q$, can be diagonalized by an Euler rotation that aligns each term with their respective principal axis.

While equation (2.41) is the most general spin Hamiltonian, in the case of degenerate non-Kramers ions the perpendicular Zeeman and hyperfine interactions vanish. Consequently, only the contributions due to g_z, A_z, and Q_z have to be considered.

For impurity sites of C_2 or higher point-group symmetry, the principal axis orientation with respect to the crystal-field axes of each term in equation (2.38) can be inferred from the crystal-field symmetry. For further details on spin Hamiltonians, the reader is referred to reference [16].

2.3 Crystal field Hamiltonian to spin Hamiltonian projection

In chapter 3 we will discuss the fitting of crystal-field parameters using both energy level data and spin Hamiltonian parameter matrices, g, A, and Q. In order to enable this, we must calculate the theoretical spin Hamiltonian parameters for a given $4f^N$ configuration Hamiltonian, H. This projection can be cast in the language of effective operators, of which H is itself an example. We proceed by defining the $4f^N$ configuration as the complete space and the spin Hamiltonian basis as the model space. Then, if we have eigenstates of the complete Hamiltonian of the form

$$H|\lambda\rangle = E_\lambda|\lambda\rangle,$$

we require the matrix elements of the model space Hamiltonian, such that

$$\mathscr{H}|\lambda_0\rangle = E_\lambda|\lambda_0\rangle,$$

where $\mathscr{H}$ is the spin Hamiltonian defined by equation (2.38). Since the spin Hamiltonian method assumes that H_{FI} and H_{CF} are diagonal in J, the transformation to the spin Hamiltonian basis is given by

$$V = \sum_{\tau' L' S'} \langle nl\tau LSJ|H_{\mathrm{FI}} + H_{\mathrm{CF}}|nl\tau' L'S'J'\rangle. \qquad (2.43)$$

Having defined the projection to the model space, we are now in a position to transform the hyperfine and quadrupole operators according to

$$A_{\mathrm{eff}} = V^\dagger A V, \qquad (2.44)$$

for operator, A, and effective operator, A_{eff}. Thus, the projection can be performed by first diagonalizing $H_{\mathrm{FI}} + H_{\mathrm{CF}}$ and then transforming the operators we require to the spin Hamiltonian basis using equation (2.44).

2.4 Transition intensities

There are a number of mechanisms whereby an atomic system can interact with electromagnetic radiation. The most dominant contributions to observed transition intensities are due to electric dipole and magnetic dipole transitions. Further

higher order multipole transitions are also possible, however, these are generally sufficiently small to be neglected for all practical purposes. For intra-configurational $4f^N$ transitions, the matrix elements of the electric dipole operator are nominally zero, since the electric dipole operator is of odd parity. Nevertheless, it is possible for the crystal field to mix $4f^N$ wavefunctions with components from different configurations leading to mixed parity wavefunctions and consequently to non-zero electric dipole transition intensities between crystal-field levels. Such transitions are sometimes referred to as forced electric dipole transitions [66]. Generally, for intra-configurational $4f^N$ transitions of RE^{3+} ions in insulating crystals, the contribution of the forced electric dipole transitions and magnetic dipole transitions are of roughly equivalent magnitude. We now proceed by outlining how the transition strength of both of these operators can be calculated.

Following Reid [78], we define the electric dipole operator in tensorial form

$$- e D_q^{(1)} = -er C_q^{(1)}, \tag{2.45}$$

while the magnetic dipole operator reads

$$M_q^{(1)} = \frac{-e\hbar}{2mc}(L_q^{(1)} + 2S_q^{(1)}). \tag{2.46}$$

Here e is the electric charge, $\hbar$ is the reduced Planck constant, m is the electron mass, and c is the speed of light. Furthermore, q represents the polarization, and can take on values of $q = 0, \pm 1$.

While it is straightforward to evaluate the matrix elements of $M_q^{(1)}$ for an LS coupled basis of the $4f^N$ configuration, all matrix elements of $D_q^{(1)}$ will identically vanish for transitions between crystal-field levels. In order to calculate the forced electric dipole contribution, we define an effective operator using the parameterization due to Reid and Richardson [79], which reads

$$D_{\text{eff},q} = \sum_{\lambda,t,p} A_{tp}^\lambda U_{p+q}^\lambda (-1)^q \langle \lambda(p+q), 1-q|tp\rangle. \tag{2.47}$$

Here $\lambda = 2, 4, 6, t = \lambda - 1, \lambda, \lambda + 1$, and p dependent on the point-group symmetry of the crystal field. Additionally, A_{tp}^λ are parameters which can be calculated for a given site symmetry, and U_{p+q}^λ are unit tensors. For further details on effective

operators and $4f^N$ intra-configurational electric-dipole transitions, the reader is referred to Reid [78].

Having defined the dipole operators one can then proceed to calculate the matrix elements of electric and magnetic dipole operators for a given initial and final state, $\langle A_i|$ and $|B_j\rangle$, respectively. This leads to an electric dipole strength of

$$S_{AB,q}^{\mathrm{ED}} = \sum_{i,j} e^2 |\langle A_i | D_{\mathrm{eff},q} | B_j \rangle|^2, \tag{2.48}$$

and a magnetic dipole strength of the form

$$S_{AB,q}^{\mathrm{MD}} = \sum_{i,j} |\langle A_i | \mathrm{M}_q^{(1)} | B_j \rangle|^2. \tag{2.49}$$

Provided the polarization is linear, the electric and magnetic dipole strengths may be added. However, in the case of circularly polarized light, one may, for site symmetries with pure rotational operations, obtain differential absorption known as circular dichroism [78].

In order to relate the dipole strengths defined by equations (2.48) and (2.49) to experimental observables, one typically calculates the corresponding oscillator strength. These can be directly related to the absorbance of the material and are expressed in terms of the dipole strengths by [78]

$$f_{AB,q}^{ED} = \frac{2m\omega}{\hbar e^2} \frac{\chi_L}{n} \frac{1}{g_B} S_{AB,q}^{\mathrm{ED}}, \tag{2.50}$$

and

$$f_{AB,q}^{MD} = \frac{2m\omega}{\hbar e^2} n \frac{1}{g_B} S_{AB,q}^{\mathrm{MD}}. \tag{2.51}$$

Here n is the refractive index, g_B is the degeneracy of the initial state $|B\rangle$, and χ_L is a local correction factor accounting for the relative polariseability of the RE^{3+} ion compared to the host medium, which is defined according to

$$\chi_L = \left(\frac{n^2 + 2}{3} \right)^2. \tag{2.52}$$

Finally, for completeness, we note that the electric dipole and magnetic strengths

can be related to the Einstein A coefficients using the relations

$$A_{AB,q}^{\text{ED}} = \frac{1}{3}\frac{1}{4\pi\epsilon_0}\frac{4\omega^3}{\hbar c^3}n\chi_L\frac{1}{g_B}S_{AB,q}^{\text{ED}},\tag{2.53}$$

and

$$A_{AB,q}^{\text{MD}} = \frac{1}{3}\frac{1}{4\pi\epsilon_0}\frac{4\omega^3}{\hbar c^3}n^3\frac{1}{g_B}S_{AB,q}^{\text{MD}}.\tag{2.54}$$

All constants in the above two equations are in SI units.

3

Computational crystal-field fitting

In order to accurately model the $4f^N$ configuration of rare-earths in insulating crystals using the effective Hamiltonian (3.1), it is necessary to fit a number of phenomenological parameters using experimental observations. As outlined in chapter 2, they are the free-ion parameters of equation (2.27), the crystal-field parameters B_q^k, the hyperfine coupling strength a_l, and the nuclear quadrupole strength a_Q. These parameters are traditionally determined by least-squares fitting the eigenvalues of the Hamiltonian H to experimentally determined transition energies.

In this thesis, two further modes of fitting were developed in order to facilitate an accurate determination of these parameters for very low symmetry host materials. The first of these consists of a fit to energy level data as well as the spin Hamiltonian parameter matrices g, A, and Q. The second procedure that was developed fits to multiple sets of energy level data simultaneously. This enables, for example, the same set of transitions to be fitted for different orientations and strengths of an externally applied magnetic field. While only a single set of crystal-field parameters is fitted, each field strength would be represented as a separate Hamiltonian in the input program. This also enables calculations in which Hamiltonians composed of different interactions are fitted simultaneously as is particularly relevant when hyperfine data is only available for the ground state from electron paramagnetic resonance (EPR) measurements. This "multi-Hamiltonian" fit was developed since the procedure employing energy level and spin Hamiltonian data proved to be unsuitable for Kramers ions. More specifically, an unknown phase between Kramers doublet eigenvectors allows for spin Hamiltonian matrices that

correspond to asymmetric parameter matrices g, A, and Q. While these would result in the same eigenvalue spectrum upon diagonalization, when the parameter matrices are determined from experiment they are generally assumed to be symmetric. Thus, an implicit phase choice is made which results in a different set of parameters to those inferred from a given crystal-field Hamiltonian. However, by simultaneously fitting to multiple sets of energy levels that were synthetically generated using spin Hamiltonian data, it is possible to account for the magnetic response for arbitrary field orientations that is encoded in the spin Hamiltonian data, even for cases such as Kramers ions.

We will begin this chapter by outlining the F-shell empirical program suite, developed by M. F. Reid, which is capable of fitting the above phenomenological parameters using energy level data, as well as performing transition intensity calculations. This is followed by an outline of the `pycf` program, which was developed as part of this thesis. `pycf` consists of the new fitting routines discussed above, as well as various python programs related to the F-shell programs and a collection of scripts that facilitate spin Hamiltonian calculations. The remaining sections of this chapter consist of various incremental tests of the `pycf` program to solve progressively more challenging systems. Some of these calculations have yielded interesting results in their own respect.

3.1 The F-shell empirical programs

The F-shell empirical program suite was initially developed by M. F. Reid in 1983-1984. It is widely used for modelling the energy level structure and transition intensities of $4f^N \rightarrow 4f^N$ transitions as well as $4f^N \rightarrow 4f^{N-1}5d$ transitions.

The suite of programs is divided into the following parts: the preparation of matrix elements, the calculation of the energy level structure, including fitting to experimental energy levels, the calculation of electric-dipole and magnetic-dipole transition intensities, and the plotting of transition intensities. We will briefly discuss the function and work flow of these programs for crystal-field fitting and intensity calculations. The first set of programs is responsible for preparing the matrix elements of each term of the complete Hamiltonian (3.1). This initially involves the loading of the necessary reduced matrix elements specific to the electron configuration, using values sourced from Crosswhite [80]. Once the required

reduced matrix elements are parsed, routines referred to as SLJCALC and JMCALC are successively called to calculate the matrix elements in the SLJ and $SLJM$ basis, respectively.

Having determined these matrix elements they can then be employed in crystal-field and intensity calculations. The JMCALC program can be used to either calculate the complete set of matrix elements for the specified configuration, or a truncated set for a subset of terms. The use of truncated states can vastly increase performance for large systems (typically $N \geq 3$), particularly when an algorithm repeatedly diagonalizes the Hamiltonian as part of an optimization problem. The calculation of truncated matrix elements warrants some additional discussion. The approach taken follows that of Carnall *et al.* [81], and hinges on the assumption that H_{FI} and H_{CF} do not, necessarily, require an identical basis during a parameter fit. Thus, both the free-ion and the crystal-field matrix elements are generated in an intermediate coupled basis using eigenvectors of a previous diagonalization of H_{FI}, with approximate estimates for the free-ion parameters. These matrix elements can then be employed to simultaneously fit the free-ion and the crystal-field parameters, even though the crystal-field matrix elements are in a basis that was computed with estimated free-ion parameters. This leads to only minor deviations, provided the free-ion parameter estimate is within a few percent of the final result. This is a safe assumption for the vast majority of systems encountered. Once the matrix elements of all operators in equation (3.1) have been determined one can proceed by fitting the free-ion, crystal-field and hyperfine parameters. The F-shell empirical program suite provides the CFIT routine for this purpose. While some of the technical details of the implementation make it the most complex among the suite of programs, conceptually the calculation is quite simple. Using an initial set of parameters, the complete Hamiltonian (3.1) is diagonalized, which allows for an iterative optimization of the parameters by minimizing the difference between the calculated eigenvalues and experimentally observed transition energies.

The final set of programs are used to generate transition intensity spectra for both electric dipole and magnetic dipole transitions. The first program, VTRANS is used to transform the matrix elements of the U_l^λ and $M_q^{(1)}$ tensors, previously generated with JMCALC, into the crystal-field basis using a set of eigenvectors produced by CFIT. VTRANS additionally calculates the electric dipole operator coefficients A_{tp}^λ defined in equation (2.47). These transformed matrix elements are then passed to

the INTEN program which employs them to calculate the oscillator strengths and the dipole strengths for both forced electric dipole and magnetic dipole transitions. INTEN also produces a set of input files for the SPECTRUM routine which is a gnuplot based transition intensity plotting program. Thus, the F-shell empirical program suite allows for both fitting to crystal-field energy level data and calculation of transition intensity spectra.

3.2 The pycf program

A substantial portion of this thesis was concerned with developing software for fitting the crystal-field parameters in equation (2.28) for low point-group symmetry hosts. This was initially attempted by employing a python program in conjunction with CFIT. The python script was developed to automate the input data generation and calling of CFIT, as well as the calculation of spin Hamiltonian parameter matrices from CFIT output. This enabled for an optimization to be performed which ensured a fit to both the energy levels output by CFIT as well as the calculated spin Hamiltonian parameters. This approach, however, ran into severe performance issues when applied to test calculations for C_{2v} point-group symmetry materials, with run times of weeks even without the inclusion of hyperfine matrix elements. There were numerous factors that limited performance of this approach. Key among them were: the restriction to a single processing core due to python's global interpreter lock, heavy disk IO due to the text file based communication with CFIT, and that CFIT relied on an old compiler which could not exploit many of the optimizations available on modern hardware. Thus, this approach was abandoned in favor of a dedicated program which was developed to natively perform the required calculations.

The core of the developed program is a c99 library, called cfl, which handles both crystal-field calculations and spin Hamiltonian calculations, as well as the required optimization routines. By providing a native python interface to this library, it was possible to afford the user considerable flexibility, since it allowed the crystal-field routines to be employed in a more general scripting environment. Additionally, this made it trivial to interface cfl calculations with the ubiquitous python modules for scientific computing and plotting tools [82–84]. The cfl library is complemented by a collection of python modules which are designed

to automate spin Hamiltonian calculations as well as various utilities for loading $SLJM$ matrix elements and visualizing output from cfl.

We will briefly outline the implementation as well as modes of operation of the crystal-field library, cfl. This is followed by a description of the various systems that were employed to fit crystal-field parameters for progressively more challenging materials.

3.2.1 The crystal-field library cfl

The conceptual procedure employed by cfl is similar to CFIT in that the matrix elements of each term in equation (3.1) are multiplied by a coefficient and then the Hamiltonian is diagonalized to obtain the eigenvalue spectrum. However, in order to achieve the performance required to find minima in the solution landscape that results from the inclusion of spin Hamiltonian data, the implementation entailed considerable complexity. Briefly, all matrix elements are stored using the Hermitian compress sparse row storage (CSR, or sometimes CRS for compressed sparse row format) [85]. CSR only stores non-zero matrix elements and enables the use of efficient algorithms for scaling and adding sparse matrix elements. Once the matrix elements are stored, the adjacency graph of the Hamiltonian is searched using a depth-first graph traversal to find the connected components [86]. Having found the adjacency graph, the Hamiltonian can be re-arranged into block diagonal form by a set of CSR row and column swap routines. This ensures that, for matrices with degenerate eigenvalues, the diagonalization algorithm finds Hermitian eigenvectors. Furthermore, block diagonalization enables the diagonalization to be executed in parallel on a multi-core processor. All parallelization in cfl is implemented using OpenMP [87]. The eigenspectrum of each block is computed using the LAPACK zheevr function which implements the "Relatively Robust Representations" algorithm [88]. cfit can also perform the projection (2.44) to yield the Zeeman, hyperfine, and nuclear quadrupole spin Hamiltonian matrix elements. Thus, it is possible to perform a crystal-field fit which employs both experimental energy-level data and spin Hamiltonian parameter matrices. Sections 3.3 and 3.4 will employ this method to perform crystal-field fits for S_4 and C_{2v} point-group symmetry sites, respectively.

While the above outlined approach was successful for C_{2v} point-group sym-

metry materials, an application to fitting a C_1 crystal-field Hamiltonian for the Kramers material Er^{3+}:Y_2SiO_5 resulted in asymmetric spin Hamiltonian parameter matrices. This is due to a freedom of a phase between the eigenvectors of Kramers doublets, which is normally fixed by assuming a symmetric spin Hamiltonian parameter matrix when fitting to data. As was outlined earlier, this phase is generally implicitly fixed when spin Hamiltonian parameters are determined from experiment. Thus, in order to fit to Kramers materials the above fitting approach had to be abandoned. Instead of directly fitting to spin Hamiltonian parameters, the available parameters were employed to calculate the energy level structure at different magnetic field orientations. Then, `cfl` was adapted to fit to multiple Hamiltonians simultaneously, with each fixed field orientation being treated as an independent Hamiltonian. Since the number of Hamiltonians that contribute to the fitting was only limited by the resulting computation time, this approach afforded substantial flexibility compared to the spin Hamiltonian fitting. For example, while it has been possible to determine the ground state hyperfine splitting of Er^{3+}:Y_2SiO_5 using EPR spectroscopy, the number of hyperfine states has made an assignment of optically measured hyperfine transitions of the excited states very challenging. Thus, a separate effective Hamiltonian could be used which included the matrix elements of H_{HF} and H_Q, the eigenvalues of which were fit to synthetic eigenvalues generated from the spin Hamiltonian parameters.

Additionally, the outlined multi-Hamiltonian fit conveniently lends itself to parallelization, since each Hamiltonian can be diagonalized independently using separate threads and only the final χ^2 value has to be shared. Therefore, by employing an eight core processor, it is possible to simultaneously fit to many Hamiltonians without incurring an unreasonable performance penalty. Additionally, `cfl` is well suited for parallelization across a distributed memory system using OpenMPI [89]. This would enable the simultaneous diagonalization of hundreds of Hamiltonians on a modest Beowulf type cluster, with only minimal overhead due to communication between distributed memory nodes. However, since none of the problems encountered to date have required this type of performance, OpenMPI parallelization has yet to be implemented.

A further point of note is the optimization algorithm employed by `cfl` to perform the χ^2 minimization required for crystal-field fitting. Both the addition of spin Hamiltonian data, as well as the fitting to multiple Hamiltonians, results in a

solution space with numerous local minima. In order to correctly identify global solutions, `cfl` employs the basinhopping algorithm [90, 91]. This algorithm performs a random step, the maximum magnitude of which is specified at call time, followed by a local minimization. Then, the metropolis criterion [92] is applied to decide whether the algorithm should move to the newly found local minimum. Contrary to simulated annealing, the "temperature" used in the metropolis criterion is not reduced as the number of steps increases. Additionally, the maximum size of each step can be tuned such that a predefined percentage of steps is rejected. The application of the metropolis criterion also conveniently lends itself to a constraint parameter space optimization. If the solution of a local minimization is found to be outside a set of pre-defined bounds, it is automatically rejected.

In order to perform the local minimization, `cfl` provides an interface to wrap optimization algorithms from the GNU Scientific Library [93], as well as several of the NLopt nonlinear optimization library algorithms [94]. The basinhopping algorithm may also be substituted for any of the wrapped external optimization algorithms. This affords the user considerable flexibility in the minimization routine used, such that an appropriate choice is available for most problems. The API documentation of `pycf` has been included in appendix A.

3.3 Crystal field analysis of Ce^{3+}:LiYF$_4$

This section deals with an initial application of the spin Hamiltonian enhanced energy level fit. The method was applied to perform a crystal-field fit for trivalent cerium doped into a scheelite structure LiYF$_4$ single crystal. While cerium doped fluoride crystals have been of considerable interest in the past, both in the context of fundamental spectroscopy [95–97], as well as for applications such as UV lasers and scintillators [98, 99], a complete crystal-field analysis for intra-configurational $4f$ transitions had, to our knowledge, not been reported. Consequently, a combination of infrared absorption data, the published $Z_2\gamma_{5,6}$ state determined from high resolution $4f^{n-1}5d \rightarrow 4f^n$ emission spectra [100], and ground state electron-paramagnetic resonance (EPR) data [101] furnished an ideal initial candidate for testing the developed fitting routines.

LiYF$_4$ is a tetragonal crystal of the Scheelite structure (CaWO$_4$) having the C$_{4h}^6$ space group. In this material, each Li$^+$ ion is positioned at the center of a tetrahe-

dron of F^- ions and the Y^{3+} ions are each surrounded by eight F^- ions forming a tetragonal dodecaheron of D_{2d} point-group symmetry. However, due to to a 2.3˚ distortion of the F^- cage the point-group symmetry of the impurity site is reduced to S_4. Consequently, the initial test of `pycf` will be to determine the parameters of the crystal-field Hamiltonian of S_4 symmetry.

3.3.1 Experimental details

The experiments outlined in this section were performed in collaboration with J.-P. R. Wells. The contribution of the present author was the subsequent crystal-field analysis and the associated intensity calculation. Large single crystals of $LiYF_4$ doped with trivalent cerium were grown using the vertical Bridgman-Stockbarger technique. The furnace growth chamber was filled with greater than 1 atm pressure of highly purified argon gas to minimise evaporative losses. $LiYF_4$ incongruently melts at a temperature of 819 ˚C with a composition of 49 mol % YF_3 and 51 mol % LiF. As the growths were unseeded in graphite crucibles, the grown boules had to be oriented using Laue X-ray-diffraction photography in order to be used for spectroscopic studies.

Infrared absorption spectra were recorded at 0.25 cm^{-1} resolution using a Bio-Rad FTS 40 Fourier transform infrared spectrometer. The crystal samples were cooled by thermal conduction with the 10 K stage of a CTS LTS 0.1 closed cycle helium cryostat. Temperature control was achieved with a closed-loop PID adjusted current through a resistive heater placed at the back of the cold stage head.

3.3.2 Infrared absorption spectra

Figure 3.1 (a) shows the 10 K infrared absorption spectrum of a 4.3 mm thick sample of $LiYF_4$ doped with 0.5% Ce^{3+}. Transitions to the $^2F_{7/2}$ multiplet are observable in the 2000-3000 cm^{-1} region due to the spin-orbit splitting of the degenerate $4f^1$ configuration superimposed upon the crystal-field splitting of the excited multiplet. Under S_4 point-group symmetry the $J = 7/2$ multiplet is expected to break up into two states of $\gamma_{5,6}$ symmetry and another two states of $\gamma_{7,8}$ symmetry. As such, we label the crystal-field levels with the usual notation of a letter with a numerical subscript (Z for the ground multiplet and Y for the excited multiplet; Z_1 denoting the ground state, Z_2 the first excited state and so on)

and the appropriate irreducible representation, using the notation of Koster *et al*. [102]. All of the four expected transitions are clearly observed in figure 3.1 (a).
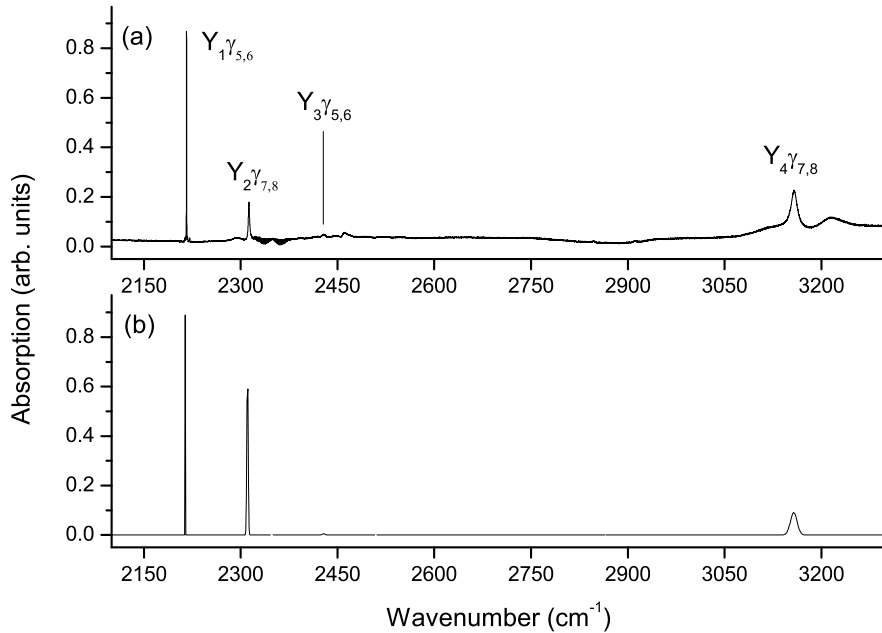
Figure 3.1: (a) 10 K infrared absorption spectrum of nominally unoriented Ce^{3+}:LiYF$_4$ showing the $^2F_{5/2} \rightarrow {}^2F_{7/2}$ transitions and (b) the simulated spectrum (see text for details).

The additional structure seen in figure 3.1 (a) is attributed to phonon sidebands of the $Z_1\gamma_{7,8} \rightarrow Y_1\gamma_{5,6}$ zero phonon electronic transition. This is consistent with phonon sidebands reported in previous optical studies of lanthanide-doped LiYF$_4$ (see for example [103]). The most prominent of these corresponds to the 248 cm^{-1} LiYF$_4$ TO mode [104]. Additional sharp peaks centered around 2350 cm^{-1} are residual atmospheric contamination observed as the CO$_2$ rotation-vibrational bands. These appear as a decrease in absorption due to an imperfect ratio of the background and the single beam absorption spectra by the FTIR spectrometer. Our infrared absorption results for Ce^{3+}:LiYF$_4$ are essentially in agreement with those reported in an earlier study [105], albeit that our data is obtained at 10 K the data in reference [105] was limited to 100 K.

3.3.3 Crystal-field analysis and simulated spectra

In order to unambiguously assign irreducible representations to the Ce^{3+} energy levels from the transitions observed in the infrared spectrum, a crystal-field analysis was performed, followed by a calculation of the expected transition intensities. To achieve this, we note that the energy of the $Z_2\gamma_{5,6}$ state has been determined to be 216 cm^{-1} from high resolution $4f^{n-1}5d \rightarrow 4f^n$ emission spectra [100] and the ground state magnetic g-values are known from EPR studies [101]. As such our analysis is based upon fits to both the experimental energy level data and the g-values.

The effective Hamiltonian describing the energy levels of the Ce^{3+} ions has the form

$$H = H_{\text{FI}} + H_{\text{CF}} + H_{\text{Z}}, \tag{3.1}$$

where H_{FI} corresponds to the free-ion term (and contains only the spin-orbit interaction), H_{CF} is the crystal-field Hamiltonian and H_{Z} is the Zeeman interaction. The parametric Hamiltonian for S_4 symmetry is given by:

$$\begin{aligned}
H_{CF} = &B_0^2 C_0^{(2)} + B_0^4 C_0^{(4)} + B_0^6 C_0^{(6)} + B_4^4(C_4^{(4)} + C_{-4}^{(4)}) \\
&+ B_4^6(C_4^{(6)} + C_{-4}^{(6)}) - iB_4^{6'}(C_4^{(6)} - C_{-4}^{(6)}),
\end{aligned} \tag{3.2}$$

where B_q^k are the usual one electron crystal-field parameters defined in section 2.1. In order to perform the fit, published values of the Pr^{3+}:LiYF$_4$ crystal-field parameters [106] were used as initial estimates for the optimization problem. The experimental and fitted energies, in addition to the g-values, are shown in table 3.1. The spin-orbit coupling constant and the S_4 crystal-field parameters obtained by the fitting process are given in table 3.2.

A good approximation to the experimental energy levels and g-values is obtained with crystal-field parameters consistent with that of other rare-earth ions in LiYF$_4$. Furthermore, the crystal-field parameters are consistent with those found for Ce^{3+}:LiYF$_4$ by Peijzel et al. [100], which were obtained by holding half of the crystal-field parameters fixed. Additionally, by altering the weighting of the contributions to the least-squares χ^2, it was possible to establish that an accurate fit to the g-values is essential in order to obtain crystal-field parameters that are consistent with the parameter trend established in reference [107]. A recent study

Table 3.1: The experimental and calculated energy levels, and ground state g-values for Ce³⁺ in LiYF₄. Energy levels are in cm⁻¹ with an uncertainty of ± 0.1 cm⁻¹.

State	Experimental	Calculated
$Z_1 \gamma_{7,8}$	0.0	1.5
$Z_2 \gamma_{5,6}$	216	213.8
$Z_3 \gamma_{7,8}$	-	414.4
$Y_1 \gamma_{5,6}$	2216.1	2215.5
$Y_2 \gamma_{7,8}$	2312.8	2312.1
$Y_3 \gamma_{5,6}$	2428.8	2430.1
$Y_4 \gamma_{7,8}$	3157.8	3158.6
$g_\parallel$	2.765	2.751
$g_\perp$	1.473	1.514

Table 3.2: The spin-orbit and S₄ symmetry crystal-field parameters for Ce³⁺ in LiYF₄.

Parameter	Fitted value (cm⁻¹)
ζ	626
B_0^2	298
B_0^4	-1328
B_4^4	-1282
B_0^6	-192
B_4^6	-1743
$B_4^{6'}$	693

[108] points out the significance of the contribution of ²F₇/₂ Kramers doublets to the ground state wavefunction and therefore to calculation of the g-values. For trivalent cerium, this can only occur through crystal-field J_z-mixing and therefore its significance varies in different host crystals. For example, our analyses show that in LiYF₄ a 1% wavefunction admixture occurs in this fashion; however, for the $C_{4v}(F^-)$ centers in CaF₂ and SrF₂ the ground state is a 100% pure $J = 5/2$ Kramers doublet.

Figure 3.1 (b) shows the simulated infrared absorption spectrum. The theoretical transition intensities were obtained by evaluating the matrix elements of the magnetic dipole operator using the wavefunctions calculated in section 3.3.3. This

allowed for the computation of the dipole strengths, and, by convolving the resulting individual Gaussian lineshapes of each transition, yielded the shown simulated spectrum. The full width at half maximum of individual Gaussians were estimated from the experimental spectrum.

Thus, by combining infrared absorption as well as previously measured high resolution inter-configurational emission and EPR data, we have performed a crystal-field analysis for the $4f$ levels of Ce^{3+} in $LiYF_4$. An excellent agreement is obtained for fits to the six experimentally determined energy levels as well as the ground state g-values, with the resultant crystal-field parameters in line with those for other lanthanide ions in this host crystal. An intensity analysis has been employed to confirm the irreducible representation assignments used in the fits, and has been found to yield a good agreement with the infrared absorption data to the $^2F_{7/2}$ multiplet.

3.4 Crystal field analysis of C_{2v} sites in Sm^{3+}:CaF_2/SrF_2

We now turn to apply the spin Hamiltonian enhanced energy level fitting method to lower point-group symmetry lanthanide sites. In particular, both magnetic and hyperfine EPR data was employed in order to create a crystal-field model for the orthorhombic sites in Li^+ and Na^+ ion charge compensated Sm^{3+} centers in co-doped CaF_2 and SrF_2 crystals. This yields a good agreement between theory and experiment, in addition to accurately modelling crystal distortions due to the differing ionic radii of Li^+ and Na^+.

The dominant defect structures of RE^{3+} doped CaF_2 and SrF_2 doped crystals has been established to be tetragonal C_{4v} symmetry centers and C_{3v} symmetry centers [109–111]. For both CaF_2 and SrF_2, charge compensation in the case of the C_{4v} center is achieved by a next nearest neighbor interstitial F^- ion located along the [100] direction. In the case of the C_{3v} center, the charge compensation mechanism is dependent on the host material. For CaF_2 crystals, the exact model of charge compensation is not completely certain [112], with some proposals containing F^- vacancies in the cube surrounding the RE^{3+} ion. For SrF_2 crystals, the C_{3v} center consists of an RE^{3+}-F^- dipole oriented such that the F^- ion is located in the next nearest neighbor position in the [111] direction.

In addition to these sites, less commonly observed cubic O_h centers have been

reported for both CaF_2 and SrF_2. The reason this center is typically not observed is since intra-configurational $4f^N$ electric-dipole transitions are forbidden for cubic symmetry substitutional sites. Consequently, such transitions are predominantly observed due to magnetic dipole interactions. The abundance of the relatively rare cubic centers has been shown to be enhanced by co-doping the host material with alkali Na^+ or Li^+ ions. Furthermore, using EPR studies, such co-doping has been shown to result in two additional substitutional sites [113, 114]. Most relevant to this work is a C_{2v} site resulting from a nearest neighbor alkali ion. In figure 3.2 we show the relative orientation of the C_{2v} symmetry axis with respect to the fluorine cage for the example of Sm^{3+}:Na^+:CaF_2/SrF_2. The third site that results from co-doping with alkali ions is a modified tetragonal center with an on-axis nearest neighbor alkali ion along the [200] direction.
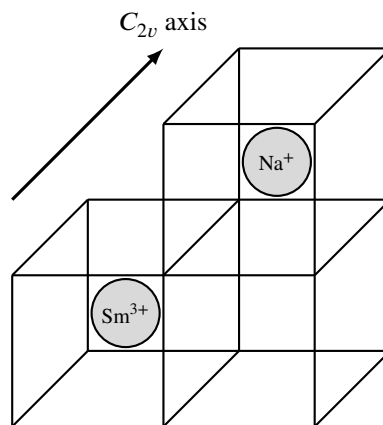
Figure 3.2: The C_{2v} symmetry axis is defined by the location of the substitutional RE^{3+} ion with respect to the co-doped alkali ion in a nearest neighbor F^- cage. The schematic indicates one such arrangement for the example of Sm^{3+}:Na^+:CaF_2/SrF_2.

Thus, in order to test the efficacy of the spin Hamiltonian enhanced crystal-field fit, we apply it to Li^+ and Na^+ ion charge compensated Sm^{3+} orthorhombic centers in co-doped CaF_2 and SrF_2 crystals. The many crystal-field levels of the low lying ^6H and ^6F terms [111], and since C_{2v} point-group symmetry ensures that the spin-Hamiltonian principal $\hat{z}$ axis is coincident with the corresponding crystal-field axis, makes these materials well suited for the investigations presented here.

The $4f^5$ configuration is appropriate for trivalent samarium which consists of

1001 two-fold degenerate electronic states. Of the available multiplets absorbing in the visible region, fluorescence is observed only from the $^4G_{5/2}$ term, the barycenter of which is near 18000 cm^{-1}. The ground multiplet is $^6H_{5/2}$ and fluorescence to all multiplets of the ^6H_J and ^6F_J terms could be observed with the exception of $^6F_{11/2}$.

The site selective spectroscopy for the C_{2v}(Na$^+$/Li$^+$) site of Sm^{3+} in alkaline-earth fluoride crystals was performed by J.-P. R. Wells but was not published due to the intractability of performing a crystal-field fit using only energy level data. The EPR studies were performed by M. Yamaga *et al*. While the magnetic *g*-values were previously published [114], the publication of the hyperfine data was also postponed due to the difficulty of the crystal-field analysis. Thus, this work is ultimately comprised of a site-selective spectroscopy experiment, a set of EPR measurements, and a detailed crystal-field analysis. Figure 3.3 (a) shows the broadband excitation spectrum of the $^4G_{5/2}$ multiplet for Sm^{3+}:Na$^+$:CaF$_2$. Both the cubic and the C_{2v} centers are clearly visible. Figure 3.3 (b) further details the C_{2v} center using site selective excitation.
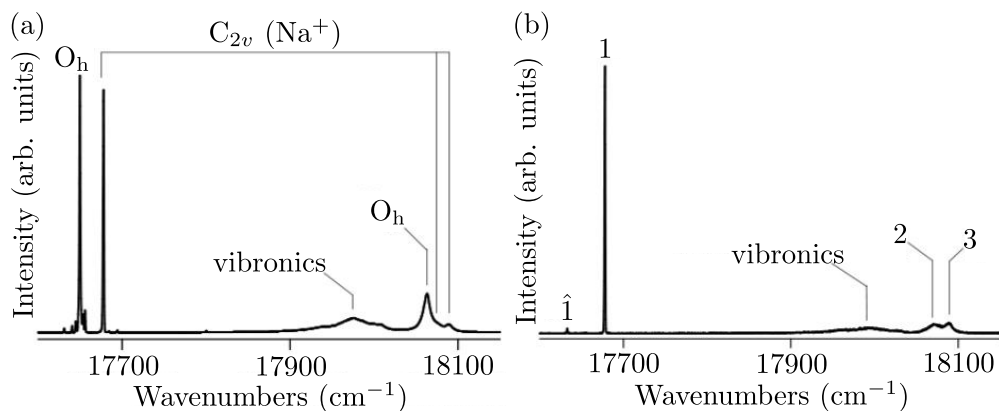

Figure 3.3: 10 K excitation spectra of the $^4G_{5/2}$ multiplet of Sm^{3+}:Na$^+$:CaF$_2$. (a) broadband excitation spectrum of both the cubic and C_{2v} centers; (b) site-selective excitation spectrum of the C_{2v} center – here $\underline{1}$ denotes the $Z_2 \rightarrow A_1$ transition.

Turning to the crystal-field calculation, we start with a crystal-field Hamiltonian

for a cubic center, which has the form [65]:

$$H_{\text{cubic}} = -\frac{1}{4}B_C^4\left[C_0^{(4)} - \sqrt{10}(C_2^{(4)} + C_{-2}^{(4)}) - \frac{3}{7}\sqrt{\frac{35}{2}}(C_4^{(4)} + C_{-4}^{(4)})\right] - \frac{13}{8}B_C^6\left[C_0^{(6)}\right.$$
$$\left. + \frac{\sqrt{105}}{26}(C_2^{(6)} + C_{-2}^{(6)}) - \frac{5}{13}\sqrt{\frac{7}{2}}(C_4^{(6)} + C_{-4}^{(6)}) + \frac{\sqrt{231}}{26}(C_6^{(6)} + C_{-6}^{(6)})\right].$$

$$(3.3)$$

To model the C_{2v} symmetry sites we add additional terms to the crystal-field Hamiltonian in order to account for a distortion from cubic symmetry:

$$H_{\text{CF}} = H_{\text{cubic}} + B_0^2C_0^2 + B_2^2(C_2^{(2)} + C_{-2}^{(2)}) + B_0^4C_0^{(4)} + B_2^4(C_2^{(4)} + C_{-2}^{(-4)}), \quad (3.4)$$

with B_q^k the crystal-field parameters. The $\hat{z}$ axis in equations (3.3) and (3.4) is chosen such that it intersects the Sm^{3+} ion, passes through the edge formed by the F^- ion cube, and then intersects the Na^+/Li^+ site. This geometry is depicted in figure 3.2.

Since the crystal-field fit critically relies on the *g*-values it is crucial that the energy level contribution to the χ^2 value is weighted with respect to the spin Hamiltonian parameter contributions. The method employed to achieve this was to initially run optimizations that preferentially fit to energy level data, and to consequently obtain initial estimates of parameter values. Subsequent optimizations were then weighted to increasingly fit to spin Hamiltonian data but to reject any parameter guesses that were substantially removed from the initial estimates. This approach is physically justifiable, since the interactions in the spin Hamiltonian are small compared to free ion and crystal-field interactions.

Using the procedure outlined above, a crystal-field fit was performed for the $C_{2v}(Na^+/Li^+)$ centers in Sm^{3+}:CaF_2 and Sm^{3+}:SrF_2. The results are split into three tables. Table 3.3 contains both the calculated energy level values as well as the experimental data obtained from site-selective excitation spectroscopy.

Table 3.3: Experimental energy levels (cm^{-1} in air, with uncertainty ± 1 cm^{-1}) and theoretical energy levels (cm^{-1}) for the C$_{2v}$(Na$^+$/Li$^+$) site of Sm^{3+} in alkaline-earth fluoride crystals. Experimental energies appended with a '?' denote uncertain assignments.

| Multiplet | State | Sm^{3+}:CaF$_2$ | | | | Sm^{3+}:SrF$_2$ | | | |
| | | Na$^+$ | | Li$^+$ | | Na$^+$ | | Li$^+$ | |
		Theory	Exp.	Theory	Exp.	Theory	Exp.	Theory	Exp.
$^6H_{5/2}$	Z_1	19	0	27	0	0	0	21	0
	Z_2	21	41	39	60	50	50	58	72
	Z_3	139	124	166	142	159	-	192	-
$^6H_{7/2}$	Y_1	941	956	960	972	980	967	999	993
	Y_2	1158	1148	1160	1162	1132	1121	1144	1140
	Y_3	1313	1319	1311	1304	1280	1269?	1288	1283
	Y_4	1335	1350	1349	1371	1311	1294?	1334	1365
$^6H_{9/2}$	X_1	2179	2185	2196	2196	2209	2198	2229	2214
	X_2	2346	2344	2343	2355	2330	2331	2338	2352
	X_3	2361	2354	2367	2369	2352	2355	2364	2367
	X_4	2522	2511	2528	2516	2488	2488	2507	2497
	X_5	2533	2550	2542	2569	2514	2548	2527	2556
$^6H_{11/2}$	W_1	3517	3517	3519	3520	3536	3571	3545	3530
	W_2	3546	3554	3570	3578	3569	3607	3593	3599
	W_3	3740	-	3727	3625	3720	3644	3723	3647
	W_4	3760	3742	3754	3751	3736	3726	3743	3738
	W_5	3777	3758	3795	3784	3767	3759	3789	3780
	W_6	3899	-	3905	-	3858	-	3874	-
$^6H_{13/2}$	V_1	4864	4857	4874	4865	4891	4864	4899	4888
	V_2	4878	4883	4896	4912	4911	4914	4936	4944
	V_3	5000	-	5010	5009	5003	5000	5024	5030
	V_4	5195	5133?	5179	5142	5163	5152	5172	5152
	V_5	5214	5183?	5201	5177	5181	5155	5188	5166
	V_6	5245	-	5254	5248	5225	-	5239	5238
	V_7	5282	-	5288	5275	5259	5241	5271	5263

Table 3.3: Experimental energy levels (cm^{-1} in air, with uncertainty ± 1 cm^{-1}) and theo-
retical energy levels (cm^{-1}) for the C_{2v}(Na$^+$/Li$^+$) site of Sm^{3+} in alkaline-earth
fluoride crystals. Experimental energies appended with a '?' denote uncertain
assignments.

| Multiplet | State | Sm^{3+}:CaF$_2$ | | | | Sm^{3+}:SrF$_2$ | | | |
| | | Na$^+$ | | Li$^+$ | | Na$^+$ | | Li$^+$ | |
		Theory	Exp.	Theory	Exp.	Theory	Exp.	Theory	Exp.
$^6F_{1/2}$,	S_1	6170	6161	6179	6165	6196	6188	6212	6191
$^6F_{3/2}$,	S_2	6187	6192	6210	6216	6217	6220	6246	6243
$^6H_{15/2}$	S_3	6284	-	6299	6312	6297	-	6319	6347
	S_4	6570	6564	6580	6571	6539	6529	6554	6543
	S_5	6721	6717	6692	6723	6666	6682	6656	6692
	S_6	6728	6724	6731	6731	6699	6696	6721	6709
	S_7	6754	6747	6756	6758	6728	6724	6744	6744
	S_8	6765	6766	6770	6782	6745	6741	6753	6764
	S_9	6850	6891	6837	6867	6811	6835	6814	6858
	S_{10}	6910	6911	6907	6894	6849	6860	6863	6871
	S_{11}	6940	6929	6940	6940	6893	6882	6900	6906
$^6F_{5/2}$	R_1	7252	7273	7268	7282	7230	7246	7249	7262
	R_2	7379	7368	7386	7373	7336	7330	7351	7341
	R_3	7388	7381	7397	7395	7360	7344	7371	7366
$^6F_{7/2}$	Q_1	8128	8130	8140	8136	8102	8108	8121	8120
	Q_2	8135	8142	8149	8156	8109	8118	8127	8139
	Q_3	8140	8162	8153	8173	8129	8135	8147	8154
	Q_4	8279	-	8287	-	8245	-	8259	-
$^6F_{9/2}$	P_1	9286	9277	9291	9287	9265	9260	9284	9277
	P_2	9306	9307	9313	9313	9279	9283	9292	9296
	P_3	9312	9321	9331	9334	9291	9298	9318	9318
	P_4	9383	9370	9392	9379	9349	9345	9368	9363
	P_5	9387	9375	9400	9386	9359	9351	9379	9371
$^4G_{5/2}$	A_1	17693	17678	17713	17690	17728	17722	17742	17735
	A_2	18061	18072	18051	18074	18069	18087	18069	18070
	A_3	18086	18089	18109	18109	18112	18100	18133	18138

Table 3.4 summarizes the calculated and measured *g*-values and hyperfine parameters. It should be noted that due to the upper limit of the EPR magnetic field strength of 1.5 Tesla, the uncertainty of the hyperfine parameters was up to 80%. Additionally, it was difficult to obtain a consistent fit to both the *g*-values as well as the hyperfine parameters if an equal weighting was selected for both. Thus, the fitting routine was heavily weighted to preferentially minimize the χ^2 contribution due to the Zeeman effect. Finally, table 3.5 contains the free-ion and crystal-field

Table 3.4: Fitted and experimental spin Hamiltonian parameters of the $C_{2v}(Na^+/Li^+)$ site of Sm^{3+} in alkaline-earth fluoride crystals. *A*-values are in cm^{-1}. It should be noted that due to the upper limit of the EPR magnetic field strength of 1.5 Tesla, the uncertainty of the hyperfine parameters was up to 80%.

Parameter	$Sm^{3+}:CaF_2$				$Sm^{3+}:SrF_2$			
	Na$^+$		Li$^+$		Na$^+$		Li$^+$	
	Theory	Exp.	Theory	Exp.	Theory	Exp.	Theory	Exp.
g_x	0.603	0.606	0.579	0.583	0.611	0.606	0.633	0.637
g_y	0.473	0.477	0.556	0.558	0.539	0.537	0.565	0.577
g_z	0.300	0.300	0.299	0.300	0.338	0.340	0.329	0.330
A_x	0.018	0.021	0.013	0.022	0.012	-	0.005	0.024
A_y	0.017	0.020	0.023	0.020	0.019	-	0.018	0.020
A_z	0.007	0.007	0.014	0.010	0.012	-	0.007	-

parameters that were obtained by fitting to the energy levels from site-selective excitation spectroscopy, as well as the *g*-values and hyperfine parameters determined from EPR spectroscopy.

As can be seen, a good agreement is found between both the energy level data and the *g*-value data. The hyperfine parameters deviate considerably from their experimentally observed values, but as noted above, the experimental uncertainty associated with the hyperfine parameters is in excess of $\sim 80\%$. Therefore, the calculated values fall within the experimental uncertainty. A point of interest from table 3.5 is the magnitude of distortion from cubic symmetry in the various materials. The most dominant trend is the substantial distortion represented by the values of the B_2^2 and B_2^4 parameters for the Li$^+$ co-doped samples as compared

Table 3.5: Fitted values for free-ion and crystal-field parameters of the C_{2v}(Na^+/Li^+) site of Sm^{3+} in alkaline-earth fluoride crystals. For the case of Sm^{3+}:Na^+:SrF_2, no hyperfine data points were available; consequently the hyperfine coupling constant was assumed to be 0.005 cm^{-1} to estimate the corresponding theoretical A-values.

Parameter	Sm^{3+}:CaF_2 (cm^{-1})		Sm^{3+} :SrF_2 (cm^{-1})	
	Na^+	Li^+	Na^+	Li^+
E_{AVG}	47739	47773	47640	47736
F^2	79840	79877	79031	79543
F^4	56203	56576	58061	57342
F^6	40600	40350	39643	39978
ζ	1175	1173	1173	1173
B_0^2	-144	-227	-167	-205
B_2^2	56	130	62	114
B_0^4	176	-155	-543	-767
B_2^4	-248	-149	835	578
B_C^4	-1796	-1832	-2717	-2441
B_C^6	906	865	750	731
a_l	0.005	0.0047	0.005	0.0041

to their Na^+ counterparts. This can be explained by the small ionic radius of Li^+ compared to the ionic radius of Na^+, which roughly matches the ionic radius of Ca^{2+}. Additionally, by computing the covariance matrix, it was established that the values of B_0^4 and B_2^4 could be set to zero without substantially affecting the quality of the fit for Sm^{3+}:Na^+:CaF_2. The same does not hold true for the remaining materials, which substantiates the following trend: there is an increase in distortion from cubic symmetry for crystals co-doped with Li^+ compared to crystals co-doped with Na^+. Furthermore, CaF_2 hosts show less distortion from cubic symmetry than SrF_2 hosts. The magnitude of the standard deviation also explains the opposite sign of B_2^4 for Sm^{3+}:Na^+:CaF_2 compared to the other materials.

An additional noteworthy point is the magnitude by which the fitted parameters are altered by the inclusion of the Zeeman interaction data. To quantify this, we performed a fit for Sm^{3+}:Na^+:CaF_2 using the Hamiltonian (3.4), with the contribution of the Zeeman term to the χ^2-value set to zero. This yielded the following parameters: $B_C^4 = -2423$ cm^{-1}, $B_C^6 = 897$ cm^{-1}, $B_0^2 = -41$ cm^{-1}, $B_2^2 = -92$ cm^{-1}, $B_0^4 = -576$ cm^{-1}, and $B_2^4 = 303$ cm^{-1}. Furthermore, the obtained g-values

were: $g_x = 0.60$, $g_y = 0.44$, and $g_z = 0.68$. These values show that the inclusion of the Zeeman interaction data shifts the values of fitted parameters beyond their estimated uncertainty. Additionally, one of the theoretically predicted g-values differs from the corresponding observed value by over 80%.

Finally, it is interesting to observe that calculated distortion is evident in the electron-paramagnetic resonance measurements as a tilting of the g-tensor $\hat{x}$ principal axes with respect to the corresponding crystal-field axis [114].

Thus, to conclude this section, the performed test case of the developed spin-Hamiltonian enhanced crystal-field fitting using C_{2v} (Na$^+$/Li$^+$) centers in Sm^{3+}:CaF$_2$ and Sm^{3+}:SrF$_2$ has yielded good agreement between experimental and theoretical energy level and spin Hamiltonian data.

4

High-resolution spectroscopy and crystal-field analysis of C_1 symmetry sites of Er^{3+}:Y_2SiO_5

This chapter deals with a general spectroscopic study of Er^{3+}:Y_2SiO_5, with the aim of developing an accurate crystal-field model for this material. While much of the experimental development was performed with this aim in mind, the established techniques also have a broader relevance in the context of experimental QIP. More specifically, the primary experiments that were developed at Canterbury as part of this thesis were magnetic-field dependent laser transmission and spectral hole burning (SHB). The former is particularly relevant for ZEFOZ transitions as this requires an extremely precise understanding of the magnetic response of the optically active ion. SHB has a wide range of applications in QIP, the specifics of which are somewhat dependent on the material. It allows for investigations of homogeneous linewidths, hyperfine splittings as well as different mechanisms of spectral diffusion when combined with an external field.

In the context of this chapter, Zeeman laser transmission experiments were employed to measure the $^4F_{9/2}D_1$ excited-state g-value for the magnetic field coincident with the crystallographic b axis. This is of direct aid to the crystal-field calculation, since it provides additional information about the exact crystalline orientation, which critically relies on detailed magnetic information in order to fit the total of 27 independent crystal-field parameters required for a C_1 symmetry Hamiltonian. Turning to the SHB experiment, while it was not possible to employ this technique to obtain additional hyperfine levels, hyperfine level storage was observed for the $^4F_{9/2}D_1$ level at zero field.

Trivalent erbium has an electron configuration of $4f^{11}$, and consequently has a total of 364 electronic states in 41 free-ion multiplets. While there are several stable isotopes of erbium, ^{167}Er is the only stable isotope with non-zero nuclear spin, which hase a value of $I = 7/2$ [115]. Therefore, ^{167}Er has a total of 2912 hyperfine states. The optical properties of Er^{3+}:Y_2SiO_5 have been studied in detail in the past. Li *et al*. [116] reported optical absorption and fluorescence spectroscopy measurements both at room temperature and at 10 K. This was followed by detailed energy level assignments from the ground state to the $^2H_{11/2}$ multiplet by Doualan *et al*. [117].

The first measurement of optical coherent transient phenomena were performed by Macfarlane *et al*. [118], which consisted of two-pulse photon echo experiments that yield dephasing times as long as 580 μs, corresponding to a homogeneous linewidth of 550 Hz. This dephasing time was further increased by Sun *et al*. [14] to 6.4 ms by employing low dopant concentration samples with 10 ppm Er^{3+}. This is equivalent to a homogeneous linewidth of $\sim$ 50 Hz, which to our knowledge is the narrowest optical transition reported to date. Later studies consisted of detailed analyses of spectral diffusion mechanisms in Er^{3+}:Y_2SiO_5 [38, 40, 42, 119]. The ground-state g-tensor as well as hyperfine tensors were then measured using electron paramagnetic resonance by Guillot-Noël *et al*. [37]. Additionally, optical measurement of the magnetic g-factors for both the ground-state level $^4I_{15/2}Z_1$ as well as the first excited-state level $^4I_{13/2}Y_1$ were initially performed by Böttger *et al*. [38] and completely characterized by Sun *et al*. [39]. Hastings-Simon *et al*. [120] determined the lifetimes of Zeeman levels using hole-burning spectroscopy, while Lauritzen *et al*. [41] investigated spectral tailoring of the Er^{3+}:Y_2SiO_5 absorption profile by employing stimulated emission using a second laser and spin mixing.

The first sections of this chapter will deal with generic material characterization followed by a detailed description of the experiments that were developed. This is followed by results and discussion of Zeeman laser transmission and SHB spectroscopy experiments. Finally, we will describe the crystal-field fit which employs the experimental data measured in this study, as well as the g-tensors reported by Sun *et al*. [39] and the ground-state hyperfine tensors due to Guillot-Noël *et al*. [37].

4.1 Crystal structure and symmetry of Er^{3+}:Y$_2$SiO$_5$

In order to uniquely define the orientation of the crystal in both the experiments and the calculations performed in this chapter, we will begin by outlining the crystallographic structure of Er^{3+}:Y$_2$SiO$_5$. The crystal structure of Y$_2$SiO$_5$ has been determined to be monoclinic with space group C_{2h}^6 [121]. The lattice constants, converted from the I_{2a} space group, which is isomorphic to C_{2h}^6, are $a = 1.041$ nm, $b = 0.6721$ nm, $c = 1.249$ nm, and $\beta = 102°39'$. We note that there is some ambiguity in the literature regarding the choice of the lattice constants a and b, with a disagreement most notably between reference [122] and reference [121]. We here follow the convention of Maksimov *et al.* , but converted to the C_{2h}^6 space group. The C_2 space-group symmetry axis corresponds to the crystallographic b axis, while the crystallographic a and c axes are located in the mirror plane that is perpendicular to b. Additionally, following Li *et al.* [116], we label the optical extinction axes D_1 and D_2 which are perpendicular and in the same plane as a and c. The orientation of the sample with respect to this set of axes is shown in figure 4.1. Throughout this chapter we will refer to the b, D_1, and D_2 axes to specify the sample orientation.

Each unit cell is composed of eight Y$_2$SiO$_5$ molecules, and there are two substitutional sites occupied by yttrium atoms. These sites are labeled Y_1 and Y_2, with both having a triclinic point-group symmetry of C_1. The sites Y_1 and Y_2 are distinguished by their coordinate numbers of six and seven respectively, which indicates the number of bonds each site has to surrounding oxygen atoms.

For a RE^{3+} ion substituting at one of these sites there are additional subclasses of ions due to the C_{2h} space-group symmetry of the unit cell. For the purpose of the experiments detailed in subsequent chapters, the sites that are related by inversion symmetry are equivalent. However, sites related by the rotational symmetry of π multiplicity have distinguishable interactions with an external magnetic field, and will consequently be of relevance in the context of Zeeman rotation patterns. Thus, in total each crystallographic site is composed of two magnetically inequivalent sites [39].

All measurements were performed on two single crystal samples grown using the Czochralski process by A. Ferrier, Chimie ParisTech, France, at erbium concentration levels of 50 ppm and 10 ppm.
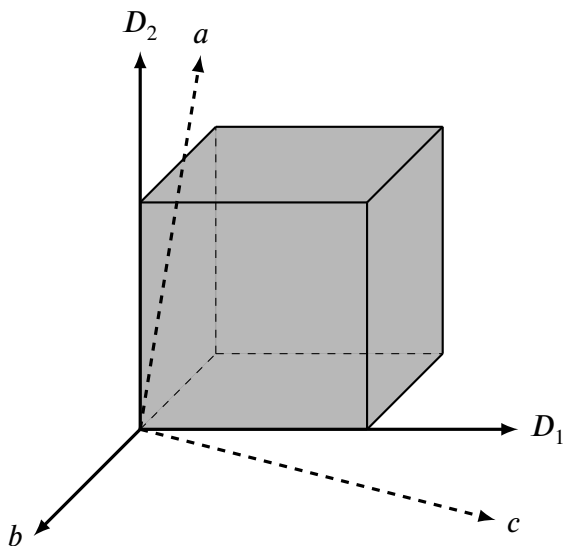
Figure 4.1: The crystallographic axes of the space group C_{2h}^6 for monoclinic Y_2SiO_5. The D_1 axis is 23.8° from the c axis and 78.7° from the a axis. D_1 is perpendicular to D_2, which are both perpendicular to the crystalline C_2 axis labeled as b.

4.2 Experimental details

Broad-band absorption measurements were performed with an Agilent Cary 6000i spectrophotometer. The sample was cooled to 10 K using a Janis CCS-150 closed-cycle cryostat and a Lakeshore 325 temperature controller which adjusted the current through a resistive heater attached to the back of the sample cold finger. The absorption spectra were measured for a 50 ppm $Er^{3+}:Y_2SiO_5$ sample with the absorption along the crystallographic b axis and isotropic polarization in the D_1-D_2 plane. The crystal had dimensions of 6.68 mm along the D_2 axis, 4.52 mm along the D_1 axis, and 4.95 mm along the crystallographic b axis.

Laser absorption spectroscopy was conducted using a Toptica DL100 pro grating stabilized diode laser with a nominal line with of $\sim$ 1 MHz. A Glan-Thompson polarizer was used to select the laser polarization. The crystal was again mounted for absorption along the crystallographic b axis in a Janis CCS-150 closed-cycle cryostat with a Lakeshore 325 temperature controller used to regulate the temperature to 10 K. The absorption was detected by recording the laser intensity transmitted through the sample with a Newfocus 1801-FS 125 MHz photoreceiver while

the laser was swept in wavelength. Additionally, part of the beam was picked-off prior to the cryostat and recorded as a laser reference with a Thorlabs PDA36A.

The DL100 pro allows for a nominal coarse tuning range between 646 nm and 657 nm by adjusting the external grating angle. In order to excite the longest wavelength transitions for both sites in Er^{3+}:Y_2SiO_5, the wavelength range was extended to 661 nm by optimizing the intra-cavity collimation optics for long wavelengths. The coarse tuned wavelength was monitored using a Bristol 521 fiber-coupled wavemeter. Mode-hop free fine tuning of the DL100 was performed by a piezo stack mounted behind the external grating. This enabled a fine-tuning range of up to 20 GHz. Thus, by modulating the piezo input wavelength with a saw-tooth waveform the DL100 could be periodically swept across the absorption profile of the $^4I_{15/2} \rightarrow {}^4F_{9/2}$ transition. The precise wavelength across each scan was calibrated by passing part of the laser through a Coherent 33-6305-001 Fabry-Pérot interferometer with a free spectral range of 300 MHz. Consequently, for every 300 MHz of laser sweep, a constructively interfered lineshape is transmitted through the Fabry-Pérot, which enabled the width of individual scans to be precisely calibrated.

Both the magnetic-field dependent laser transmission experiments and the SHB measurements were performed using the same physical setup. The experimental setup is schematically shown in figure 4.2. The Toptica DL100 pro grating stabilized laser was used for the generation of both the pump pulse as well as the probe pulse. The pulse sequence for SHB is prepared using an AOM (IntraAction 802AF1) in the double-pass configuration, which is driven by a PulseBlaster-DDSII arbitrary waveform generator (AWG) in conjunction with a Mini-Circuits ZHL-2W+ RF amplifier. The PulseBlaster additionally served as the central timing unit of the experiment, taking responsibility for the generation of laser pulse sequences, both in time and frequency, as well as triggering the data acquisition equipment.

Similar to the laser absorption measurement described above, the DL100 was swept in wavelength by modulating the piezo voltage. However, rather than employing a saw-tooth waveform, a custom ramp function was developed to minimize mode-hopping for fast scan repetition rates. This waveform was produced using a Hewlett-Packard HP33120A AWG triggered via a TTL by the PulseBlasterDDSII. The functional form of this custom ramp is shown in figure 4.3. As de-
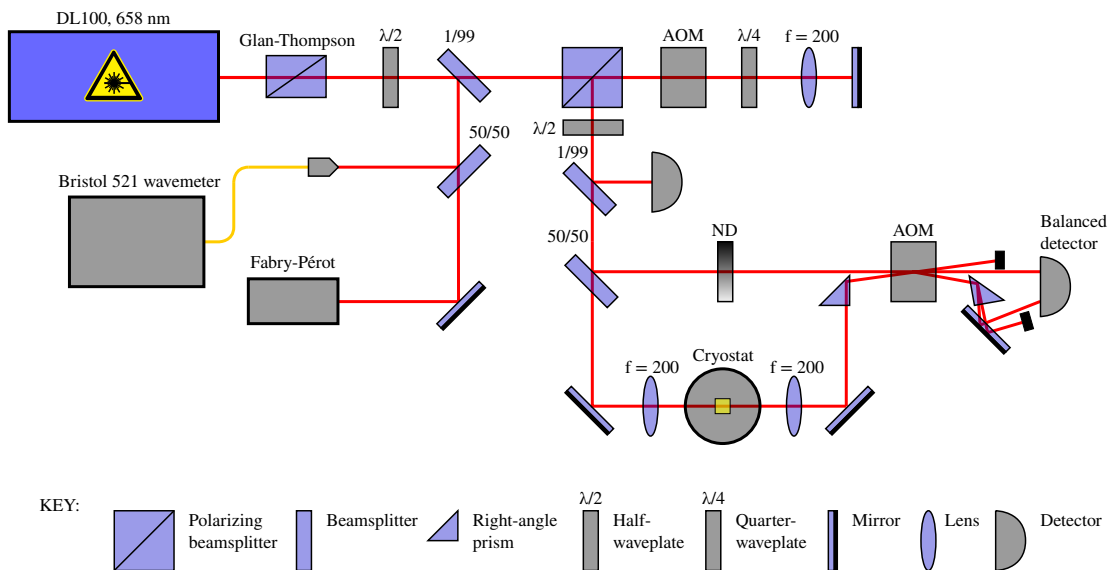
Figure 4.2: Beam path and key components of the SHB experiment. See the text
for a detailed description of key components.

scribed above for the laser absorption spectroscopy, the laser scan frequency range
was calibrated by monitoring the transmission through a Coherent 33-6305-001
Fabry-Pérot cavity.

In order to detect absorption through the sample, while simultaneously reject-
ing any laser power fluctuations, a balanced detection scheme was used. This was
achieved by splitting the beam prior to the sample into a probe and reference path
of equal intensities. Any attenuation of the probe pulse was then recorded us-
ing a Newport 1807-FS balanced detector. To achieve optical balance for an off-
resonance laser, and thus to account for any power differences due to the cryostat
windows, a variable neutral density filter was inserted into the reference beam.

The balanced detector is additionally gated by an AOM (IntraAction 802AF1)
driven by a Mini-Circuits ZX95-100S+ voltage-controlled oscillator in tandem
with a Mini-Circuits ZHL-2W+ RF amplifier. Accurate timing was achieved by
gating the RF signal prior to amplification using a Mini-Circuits ZYSW-2-50DR
TTL activated switch, controlled using the PulseBlasterDDSII. This additional
AOM was required, since when the balanced detector was operated near the max-
imum power threshold a large optical imbalance resulted in a DC offset that per-
sisted for hundreds of milliseconds. Additionally, since the optical imbalance de-
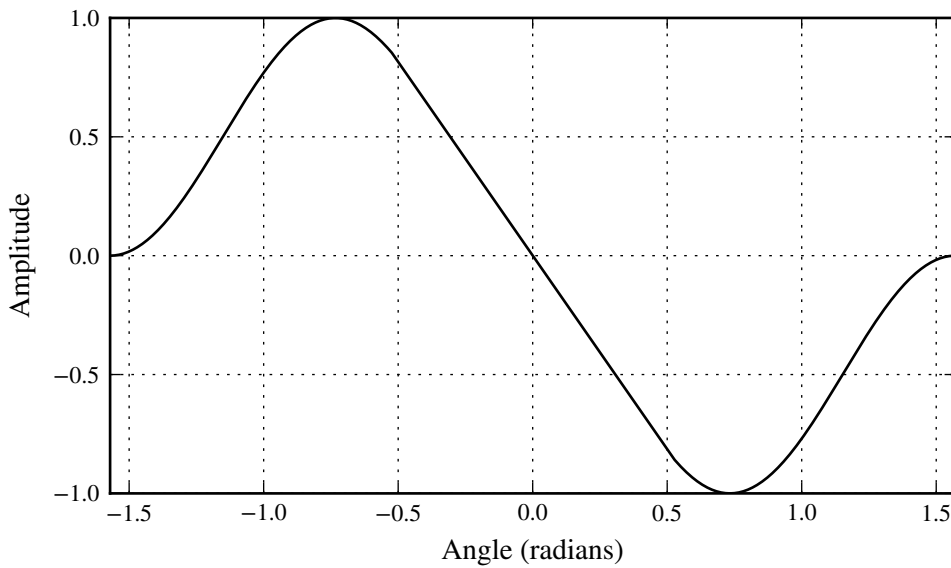
Figure 4.3: Smooth ramp applied to DL100 piezo using a HP33120A AWG in order to scan the laser frequency with minimum likelihood of unwanted mode hops. The figure shows one complete period, the length of which could be adjusted by altering the HP33120A frequency. Additionally, the DL100 scan amplitude, which is dependent on the peak-to-peak voltage of the waveform applied to the piezo, could be adjusted by controlling the amplitude of the depicted ramp.

pended on whether the burn pulse was tuned precisely on resonance, the DC offset moved if the burn laser drifted or was tuned. Thus, by gating the detector with an AOM that is switched to zero-order for the burn pulse, this offset was mitigated. Unfortunately due time constraints and the local availability of AOMs as well as suitable RF supplies, both the reference and transmission beams had to be gated with a single AOM. While this trivially ensured coincident gating of both beams, the single pass efficiency for each beam was no better than 40% due to the difficulty of aligning two independent beams through one AOM.

All detector signals were digitized with a Tektronix DPO7104 oscilloscope. A central program was developed that allowed for a variety of burn-probe pulse sequences, including kHz frequency-modulation (FM) spectroscopy performed using the double-pass AOM, as well as 20 MHz FM spectroscopy implemented using an EOM. Initially, the necessary PulseBlaster sequence is generated and loaded

onto the device; thereafter, all timing control is handed off to the PulseBlaster core which triggers all peripheral equipment including the data acquisition. During a scan sequence, waveform data is asynchronously transferred from the DPO7104 using the VXI-11 protocol over Ethernet, and stored using the HDF5 data format [123].

Figure 4.4 shows the pulse sequence that was employed and notes the various parameters that can be altered. This pulse sequence was repeated at a pre-defined repetition rate with a user-defined number of shots averaged per scan.
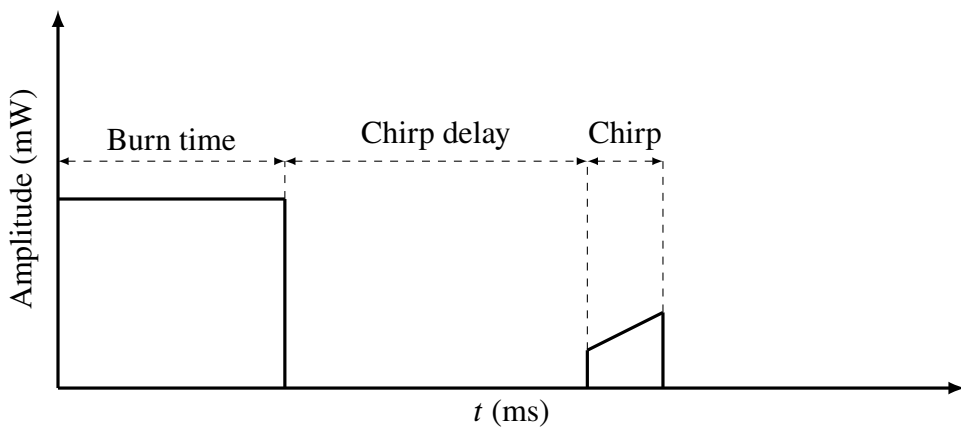

Figure 4.4: Parameters of the pulse sequence used for the spectral hole-burning experiments. The pulse amplitude, pulse-time, chirp-delay and chirp amplitude were readily adjustable using the developed software. The chirp time was typically fixed to 1 ms. Additionally, the range of the chirp frequency sweep was adjustable by altering the peak-to-peak voltage of the ramp function applied to the piezo of the DL100 pro laser.

The scan procedure was programmed to step through a either range of chirp-delay times, pulse-amplitude values, or burn-pulse lengths. While stepping through the chosen sequence, each scan was preceded with an identical reference scan that excluded the burn pulse. This was performed since the laser frequency drifted over the course of tens of minutes. Thus, since a typical reference-burn scan took substantially less time than this, it was possible record an accurate reference of the absorption profile without a burn pulse which could later be subtracted to account for any laser drift.

In order to achieve a more sensitive method of detecting changes in absorption

of the probe pulse in SHB, and thus potentially enable the detection of hyperfine level storage, a frequency-modulation (FM) absorption spectroscopy setup was implemented to complement the above direct transmission measurements. In this technique, the probe pulse is frequency modulated which, for a correctly chosen modulation depth, results in a central carrier with upper and lower side bands. The carrier is at the frequency of the unmodulated probe pulse, whereas the side-bands are displaced at plus and minus the modulation frequency. If the probe pulse passes through a sample and either the upper or the lower side-band over-laps in frequency with a spectral feature, then a beat can be observed when the beam impinges on the detector [124, 125]. As was first observed in the references [124, 125], provided the modulation frequency is large compared to the spectral feature, the in-phase component of the beat signal is directly proportional to the absorption of the side-band, whereas the quadrature component is directly pro-portional to the dispersion induced by the spectral component. Additionally, as noted by Bjorklund, if the modulation frequency is much smaller than the width of the spectral feature one is operating in the regime of wavelength modulation spectroscopy. Thus, the absorption is instead proportional to the derivative of the in-phase component, whereas the dispersion is proportional to the second deriva-tive of the quadrature component of the beat signal [124, 126].

The experimental implementation primarily focused on the FM modulation sce-nario where the modulation frequency is greater than the width of the spectral fea-ture. However, some attempts were made at employing the double-pass AOM to apply a kHz frequency modulation to the chirp pulse. While the frequency mod-ulation was visible using the Fabry-Pérot, the detection of a beat signal was not successful.

The changes to the experimental layout required for FM spectroscopy are shown in the schematic presented in figure 4.5. Here the key additions are an RF mixer and a 20 MHz electro-optic phase modulator (EOM, Thorlabs EO-PM-R-20-C1). The EOM was driven using the second AWG channel of the PulseBlasterDDSII, which allowed for a precise temporal control over which components of the pulse sequence should be modulated. Additionally, since the SHB experiment was pulsed, it was not possible to employ standard methods used in FM spectroscopy to elim-inate residual amplitude modulation due to the EOM [127]. However, the use of a balanced detection scheme seemed to largely mitigate the issue of residual

amplitude modulation noise.
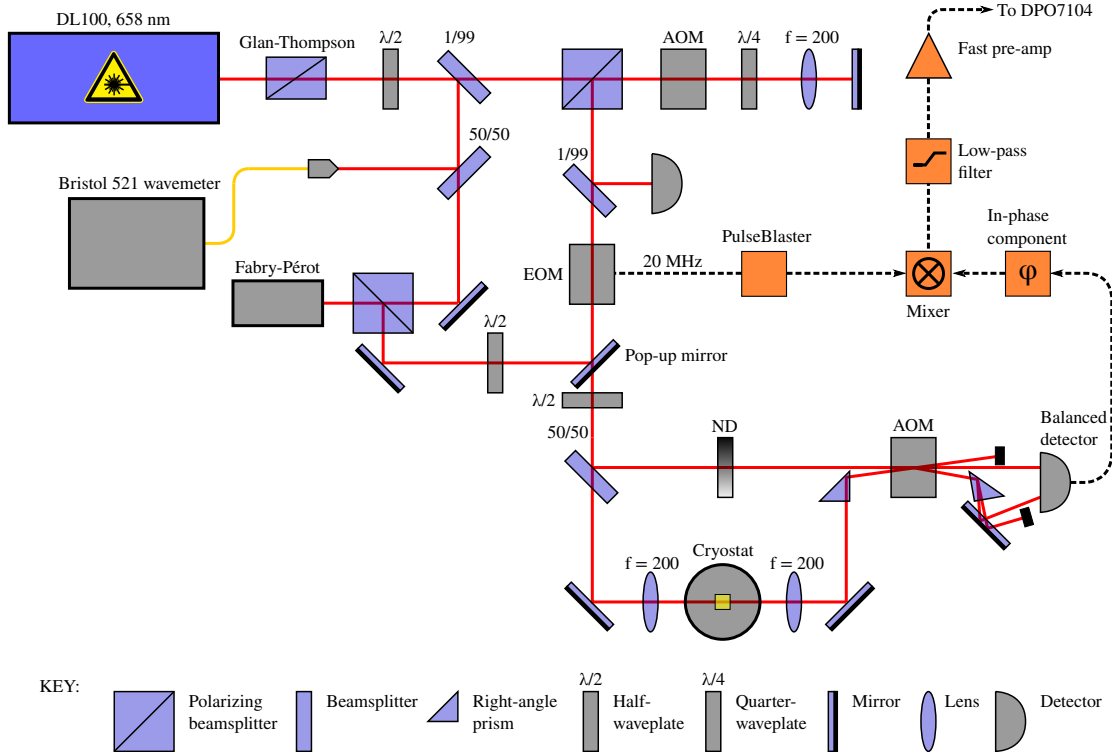
Figure 4.5: Beam path and key components of the SHB experiment with frequency modulation spectroscopy used for enhance detection sensitivity. See text for a detailed description of key components.

The in-phase component of the RF beat signal was obtained using an RF splitter (Mini-Circuits ZMSCQ-2-50+), which was further reduced to a DC signal using homodyne detection with a Mini-Circuits ZFM-3-S+ mixer. Before digitization with the Tektronix DPO7104 oscilloscope, the signal was low-pass filtered using a Mini-Circuits SLP-2.5+ and amplified using a Stanford Research Systems SR240A fast pre-amp.

One of the critical parameters of the FM setup was the modulation depth employed. The initial characterization was completed by analyzing the FM modulated beam using the Fabry-Pérot interferometer. Figure 4.6 shows the Fabry-Pérot spectra obtained at four different modulation depths.

In order to further determine the optimal modulation depth, a number of trial scans were conducted. Figure 4.7 shows the FM SHB spectra obtained for spectroscopic site Y_2 at an external field of 0.067 Tesla, applied along the crystallographic
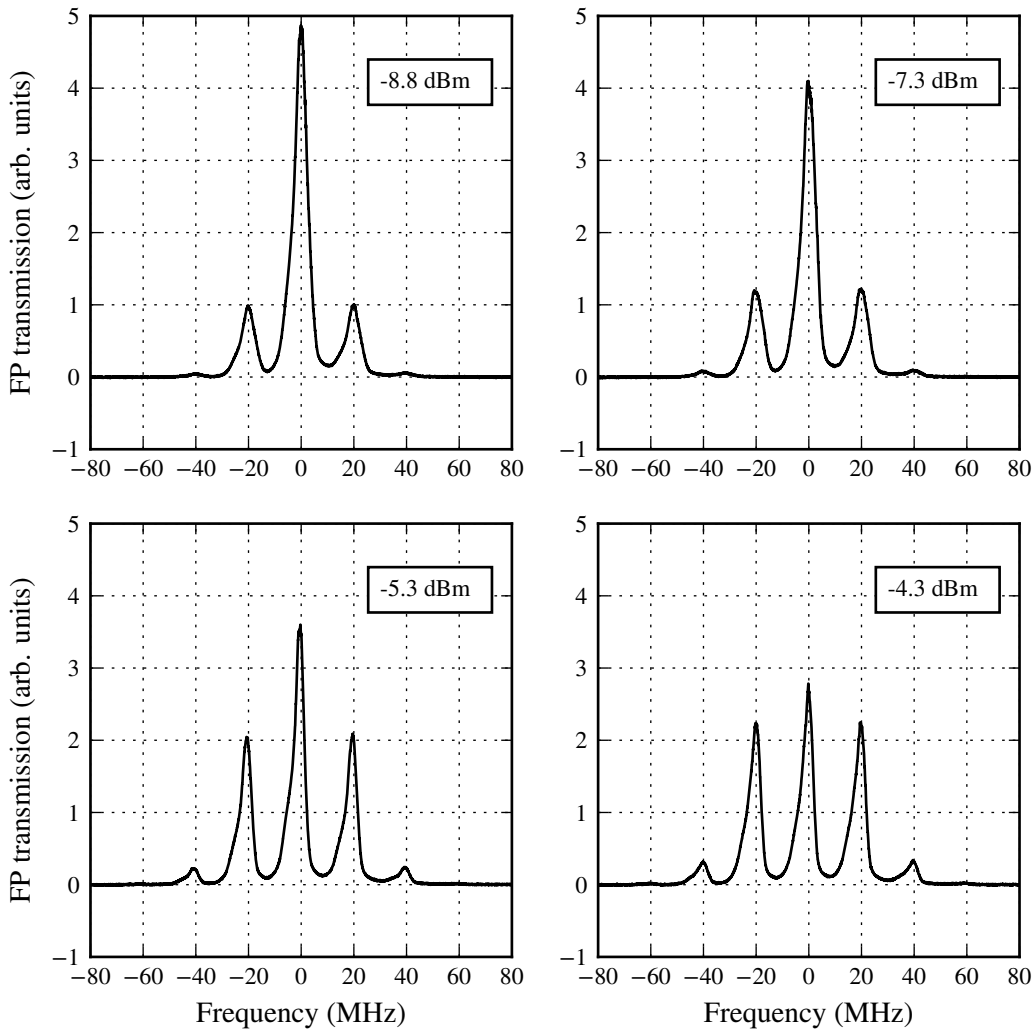
Figure 4.6: Fabry-Pérot spectrum of FM modulated laser at various modulation depths. The power specified in each inset corresponds to the RF power applied to the 20 MHz EOM. Evidently an RF drive power as low as -8.8 dBm was sufficient to obtain well defined upper and lower sidebands.

b axis for a variety of modulation powers applied to the EOM. From this it was concluded that an RF drive power of -7.3 dBm produced the clearest FM signal.

Throughout the development of the above described Zeeman laser transmission and hole-burning experiments, several cryostats were employed to cool samples. Initially, a home-built glass immersion cryostat was used. This consisted of a 10
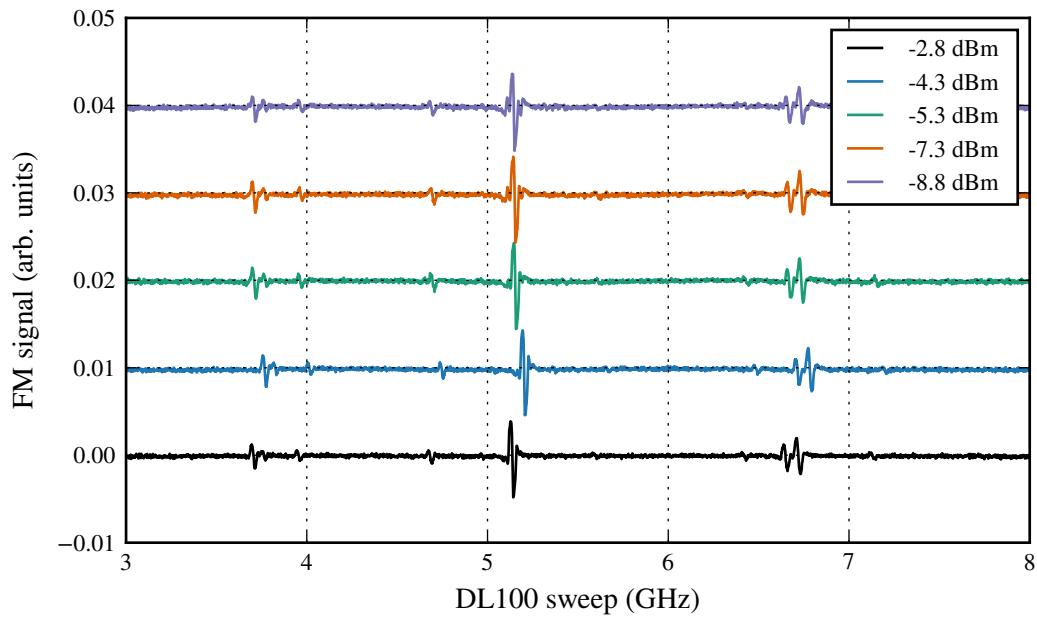
Figure 4.7: FM absorption SHB spectrum at various EOM modulation powers of spectroscopic site Y_2 of Er^{3+}:Y_2SiO_5. The sample is at 2 K, with a magnetic field of 0.067 Tesla applied along the crystallographic *b* axis. It is apparent that for higher modulation powers the dispersive lineshapes become nosier. This can be attributed to higher order sidebands becoming significant leading to more complex beat patterns.

liter helium bath with an outer liquid nitrogen jacket. By controlling the vapor pressure of the helium bath, a temperature range between 1.6 K to 2.2 K was achieved. The pressure was regulated using a manostat in tandem with an Anest Iwata ISP 250 vacuum pump. Above the liquid helium Lambda point, persistent bubbles in the helium made the operation of this cryostat impractical.

In order to conduct magnetic-field dependent studies, the immersion cryostat was replaced with a 4 Tesla home-built Nb-Ti superconducting magnet. The sample was mounted on a cold-finger in contact with the superconducting coil helium bath. Since the helium reservoir was not designed to be pumped, the operational temperature was fixed to 4.2 K. From previous spectroscopic studies, it was known that the temperature of the cold-finger is only marginally warmer than the bath temperature.

After the bulk of the magnetic-field dependent studies were completed, access

was gained to an Oxford Instruments SpectroMag cryostat with a superconducting split coil providing magnetic field strengths up to 7 Tesla. The optical tail of this system featured a sample cell separate from the superconducting winding reservoir, with the facility to be pumped; thus, temperatures as low as 1.3 K could be obtained. Below the liquid helium Lambda point, a constant temperature was again achieved by using a manostat to control the vapor pressure. For temperatures between 2.2 K and 4.2 K, the sample space was evacuated to 5 Torr, and the needle valve controlling helium flow from the reservoir to the sample cell was opened manually to achieve the required temperature, which was inferred from the resistance of a calibrated Allen-Bradley resistor. In future, this system could be substantially improved by controlling the temperature of the helium vapor entering the sample cell using a small heater mounted on the needle valve. By mounting a silicon diode temperature sensor, this heater could be driven in a closed loop, thus ensuring that all helium gas entering the sample cell is of a constant temperature. Consequently, temperature gradients typically encountered when a heater is mounted on the sample cold finger could be mitigated. For temperatures above 4.2 K, the needle valve controlling helium flow from the reservoir to the sample cell was fully opened and the helium boil-off was used for cooling. The boil-off flow was regulated using positive pressure in the sample cell, which was controlled by a solenoid valve driven by a closed loop controller with feedback from an Allen-Bradley resistor. This regulated the amount of helium vapor that entered the sample space and thus allowed for temperature control up to 20 K without the application of a heater.

4.3 Absorption spectroscopy

Figure 4.8 shows the absorption spectrum for the $^4F_{9/2} \rightarrow {}^4I_{15/2}$ transitions of the 50 ppm Er^{3+}:Y_2SiO_5 sample at 10 K recorded with the Agilent spectrophotometer. The indicated transition wavelengths were obtained by fitting Gaussian lineshapes to each peak. Numbers in parentheses of each label of figure 4.8 designate the spectroscopic site using the assignments by Doualan *et al*. [117].

The precise transition energies determined from this measurement was further followed up by laser transmission spectroscopy in order to determine the inhomogeneous linewidth as well as the polarization dependent absorption.
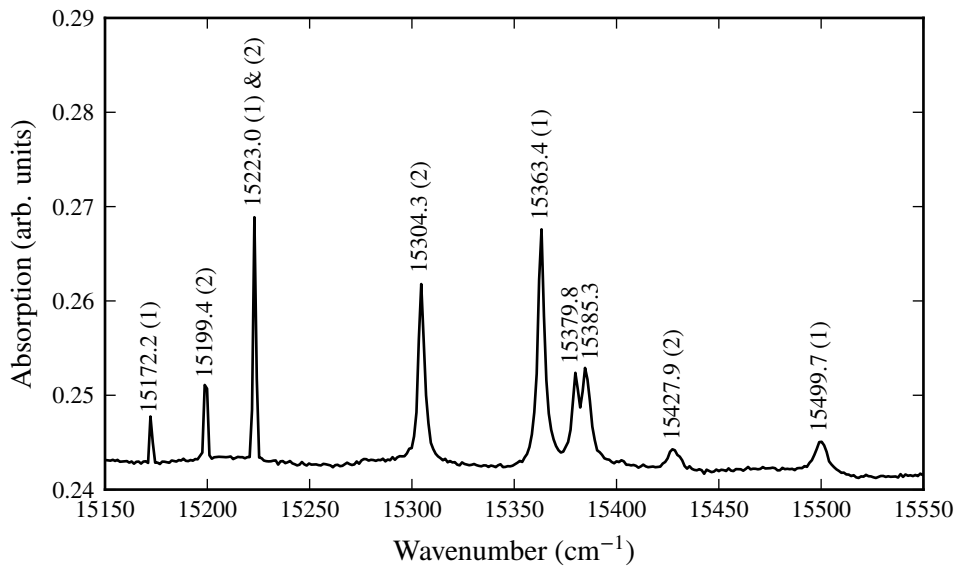
Figure 4.8: Absorption spectrum for the $^4F_{9/2} \rightarrow {}^4I_{15/2}$ transition along the crystallographic b axis for a 50 ppm Er^{3+}:Y_2SiO_5 crystal at 10 K. Lineshape centers are shown for each transition, with parentheses indicating the crystallographic sites for transitions where the assignment is unambiguous from site-selective fluorescence experiments [117].

In order to conduct the absorption measurement the laser was coarse-tuned to the central absorption wavelength determined by fitting Lorentzian lineshapes to the absorption spectra recorded with the Cary 6000i. Using the Bristol 521 wavemeter, the laser was determined to be at 15172.66 ± 0.15 cm^{-1} (in air) when tuned to the center of the inhomogeneous absorption profile of site 1, whereas it was 15199.25 ± 0.15 cm^{-1} (in air) for site 2.

Figure 4.9 shows both the horizontally and vertically polarized laser transmission for the $^4I_{15/2}Z_1 \rightarrow {}^4F_{9/2}D_1$ transition of crystallographic site 1 of the 50 ppm Er^{3+}:Y_2SiO_5 sample at 10 K. It is readily apparent that the strongest absorption for site 1 is for $E \parallel D_2$. In order to establish the total absorption as well as the inhomogeneous linewidth, a Lorentzian lineshape was fitted to the absorption profile. The full width at half maximum (FWHM) for $E \parallel D_2$ was determined to be 475.94 MHz, while for $E \perp D_2$ it was 463.66 MHz.

Analogous measurements were performed for the second crystallographic site of the 50 ppm Er^{3+}:Y_2SiO_5 sample. The transmission spectra for both the vertical
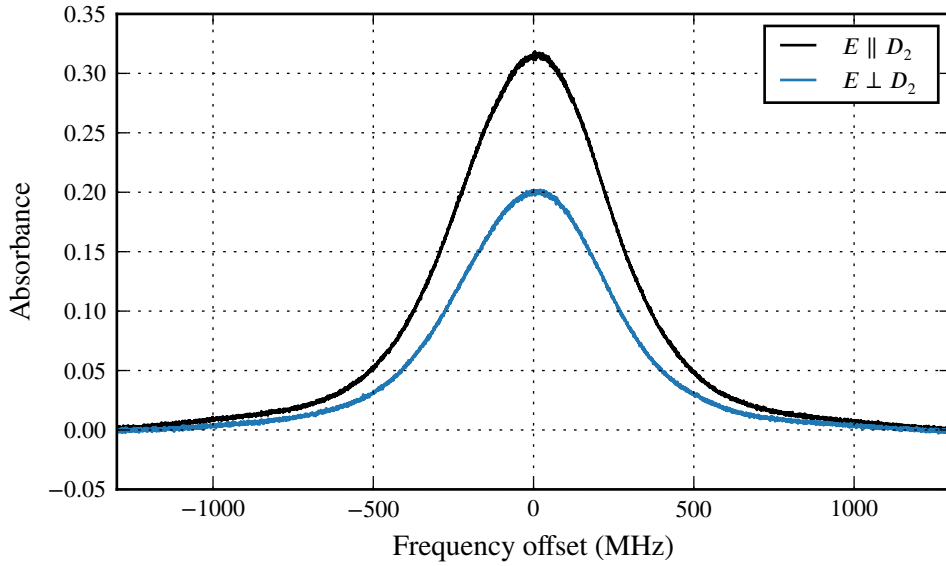
Figure 4.9: Site 1 laser absorption measurement for both vertical and horizontal polarization of the $^4F_{9/2} \rightarrow {}^4I_{15/2}$ transition for the crystallographic site 1 of 50 ppm Er^{3+}:Y_2SiO_5 at 10 K. A Lorentzian lineshape fit yielded full width half maxima of 475.94 MHz and 463.66 MHz for $E \parallel D_2$ and $E \perp D_2$ polarizations, respectively.

and the horizontal laser polarization are shown in figure 4.10. The absorption for the $E \parallel D_2$ polarization was twofold greater than for the crystallographic site 1, while for $E \perp D_2$ the absorption was slightly less than for site 1. Additionally, the FWHM for $E \parallel D_2$ was determined to be 606.34 MHz, while for $E \perp D_2$ polarization a FWHM of 584.58 MHz was obtained. While somewhat larger, the linewidths observed here are of the same order as the linewidth of 390 MHz reported for the $^4I_{15/2}Z_1 \rightarrow {}^4I_{13/2}Y_1$ transition of a 50 ppm Er^{3+}:Y_2SiO_5 sample by Böttger *et al.* [38].

The observed linewidths can be primarily attributed to inhomogeneous broadening. Inhomogeneous broadening is the result of strain in the crystalline environment to a mismatch in ionic radii of the host atom and the substituted dopant ions. This leads to different Er^{3+} ions experiencing a slightly different Stark shift due to the crystalline host, which manifests itself as a broadening of the collective linewidth. Compared to typical rare-earth doped insulators, the observed inhomogeneous linewidths of a few hundred MHz are exceptionally narrow [128, 129].
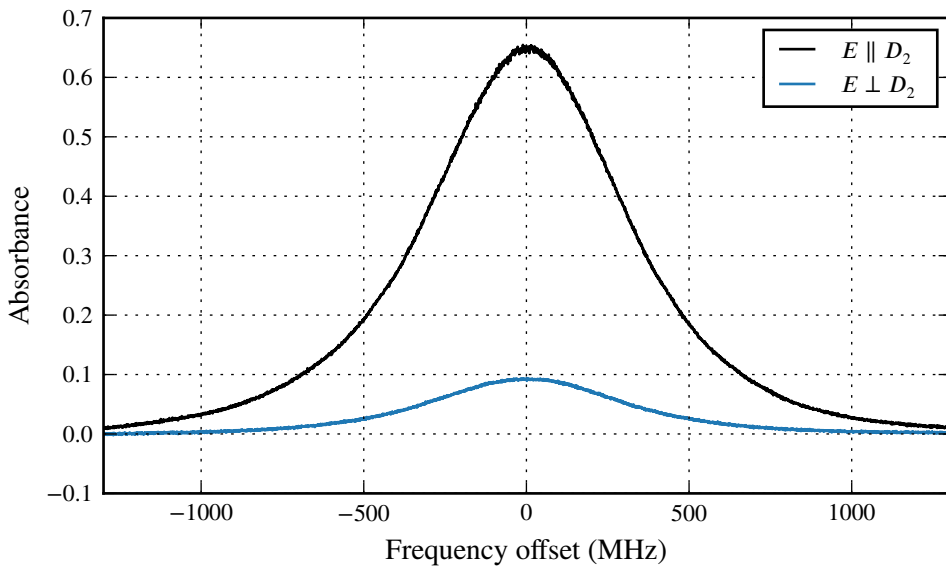
Figure 4.10: Site 2 laser absorption measurement for both vertical and horizontal polarization of the $^4F_{9/2} \rightarrow {}^4I_{15/2}$ transition for the crystallographic site 1 of 50 ppm Er^{3+}:Y_2SiO_5 at 10 K. A Lorentzian lineshape fit yielded full width half maxima of 606.34 MHz and 584.58 MHz for $E \parallel D_2$ and $E \perp D_2$ polarizations, respectively.

This can be attributed to both the low dopant concentration employed and due to the relatively small a mismatch in ionic radii between the Y^{3+} ions and the substituted Er^{3+} ions. Additionally, at this very low dopant concentration the inhomogeneous linewidth is strongly dependent on growth rate and purity of precursor materials.

4.4 Zeeman study of the $^4F_{9/2}D_1$ level

A magnetic field dependent laser transmission experiment was performed in order to obtain the *g*-value of the $^4F_{9/2}D_1$ excited state along the crystallographic *b* axis. The application of an external magnetic field results in a splitting of each state thereby lifting the Kramers degeneracy. This leads to a total of four transitions between the lowest energy state of the ground state and the lowest energy state of the $^4F_{9/2}$ term for a magnetic field coincident with the crystallographic *b* axis or within the D_1-D_2 plane. For a general magnetic field orientation this would
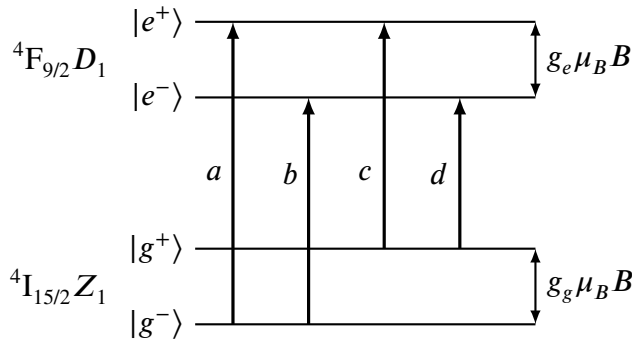
Figure 4.11: Labels of the lowest energy transitions between the $^4I_{15/2} \rightarrow {}^4F_{9/2}$ multiplets with the Kramers degeneracy lifted by an external magnetic field.

double to a total of eight transitions since each crystallographic site is composed of two magnetically inequivalent orientations of ions.

We adopt the transition labelling scheme of reference [38] to the $^4F_{9/2}$ term, which is summarized in figure 4.11. By inspection of the splittings shown in figure 4.11 it is readily apparent that the $^4I_{15/2}Z_1$ g-value can be expressed in terms of transition energies according to the following equation

$$g_g = \frac{E_a - E_c}{\mu_B B} = \frac{E_b - E_d}{\mu_B B}.$$ (4.1)

Similarly, the $^4F_{9/2}D_1$ excited-state g-value can be specified by

$$g_e = \frac{E_a - E_b}{\mu_B B} = \frac{E_c - E_d}{\mu_B B}.$$ (4.2)

In both of the above equations, B is the applied field strength and μ_B is the Bohr magneton.

Thus, the g-value along a specific axis for both the ground and excited state can be determined by recording the field dependence of a specific transition between two split Kramers doublets. Since both crystallographic sites Y_1 and Y_2 are of C_1 symmetry, it is not possible to infer anything about the orientation of the principal components of the g-tensor with respect to the crystallographic axes. In order to determine the full g-tensor, complete rotation patterns are required, as were performed for the $^4I_{13/2}$ states by Sun *et al.* [39]. While this is beyond the scope of

the present work, the observation of a single *g*-value in a previously unmeasured multiplet is nevertheless of value for the crystal-field fit performed in section 4.6.

Figure 4.12 shows the field dependence of the Y_1 crystallographic site measured at 4.2 K using the in-house built superconducting cold-finger magnet. All measurements were performed using the 50 ppm Er^{3+}:Y_2SiO_5 sample oriented with both the laser and the magnetic field parallel to the crystallographic *b* axis. Furthermore, the laser polarization was adjusted with a half-waveplate for maximum absorption, that is, $E \parallel D_2$. It should be noted that these measurements were performed prior to the implementation of a balanced detector. Thus, direct transmission was instead measured with a Newfocus 1801-FS photoreceiver, while a laser power baseline was recorded with a Thorlabs PDA36A.

Due to the 20 GHz maximum mode-hop free tuning range of the probe laser, it was necessary to perform scans split into multiple segments for Zeeman splittings that exceeded this range. Segments were chosen so as to have overlapping spectral features, which could be exploited for aligning the scan ranges of individual segments. In order to determine the centers of the observed absorption lines, Lorentzian lineshapes were fit to the individual peaks, from which it was possible to infer the effective Zeeman splitting. The power of the scan laser was 0.14 mW with each frequency segment swept out in 1 ms. A total of 250 individual transmission spectra were averaged for each segment using a repetition rate of 10 Hz.

The transitions *a* and *d* can readily be identified in figure 4.12 since they correspond to the highest and lowest energy transitions, respectively. In order to distinguish the transitions *b* and *c* it is necessary to conduct a temperature dependent study to identify the depletion of the $|g^+\rangle$ state at low temperature. However, since previous studies have determined the ground-state *g*-tensors, both from EPR studies [37] as well as optical spectroscopy [39], it is possible to express the excited-state *g*-value in terms of the *a* and *d* splitting in addition to the ground-state *g*-factor. Rearranging equations (4.1) and (4.2), one obtains the following expression:

$$g_e = \frac{E_a - E_d}{\mu_B B} - g_g. \tag{4.3}$$

In order to apply equation (4.3) we first require the effective *g*-factor along the crystallographic *b* axis. This was determined to be 8.84 for site Y_1 using the full
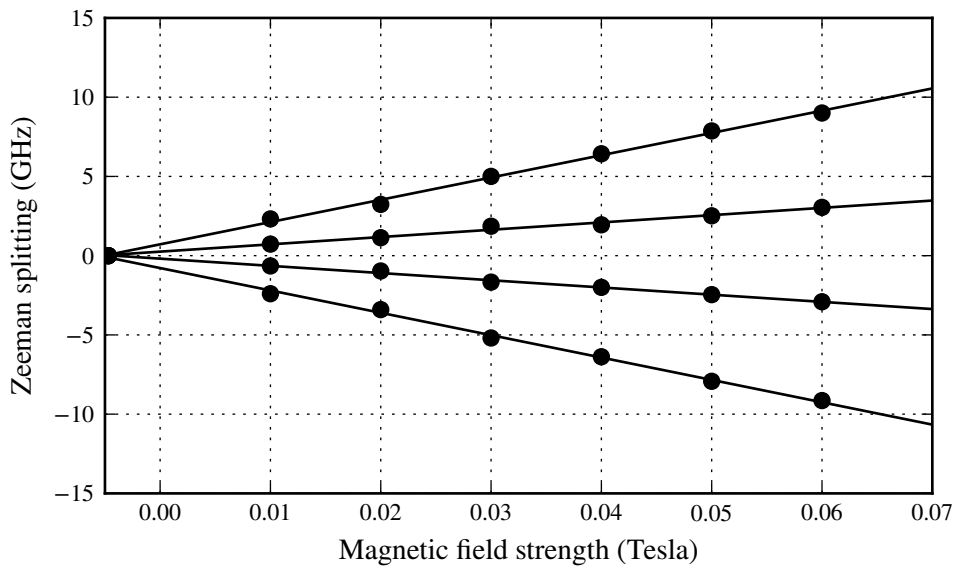
Figure 4.12: Zeeman splitting of the four transitions *a*, *b*, *c*, and *d* shown in figure 4.11 for the crystallographic site Y_1. Solid points represent experimental splittings while solid lines correspond to a linear least-squares fit. The sample was at 4.2 K, with the magnetic field applied along the crystallographic *b* axis. The zero offset is due to a small residual field that is always present in the magnet.

ground-state *g*-tensor reported by Sun *et al*. [39]. Consequently, by performing a least-squares fit for the Zeeman splitting shown in figure 4.12 to determine the effective splitting $E_a - E_d$, equation (4.3) can be employed to yield the effective *g*-factor value of 11.28 for the $^4F_{9/2}D_1$ level.

Figure 4.13 shows an analogous external field dependence along the crystallographic *b* axis for spectroscopic site Y_2 obtain with an identical setup to that described for site Y_1. By again using the published ground-state *g*-tensor the effective ground-state *g*-factor along the *b* axis was found to be 2.76, which with recourse to equation (4.3) yields an excited-state *g*-factor of 1.05 for the $^4F_{9/2}D_1$ level.

Thus we have determined the effective *g*-factors of the $^4F_{9/2}D_1$ state along the *b* axis for both crystallographic sites. While only for a single orientation, this measurement yielded an additional data point for a previously uncharacterized multiplet, thus complementing the very detailed data available for the $^4I_{15/2}$ and
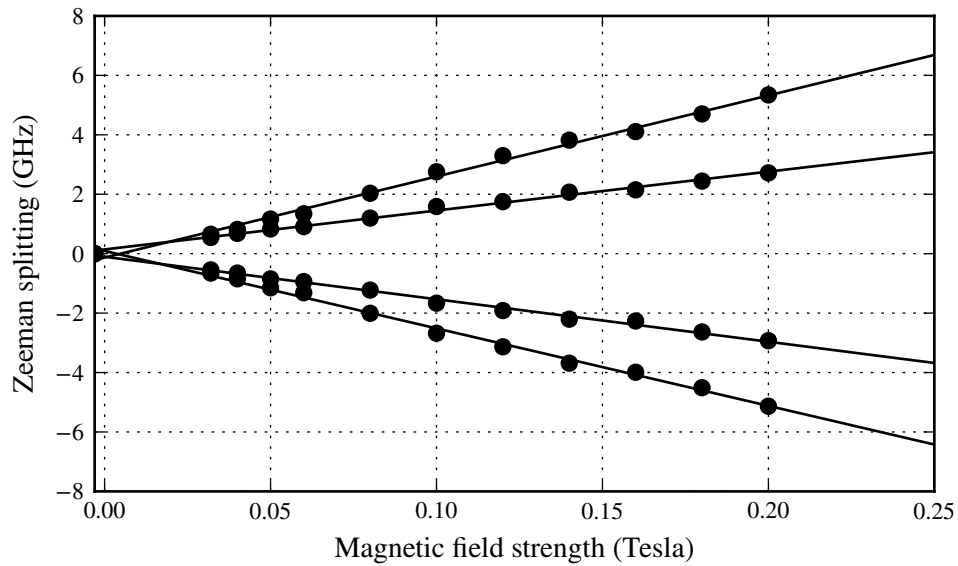
Figure 4.13: Zeeman splitting of the four transitions *a*, *b*, *c*, and *d* shown in figure 4.11 for the crystallographic site Y_2. Solid points represent experimental splittings while solid lines correspond to a linear least-squares fit. The sample was at 4.2 K, with the magnetic field applied along the crystallographic *b* axis. The zero offset is due to a small residual field that is always present in the magnet.

$^4I_{13/2}$ multiplets [37, 39].

4.5 Spectral hole-burning

We now turn to discuss the physical mechanisms involved in a SHB experiment. As we noted in the previous section, a direct laser transmission experiment is limited in resolution by the inhomogeneous linewidth, that is, the collective linewidth of the ensemble of ions shifted by perturbations due to the crystal field. The true dynamic linewidth associated with the transition, the homogeneous linewidth, is not resolvable. Additionally, hyperfine splittings for $^{167}Er^{3+}$ are ~ 100 MHz, whereas the inhomogeneous linewidth is ~ 1 GHz. Therefore, it is not possible to directly resolve the hyperfine spectrum by using absorption or excitation spectroscopy. However, both the homogeneous linewidth and the hyperfine splittings can, in principle, be determined using SHB spectroscopy.

In order to perform the SHB technique, a single frequency laser is employed to provide an excitation pulse tuned within the frequency range of the inhomogeneous linewidth. This will excite electrons in the subset of ions that have resonant transitions coincident with the pump frequency. Consequently, the resonant subset of ions will experience a depletion of electrons in the ground state, which can be detected by the application of a probe pulse that is swept in frequency. This depletion of electrons is detected by an increase in transmission of the probe pulse, which is referred to as a spectral hole. The precise form of this experiment depends on the storage mechanism which prevents excited electrons from relaxing back to the ground state prior to the application of the probe pulse. The pulse sequence and its defining parameters are schematically shown in figure 4.4.

The simplest case consists of electron storage in a long-lived excited state. However, there are several additional storage mechanisms that have been observed in RE^{3+} ion doped crystals. Among them is storage in Zeeman split levels, hyperfine state storage, and super-hyperfine state storage [16]. While this type of experiment can in some instances be employed to determine hyperfine and super-hyperfine levels, it additionally enables the study of dephasing dynamics due to nuclear spin flips in both the RE^{3+} ion as well as the ligands. Consequently, this experimental technique is not only of value for determining the energy level structure, but can be employed to study the dephasing dynamics of potential storage levels. This is particularly the case when coupled with techniques such as photon echoes [40, 42, 119].

For clarity, we will canvas the details involved in a hole-burning experiment by considering a Zeeman split doublet. This will greatly simplify the number of transitions one has to deal with, yet the basic principles discussed are nevertheless equally applicable to experiments dealing with storage in hyperfine levels. When an external field is applied to an erbium ion the degeneracy of Kramers levels in both the ground and excited state is completely lifted. Thus, for the previously consider $^4I_{15/2}Z_1 \rightarrow {}^4F_{9/2}D_1$ splitting, there are four possible transitions that can be resonant with an applied pump pulse. Figure 4.14 (a) defines these transitions, with transition *a* in resonance. Provided that the lifetime of the level $|g^+\rangle$ is greater than the optical lifetime of the $^4F_{9/2}$ state, electrons are stored in the upper ground-state level $|g^+\rangle$. Thus, when the probe pulse is applied in this scenario, both transitions originating from the $|g^-\rangle$ level will result in holes, whereas
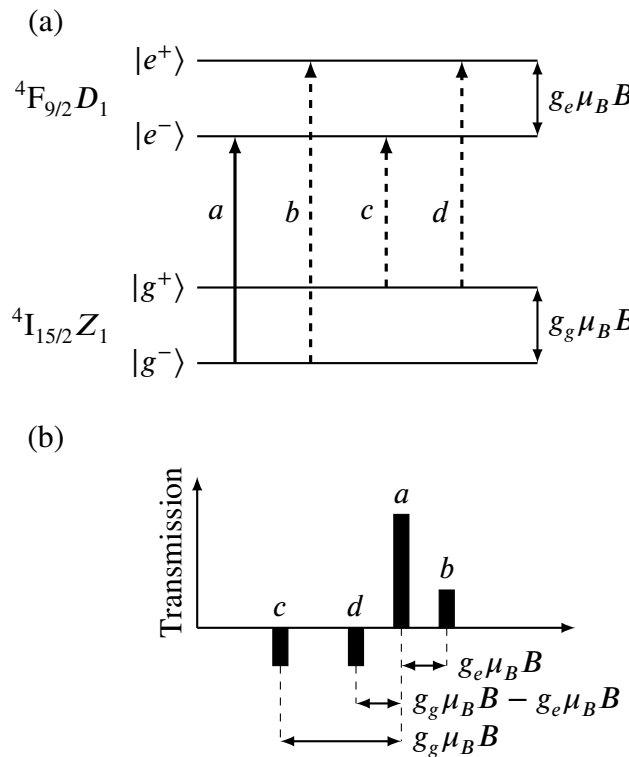
Figure 4.14: Four-level hole burning with the burn laser in resonance with the $|g^-\rangle \rightarrow |e^-\rangle$ transition (solid line). All four transitions are swept over by the probe laser. For ions in a crystal host, the burn laser would be in resonance with each of the transitions for a subset of ions due to inhomogeneous line shifts; thus, the resulting burn pattern would show two side holes, along with several anti-holes.

at frequencies corresponding to transitions that originate from the $|g^+\rangle$ state one would observe an increase in absorption, referred to as an anti-hole. Figure 4.14 (b) is a graphical representation of the hole/anti-hole pattern one would observe in the case of Zeeman level storage [130]. For a realistic sample with inhomogeneously shifted transitions, the hole/anti-hole pattern would be more complex, since the pump pulse would be in resonance with four different classes of ions. However, provided each transition is excited in some subset of ions, it is possible to reconstruct both the ground and excited-state splittings from the observed hole/anti-hole pattern.

In the case of hyperfine splittings of $^{167}Er^{3+}$, with nuclear spin $I = 7/2$, there are a total of 256 ion classes that can be in resonance with the burn pulse. This

leads to a very complex hole-burning pattern, the interpretation of which is additionally complicated since the complete hyperfine pattern is broader than the inhomogeneous linewidth. Consequently, not all 256 ion classes can be excited with the burn pulse frequency tuned within the inhomogeneous linewidth. Yet by altering the burn pulse frequency, one inadvertently changes the hole/anti-hole pattern, since a different subset of ions is then in resonance with the pump pulse. This makes it difficult to fully characterize the entire hole/anti-hole pattern when the total hyperfine splitting exceeds the inhomogeneous linewidth. Nevertheless, by employing SHB in conjunction with simulated hyperfine patterns, it may be possible to identify individual levels and thus validate the crystal-field analysis.

4.5.1 Excited-state storage

The dominant electron storage mechanism for SHB of the ${}^4F_{9/2}D_1$ state proved to be the long-lived excited state ${}^4I_{13/2}$. Hole burning was performed on the 50 ppm $Er^{3+}{:}Y_2SiO_5$ sample, with the laser parallel to the b axis, and the polarization adjusted such that $E \parallel D_2$. All measurements in this section were performed using the Oxford Instruments SpectroMag cryostat, with temperature above 4.2 K regulated by maintaining a positive pressure in the sample cell. Furthermore, the maximum burn pulse power was 5.2 mW, which was applied for a length of 50 ms, while the chirp pulse power was 0.1 mW, which was applied for a duration of 1 ms. The pulse sequence repetition rate was set to 0.2 Hz.

Figure 4.15 shows a temperature dependence study of the hole lifetime observed by tuning the burn laser frequency to the center of the inhomogeneous linewidth for the crystallographic site Y_1. This corresponds to a wavelength of 659.080 ± 0.006 nm (in air). Figure 4.15 shows, in addition to the temperature dependent hole intensities, a representative transmission profile showing the spectral hole, burned at the center of the inhomogeneous lineshape. Furthermore, the bottom right-hand panel shows the difference of the central hole after subtraction of the reference lineshape, which was obtained by performing a chirp probe without a burn pulse. This panel also shows the fit of a Lorentzian lineshape used to determine the depth of the burned hole. The central hole lifetimes were determined by fitting a linear function to the log of the decay curves. This yielded a lifetime of 9.6 ± 0.5 ms, which, within the uncertainty of the measurement, was constant
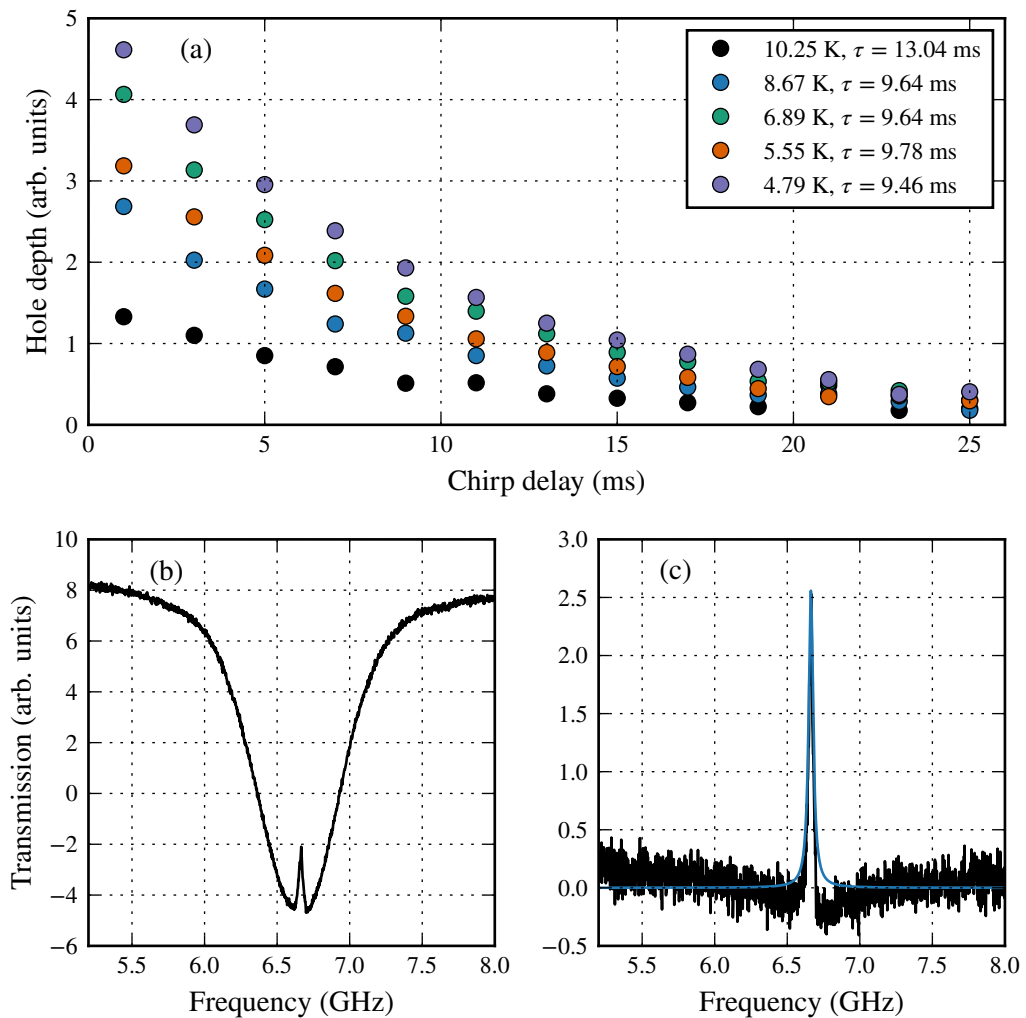
Figure 4.15: (a) Temperature dependence of chirp delay with fitted hole lifetimes crystallographic Y_1 of Er^{3+}:Y_2SiO_5. (b) A representative transmission spectrum with the central hole, in this instance, for a chirp delay of 3 ms and a temperature of 5.55 K. (c) The difference between the trace on the left panel and a reference trace obtained by performing a chirp probe without a burn pulse. Additionally, this panel shows the Lorentzian fit performed to obtain the hole depth.

over the temperature range explored. The exception to this is the 10.25 K measurement; however, this outlier was attributed to the spectral hole becoming only marginally resolvable at this temperature, which substantially impaired the accuracy of the Lorentzian fits. The lifetime of the central hole is consistent with the reported value of the $^4I_{13/2}$ excited-state lifetime of $T_1 = 11.4$ ms at 10 K [38]. This corroborates the assumption that the principal storage mechanism for the central hole is in the $^4I_{13/2}$ excited state.

Analogous measurements were performed for the second crystallographic site Y_2, at a central wavelength of 657.927 ± 0.006 nm (in air). The results are summarized in figure 4.16. We note that the improvement of the signal-to-noise ratio is due to the absorption of this site being almost double compared to site 1 for a polarization of $E \parallel D_2$. The central hole lifetime was found to be slightly shorter for this site, corresponding to 7.2 ± 0.5 ms for the studied temperature range. This is again consistent with the reported excited-state lifetime of $T_1 = 9.20$ ms at 10 K [38].

The difference in ~ 2 ms of the hole lifetimes with respect to the excited-state storage lifetimes is attributed to a direct decay from the $^4F_{9/2}$ multiplet to the ground state, thus bypassing the $^4I_{13/2}$ bottle-neck. Additionally, spectral diffusion induced by spin flips of neighboring erbium-ion valance electrons may partially contribute to this shortening in lifetimes. A similar effect to this has been previously observed in Er^{3+}:$LiYF_4$, albeit on a much shorter timescale of 200 μs [131]. The authors of reference [131] argued that the dominant cause of spectral diffusion was the result of fluorine nuclear spin flips in the $LiYF_4$ host; the longer time scales observed in our measurement would be consistent with this interpretation, due to the much smaller nuclear moments of the Y atoms in our host material.

Following reference [131], this interpretation was corroborated by a time resolved hole-burning study of both spectroscopic sites at 1.5 K. It was found that the holewidth increased by up to a factor of two between a chirp delay of 1.0 ms and 17.0 ms. This is principally attributed to spectral diffusion due to spin flips of neighboring erbium-ion valance electrons. Figure 4.17 graphically shows this result by plotting the holewidth with respect to chirp delay for both crystallographic sites. It is evident that the uncertainty of the fitted linewidth increase substantially for longer delays, which makes a more quantitative analysis difficult. In order to establish a more precise timescale it would be necessary to perform such measure-
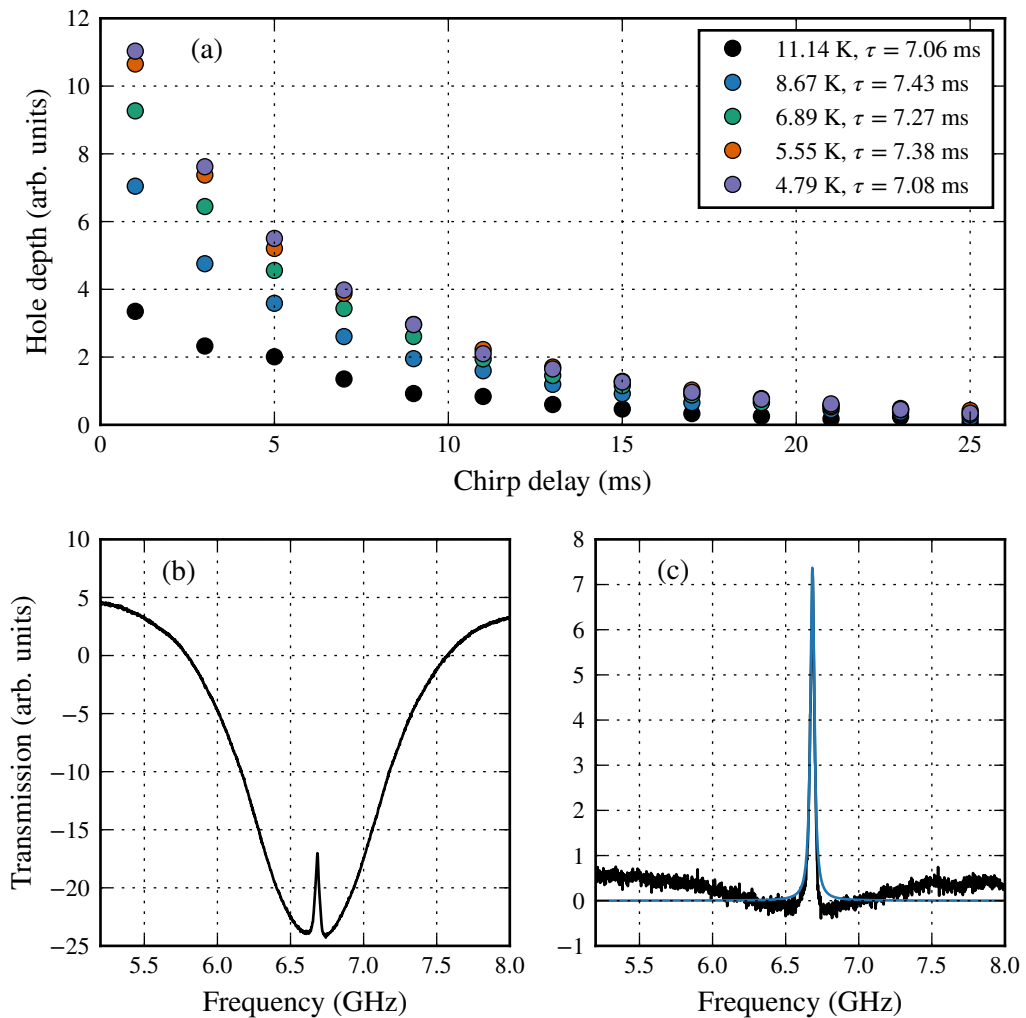
Figure 4.16: (a) Temperature dependence of chirp delay with fitted hole lifetimes for crystallographic Y_2 of Er^{3+}:Y_2SiO_5. (b) A representative transmission spectrum with the central hole, in this instance, for a chirp delay of 3 ms and a temperature of 5.55 K. (c) The difference between the trace on the left panel and a reference trace obtained by performing a chirp probe without a burn pulse. Additionally, this panel shows the Lorentzian fit performed to obtain the hole depth.

ments for shorter chirp delays, since this would yield an improved hole-depth to which the fitting of Lorentzian lineshapes would be easier to achieve with high accuracy.
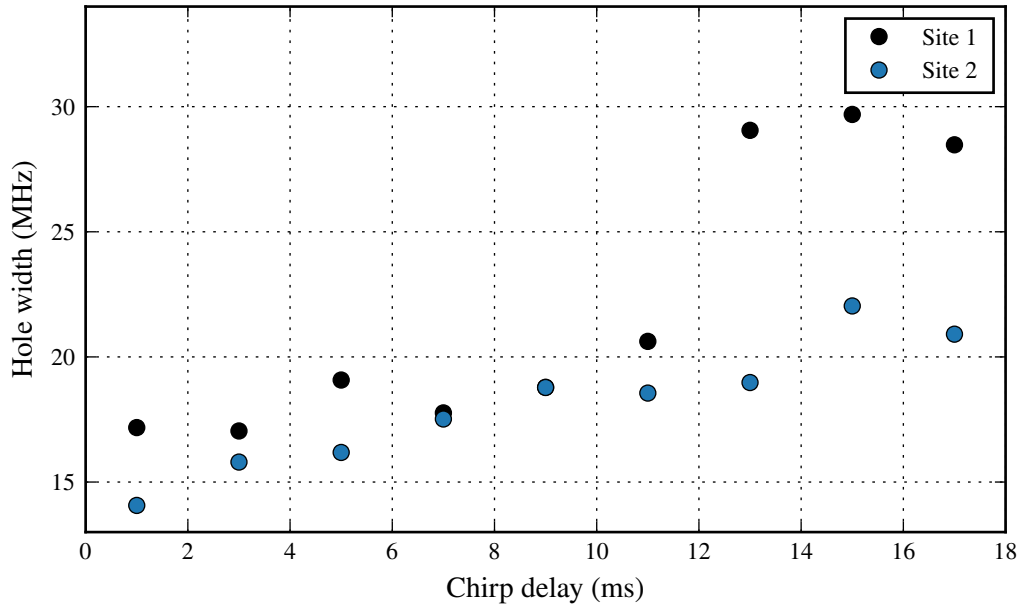
Figure 4.17: Central hole width with $^4I_{13/2}$ level storage with respect to chirp delay. A broadening of almost a factor of two can be observed for both spectroscopic sites Y_1 and Y_2. This instantaneous spectral diffusion is attributed to nuclear spin flips in the host lattice.

4.5.2 Hyperfine level storage

We now turn to investigate the presence of hyperfine level storage. The initial approach taken was to use FM spectroscopy in order to potentially resolve holes or anti-holes due to ground-state hyperfine levels. Given the better signal-to-noise ratio of the crystallographic site Y_2, all initial investigative experiments were performed for this site. Figure 4.18 shows the FM absorption signal at zero field, with the burn laser tuned to the center of the inhomogeneous lineshape. The sample was at 1.5 K, with the burn pulse length set to 100 ms, the chirp delay set to 1.0 ms, and a pulse sequence repetition rate of 1.0 Hz. While the structure to the either side of the central hole may be attributable to electron depletion of individual

hyperfine levels, it is difficult to argue with any confidence. This could potentially be improved by altering the FM modulation frequency, or by moving longer burn pulses.

Even though hyperfine levels were not directly observed in FM spectroscopy, long term storage in the ground-state hyperfine levels could be inferred from an enhancement in absorption across the entire inhomogeneous lineshape of the transmission signal when compared to a reference scan. This effect can be clearly seen in figure 4.19, where the difference between the SHB signal and the reference signal yields a very broad anti-hole. The origin of this is assumed to be the convolution individual of anti-holes, which form due to electron storage in the ground or excited-state hyperfine levels. Long term storage in ground-state hyperfine levels has previously been observed in a number of systems [48, 132–135]; this includes storage times as long as 100 s in Pr^{3+}:Y_2SiO_5 and exceeding 20 days
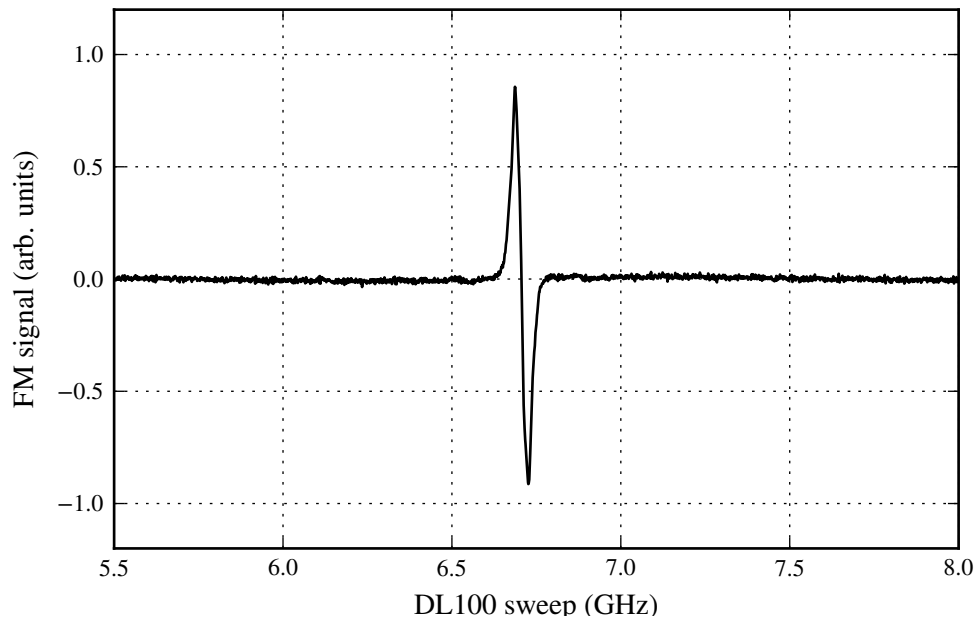
Figure 4.18: FM spectroscopy trace for crystallographic site Y_2 of Er^{3+}:Y_2SiO_5 at 1.5 K. The laser, which was tuned to the center of the inhomogeneous lineshape, was applied for 100 ms, and a chirp delay of 1 ms was employed. While possible hyperfine structure may be marginally visible, no clear signal could be obtained.
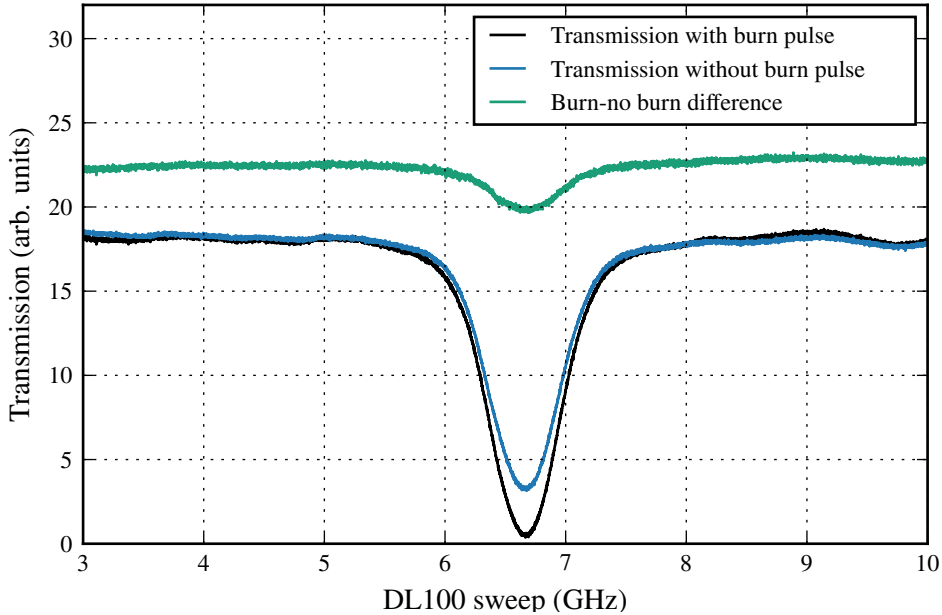
Figure 4.19: Broad anti-hole due to ground-state hyperfine level storage for crystallographic site Y_1 of Er^{3+}:Y_2SiO_5, with the sample at 1.5 K. The burn pulse was applied for the duration of 1 s, with the subsequent chirp pulse delayed by 500 ms. Pulse sequence was applied with a repetition rate of 0.2 Hz.

in Eu^{3+}:Y_2SiO_5. Further evidence of hyperfine storage can be seen in figure 4.20, which is a repeated measurement of figure 4.19 for spectroscopic site Y_2. This clearly reveals that the observed anti-hole corresponds to a convolution of individual lineshapes.

To our knowledge, all previous reports of hyperfine storage for an erbium-doped material were performed with an external magnetic field. This stems from the fact that the principal cause for both hole filling as well as spectral diffusion is due to electron spin flips of nearby Er^{3+} ions [119, 131]. In order to gain a better understanding of the mechanisms responsible for the observed anti-holes, a number of temperature dependent lifetime measurements were performed. Figures 4.21 and 4.22 show the resulting decay curves for spectroscopic sites Y_1 and Y_2, respectively. While the resolution is evidently insufficient to establish a clear temperature trend, for the parameter space measured here, an average lifetime of 1.6 ± 0.4
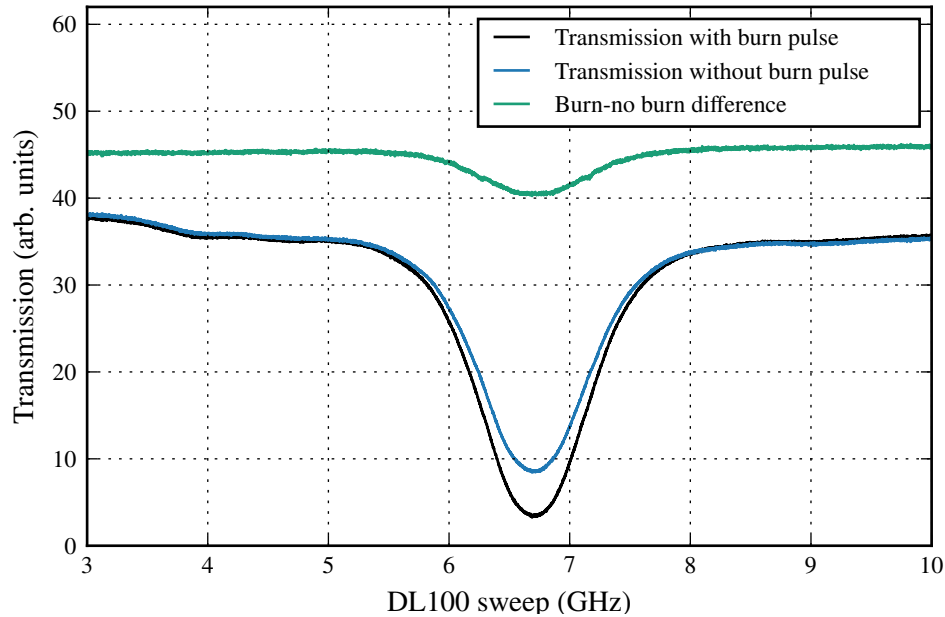
Figure 4.20: Visible hyperfine levels for crystallographic site Y_2 of Er^{3+}:Y_2SiO_5, with the sample at 1.5 K. The burn pulse was applied for the duration of 1 s, with the subsequent chirp pulse delayed by 500 ms. Pulse sequence was applied with a repetition rate of 0.2 Hz.

seconds can be ascertained for both spectroscopic sites.

This work was complemented by a brief study of the anti-hole lifetime in an external magnetic field. Figure 4.23 shows the lifetime at zero field as well as 0.5 Tesla and 1.0 Tesla, for spectroscopic site Y_1 at a temperature of 1.5 K.

As is clearly evident from the figure, the application of an external field has a very pronounced effect. Counter to what is typically reported [48, 132, 133], rather than increase the storage efficiency, the application of an external field almost entirely eliminates the observed hyperfine storage. While the indicated lifetimes are substantially shorter at non-zero field, the uncertainty associated with fitting a Lorentzian lineshape to a very small peak is considerable. The most plausible explanation for the observed drastically reduced storage efficiency is that the application of an external field results in an admixture of the ground and excited-state wavefunctions. This, by way of selection rules, substantially reduces the branching ratios whereby electrons can be pumped to the long-lived hyperfine levels. An
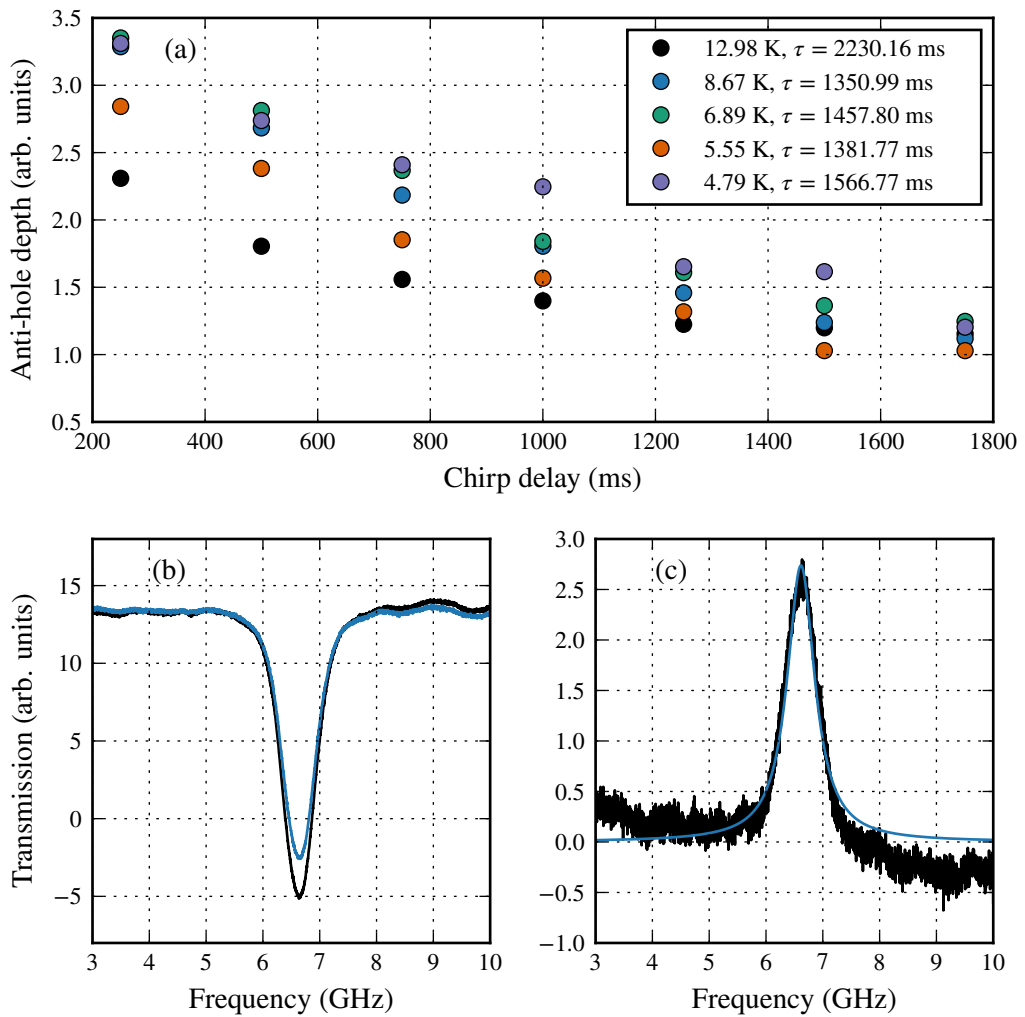
Figure 4.21: (a) Temperature dependence of chirp delay with fitted hyperfine storage lifetimes for crystallographic Y_1 of Er^{3+}:Y_2SiO_5. The burn length was 1 s, with the pulse sequence repetition rate set to 0.2 Hz. (b) A typical transmission spectrum (black) and the reference scan for which no burn pulse was applied (blue). This example corresponds to a chirp delay of 500 ms at a temperature of 4.79 K. (c) The difference between the trace on the left panel and a reference trace obtained by performing a chirp probe without a burn pulse. Additionally, this panel shows the Lorentzian fit performed to obtain the hole-depth.

investigation of the central hole FWHM reveals that the application of an external field reduces the linewidth to 1 MHz or less, which corresponds the resolution
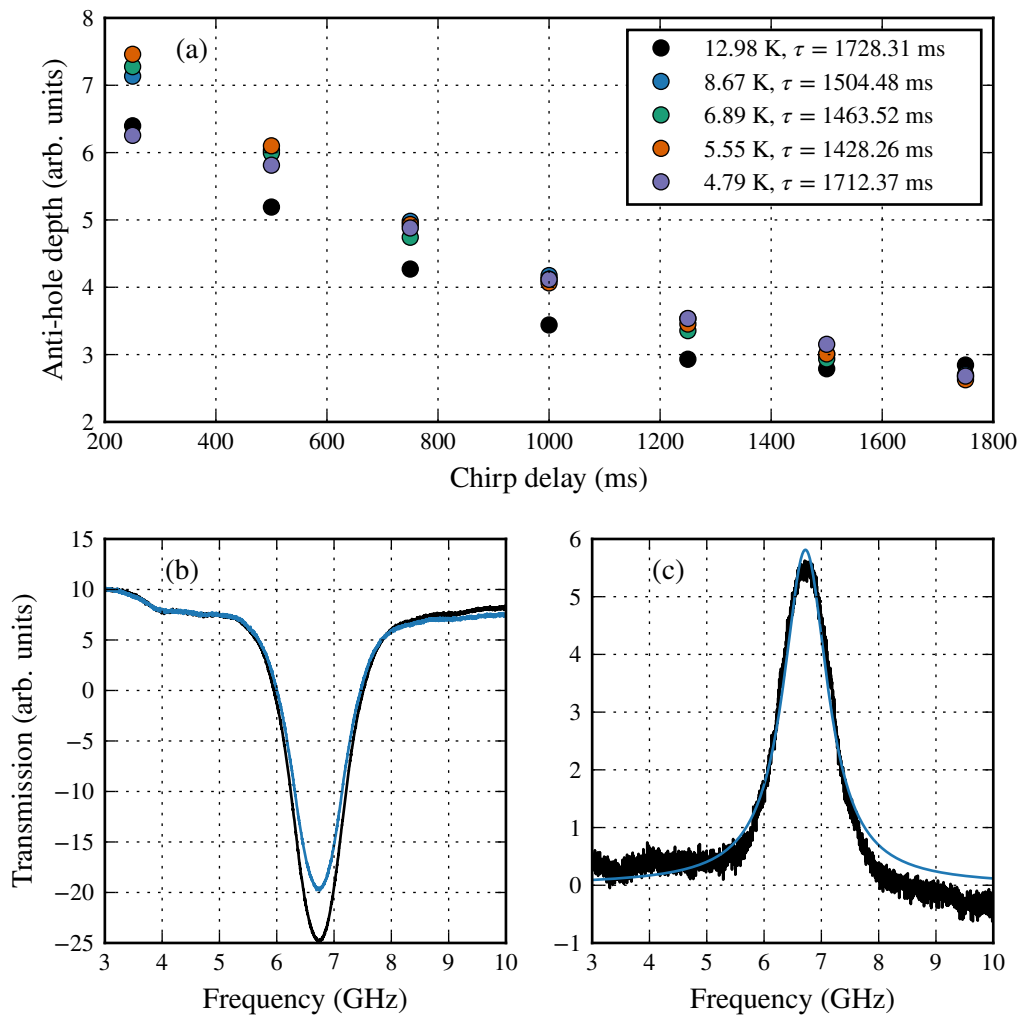
Figure 4.22: (a) Temperature dependence of chirp delay with fitted hyperfine storage lifetimes for crystallographic Y$_2$ of Er^{3+}:Y$_2$SiO$_5$. The burn length was 1 s, with the pulse sequence repetition rate set to 0.2 Hz. (b) A typical transmission spectrum (black) and the reference scan for which no burn pulse was applied (blue). This example corresponds to a chirp delay of 500 ms at a temperature of 4.79 K. (c) The difference between the trace on the left panel and a reference trace obtained by performing a chirp probe without a burn pulse. Additionally, this panel shows the Lorentzian fit performed to obtain the hole-depth.

limit imposed by the DL100 laser linewidth. This indicates that, consistent with what one expects, the instantaneous spectral diffusion is substantially reduced by
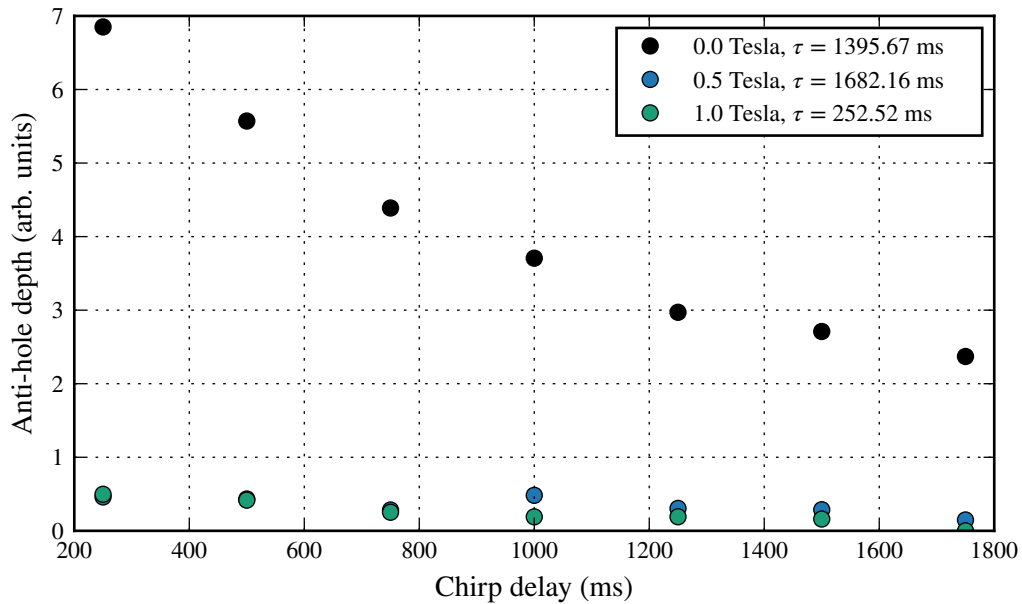
Figure 4.23: External magnetic field dependence of hyperfine storage lifetimes for crystallographic Y_1 of $Er^{3+}:Y_2SiO_5$. The burn length was 1 s, with the pulse sequence repetition rate set to 0.2 Hz, and the sample cooled to 1.5 K.

the external field. This supports the hypothesis that the actual anti-hole lifetime is not reduced, but rather that the likelihood of electron transfer to hyperfine states is reduced.

Finally, the observed hyperfine level storage was investigated with respect to the burn-pulse repetition rate and burn power. This was originally done in order to establish an optimal burn power regime and a repetition rate so as to ensure the sample effectively relaxes between subsequent pulse sequences. Figure 4.24 shows this parameter space for the second spectroscopic site, at a temperature of 2.0 K. As expected from the lifetime studies, at fast repetition rates there is an increased optical pumping to the hyperfine states. Similarly, it is evident that there is a dependence on optical burn power; however, somewhat unexpected, for a burn power of 1.08 mW the anti-hole effectively disappears, irrespective of the pulse sequence repetition rate. One would expect that a fast repetition rate effectively compensates for a reduced power of individual burn pulses. This suggests that the
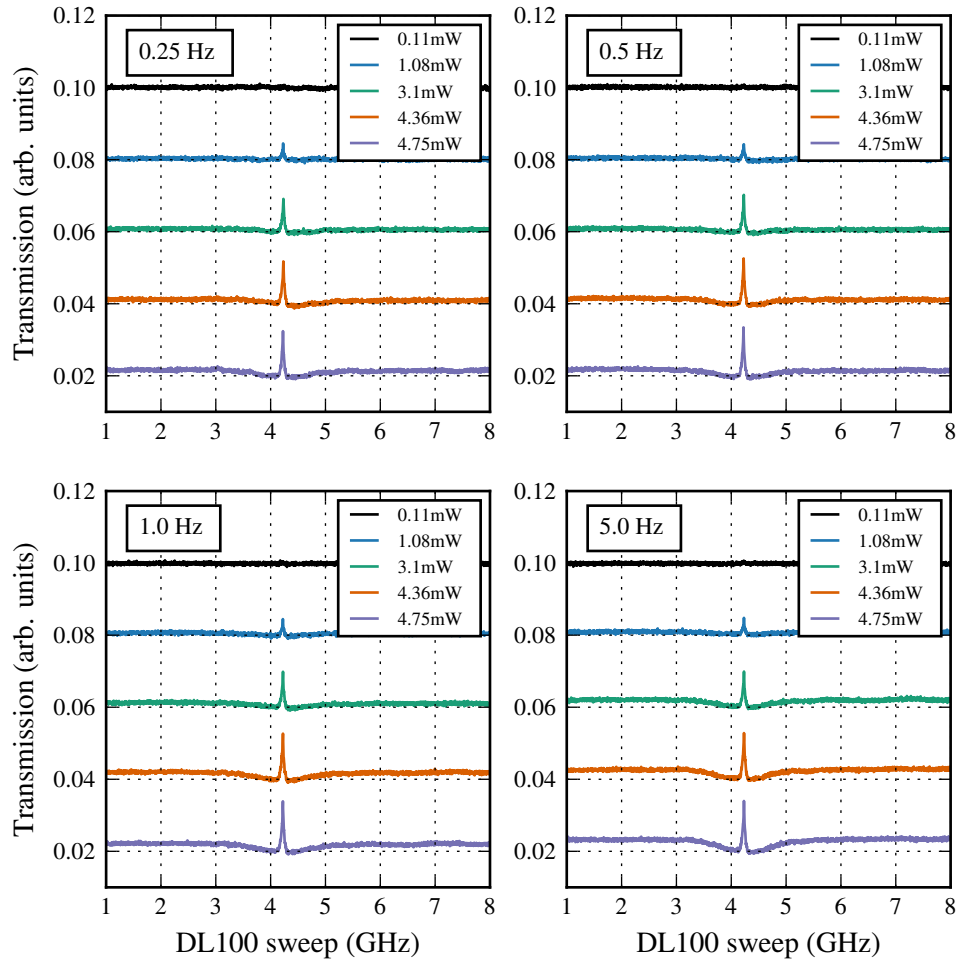
Figure 4.24: Pulse-sequence repetition rate and burn-power dependence for crystallographic site Y_2 of Er^{3+}:Y_2SiO_5.

storage mechanism has a non-linear dependence on optical burn power.

4.6 Crystal-field analysis

The crystal-field analysis of Er^{3+}:Y_2SiO_5 was performed using the "multi-Hamiltonian fit" described in section 3.2. By employing energy-level data, as well as ground state and first-excited state magnetic data, it was possible to reproduce the experimental energy level spectrum reported by Doualan *et al*. [117].

This section effectively proceeds in the same order as the analysis was performed. Results are initially shown for a calculation which includes energy level data and ground/first-excited state g-value data in the form of theoretical rotation patterns for the $^4I_{15/2}Z_1 \rightarrow {}^4I_{13/2}Y_1$ transition. Thereafter, the method employed to fit to ground-state hyperfine EPR data is discussed, and the resulting fits are presented.

Both substitutional sites Y_1 and Y_2 of Er^{3+}:Y_2SiO_5 have a C_1 point-group symmetry. The crystal-field Hamiltonian appropriate for such a site has the form:

$$H_{CF} = \sum_{k,q} B_q^k C_q^{(k)}, \tag{4.4}$$

for $k = 2, 4, 6$ and $q = -k \cdots k$. Additionally, all non-axial parameters B_q^k with $q \neq 0$ are complex with $B_{\pm q}^k = X_q^k + iY_q^k$, where both X_q^k and Y_q^k real. Thus, the crystal-field Hamiltonian H_{CF} contains a total of 27 parameters. As part of the crystal-field fit, we further varied the Slater parameters of the free-ion Hamiltonian, F^2, F^4, and F^6; as well as the spin-orbit coupling parameter, ζ. As will be explained below, a subset of the Hamiltonians employed also account for hyperfine and nuclear quadrupole interactions. In these instances, the additional a_l and a_Q parameters were varied during the fit. This yields a total of 33 parameters that were varied in order to obtain the final set of parameters. All remaining parameters in the free-ion Hamiltonian (2.27) were fixed to values obtained from the literature [67] throughout the optimization.

The fitting was performed in stages, with initial calculations fitting to energy level data up to the $^2H_{11/2}$ multiplet published by Doualan *et al*. [117] and to Zeeman data of the $^4I_{15/2}Z_1$ and $^4I_{13/2}Y_1$ states reported by Sun *et al*. [39]. To account for the magnetic field dependence, the published g-tensors were employed to generate synthetic energy level splittings for a field of 0.484 Tesla (the experimental field strength quoted in reference [39]). Sets of Zeeman splittings were calculated

for a rotation of this field in the D_1-D_2 plane, the $D_2 - b$ plane, and the $b - D_1$ plane, for angles of rotation of $\pi/8$, $\pi/4$, $3\pi/4$, as well as with zero rotation. The fit of the resulting energy level differences was implemented by considering each orientation as a separate Hamiltonian. By application of the basinhopping algorithm and the NLopt bobyqa local minimization routine, an excellent fit was obtained for both spectroscopic sites. Interestingly, an optimal fit could only be achieved by use of the complete matrix elements spanning the full $4f^{11}$ configuration, indicating that second order crystal-field effects played a non-negligible role. Additionally, it was found that the inclusion of the M^i and P^i parameters, which accommodate higher-order spin-dependent effects, were also essential for an optimal fit to the Zeeman data.

This was followed by the inclusion of the $^4F_{9/2}$ g-factor measurements discussed in section 4.4 for the crystallographic b axis. For site Y_1 it proved to be difficult to achieve an accurate agreement to both the g-factor measured here as well as the published data by Sun *et al*. This was primarily attributed to a possible misalignment of the crystal within the cryostat during the Zeeman measurement. For the magnet employed in this measurement, accurate alignment of the crystal axes within the field was difficult. It is hoped that these initial measurements can be followed up with the recently acquired Oxford SpectroMag cryostat, which has sufficient space to allow for a sample mount capable of a rotation within the field. A complete rotation pattern would allow any small misalignment to be compensated for during the data analysis, something which is not possible for a g-factor measurement along a single axis. In order to reconcile this, the weighting of the χ^2 contribution due to the $^4F_{9/2}$ g-value was substantially reduced compared to the remaining data.

In order to compare the accuracy of the crystal-field fit for an arbitrary magnetic field orientation, matching rotation pattern plots were produced to those presented by Sun *et al*. [39]. However, rather than experimental data, here the circles denote data simulated using the published g-tensors, whereas the solid line represents the transition energy predicted by the crystal-field simulation. These rotation patterns are summarized in figures 4.25 and 4.26 for spectroscopic site Y_1 and Y_2, respectively. While the agreement is not quite as accurate as the original g-tensor fit, a very good agreement has been obtained. It should be noted that, provided there is sufficient data to obtain a unique fit, this would allow the simulation of any set of

transitions within the entire $4f^{11}$ configuration.

Subsequently, the calculation was further refined by adding the ground-state EPR data reported by Guillot-Noël *et al.* [37]. In order to yield a convergent solution, it was necessary to include a number of separate Hamiltonians. More specifically, the spin Hamiltonian data was employed to generate ground-state splittings due to only the magnetic dipole hyperfine interaction and the nuclear quadrupole interactions, separately. These energy differences were then fit using separate Hamiltonians, in addition to a third Hamiltonian containing both the magnetic dipole as well as the nuclear quadrupole interactions. In addition to this, the exceptionally small magnitude of the hyperfine splittings compared to electronic and Zeeeman splittings made these fits highly sensitive to the respective weightings between the χ^2 contributions of each of these Hamiltonians. While it was originally hoped that the previously obtained crystal-field parameters would be a sound starting point for a subsequent bounded search, this assumption did not hold. Instead, it was necessary to repeat a complete global basinhopping search. The solution obtained by this method was further "polished" by repeating the final local minimization using the NLopt `sbplx` algorithm.

The complete set of calculated parameters are summarized in table 4.2. Additionally, the calculated energy levels up to the $^2H_{11/2}$ multiplet, along with their experimental counterparts reported by Doualan *et al.* , are summarized in table 4.1. As can be seen from the table, a very good agreement was achieved for the overall energy level predictions.

Table 4.1: Theoretical energy levels up to the $^2H_{11/2}$ multiplet of Er^{3+}:Y_2SiO_5 calculated using the here determined crystal-field Hamiltonian. For comparison, the experimentally determined values of energy levels reported in reference [117] have been included. All quoted values are in cm^{-1}. Question marks denote uncertain assignments as indicated by the authors of reference [117].

Multiplet	State	Site Y_1			Site Y_2		
		Theory	Exp.	Diff.	Theory	Exp.	Diff.
$^4I_{15/2}$	Z_1	4	0	-4.6	5	0	-5.2
	Z_2	37	42	5.0	22	28	6.2
							Continued over page.

Table 4.1: Theoretical energy levels up to the $^2H_{11/2}$ multiplet of Er^{3+}:Y$_2$SiO$_5$ calculated using the here determined crystal-field Hamiltonian. For comparison, the experimentally determined values of energy levels reported in reference [117] have been included. All quoted values are in cm^{-1}. Question marks denote uncertain assignments as indicated by the authors of reference [117].

Multiplet	State	Site Y$_1$			Site Y$_2$		
		Theory	Exp.	Diff.	Theory	Exp.	Diff.
	Z_3	88	86	-2.0	68	63	-5.0
	Z_4	109	104	-4.6	133	128	-4.6
	Z_5	180	172	-8.3	177	169	-7.9
	Z_6	411	424?	13.1	306	314	7.5
	Z_7	470	481	10.6	347	350	2.6
	Z_8	507	513	6.5	412	415	3.2
$^6I_{13/2}$	Y_1	6514	6507	-7.1	6507	6497	-9.9
	Y_2	6563	6547	-15.6	6547	6563	16.5
	Y_3	6605	6596.5	-8.2	6586	6592	6.3
	Y_4	6632	6623	-9.1	6614	6621	6.6
	Y_5	6792	6798	6.0	6709	6725	15.8
	Y_6	6851	6852	1.2	6748	6750	2.3
	Y_7	6874	6871	-3.3	6799	6798	-0.5
$^6I_{11/2}$	A_1	10178	10193	14.8	10173	10179	6.1
	A_2	10227	10271?	44.0	10205	10193?	-11.8
	A_3	10259	10292?	33.3	10226	10235.5	9.1
	A_4	10338	10308?	-30.1	10276	10250	-25.7
	A_5	10378	10369	-9.2	10304	10308?	3.8
	A_6	10391	10383?	-7.5	10343	10341	-2.1
$^6I_{9/2}$	B_1	12348	12359.5	11.5	12364	12376	12.4
	B_2	12452	12459.5?	7.5	12446	12448	2.4
	B_3	12528	12527.5?	-0.2	12490	12492?	2.2
	B_4	12616	12612	-3.8	12560	12563	3.2
	B_5	12669	12649.5	-19.3	12611	12605	-5.8
$^6H_{9/2}$	D_1	15179	15169	-9.7	15195	15195.5	0.1
	D_2	15220	15220.5	0.5	15228	15220.5	-7.3

Continued over page.

Table 4.1: Theoretical energy levels up to the $^2H_{11/2}$ multiplet of Er^{3+}:Y_2SiO_5 calculated using the here determined crystal-field Hamiltonian. For comparison, the experimentally determined values of energy levels reported in reference [117] have been included. All quoted values are in cm^{-1}. Question marks denote uncertain assignments as indicated by the authors of reference [117].

Multiplet	State	Site Y_1			Site Y_2		
		Theory	Exp.	Diff.	Theory	Exp.	Diff.
	D_3	15352	15360.5?	8.9	15306	15303	-2.9
	D_4	15387	15381.5	-5.7	15384	15381.5?	-2.6
	D_5	15487	15498	10.9	15435	15424.5	-10.1
$^6S_{3/2}$	E_1	18258	18267	8.7	18297	18308	11.0
	E_2	18371	18372	1.3	18406	18417	11.1
	E_3	19096	19091	-4.6	19088	19070	-18.1
$^2H_{11/2}$	F_1	19125	19116	-9.3	19132	19132	-0.5
	F_2	19164	-	-	19159	19159?	0.5
	F_3	19219	-	-	19203	19201	-1.6
	F_4	19256	-	-	19241	19244?	3.3
	F_5	19271	-	-	19254	19266	12.0

Finally, table 4.3 shows the theoretical hyperfine splittings for both the $^4I_{15/2}Z_1$ and $^4I_{13/2}Y_2$ states of Er^{3+}:Y_2SiO_5. We note that for some levels there is considerable disagreement. While it was possible to obtain an almost perfect fit to the ground state EPR data, this resulted in non-trivial deviations for the rotation patterns shown in figures 4.25 and 4.26. For example, in the case of site 1, a heavy weighting towards the ground-state hyperfine data resulted in an additional level crossing at 105° both in the $D_1 - D_2$ rotation plane as well as in the $D_2 - b$ rotation plane. All other transitions continued to closely match the *g*-tensor model of Sun *et al*. This mismatch in the ground-state hyperfine structure is attributed to the difficulty associated with achieving an accurate alignment of the crystallographic axes when performing EPR spectroscopy [136]. The crystal-field parameters presented here represent the closest match to the EPR data that was achieved while preserving a good agreement with the Zeeman rotation patterns.

Table 4.2: Fitted values for free-ion and crystal-field parameters of the C_1 symmetry Y_1 and Y_2 sites of Er^{3+}:Y_2SiO_5. All values are in cm^{-1}, and square brackets indicate that the parameter was held fixed during the optimization procedure.

Parameter	Site 1	Site 2
F^2	95346	95721
F^4	68525	68564
F^6	52804	52999
α	[17.79]	[17.79]
β	[-582.1]	[-582.1]
γ	[1800]	[1800]
T^2	[400]	[400]
T^3	[43]	[43]
T^4	[73]	[73]
T^6	[-271]	[-271]
T^7	[308]	[308]
T^8	[299]	[299]
M^{tot}	[3.86]	[3.86]
P^{tot}	[594]	[594]
ζ	2358	2356
B_0^2	-563	354
B_1^2	558+280i	498.6807+274i
B_2^2	143-121i	-75.8028+60i
B_0^4	-125	226
B_1^4	225-831i	-657.8381+593i
B_2^4	-48-945i	335.7827+253i
B_3^4	-615-688i	-71.3262-46i
B_4^4	744-102i	-813.9654+64i
B_0^6	-28	219
B_1^6	49+199i	-127+197i
B_2^6	120-107i	-36-47i
B_3^6	195-55i	17-108i
B_4^6	-287-161i	-100+77i
B_5^6	-117+162i	-263+103i
B_6^6	136+186i	12-26i
a_l	0.0059	0.0069
a_Q	0.0800	0.0808

Finally, we note that in order to employ this data to identify transitions in hole-burning or Raman-heterodyne data one would have to calculate transition intensi-

Table 4.3: Hyperfine splittings for the ground and first-excited states of Er^{3+}:Y_2SiO_5 simulated for both C_1 symmetry crystallographic sites. These values were generated using the crystal-field parameters determined by fitting to ground-state EPR data [37], ground and excited-state optical Zeeman data [39], as well as electronic state transition energies [117]. All values are in MHz.

Site 1		Site 2	
$^4I_{15/2}Z_1$	$^4I_{13/2}Y_1$	$^4I_{15/2}Z_1$	$^4I_{13/2}Y_1$
0.00	0.00	0.00	0.00
0.00	0.00	0.05	0.00
815.54	1133.64	792.24	1323.61
815.90	1133.65	795.87	1323.61
1568.59	2209.86	1500.11	2586.17
1594.52	2211.60	1581.75	2587.30
2108.10	3163.30	2015.24	3690.39
2603.59	3308.50	2717.64	3906.33
2868.15	4171.17	2936.75	4931.86
3608.39	4241.53	3709.52	4970.90
4018.43	5116.66	4122.41	6037.99
4036.12	5117.51	4161.76	6038.23
4664.90	5971.94	4823.32	7067.35
4664.99	5971.94	4824.47	7067.35
5305.86	6771.42	5527.24	8038.17
5305.86	6771.42	5527.26	8038.17

ties. While this is readily possible given the crystal field parameters in table 4.2, presenting the large number of allowed transitions graphically is difficult. This is due to the fact that both the ground-state as well as the excited-state wavefunctions are not pure in nuclear spin projection I_z, such virtually all transitions between each ground and each excited state are allowed.
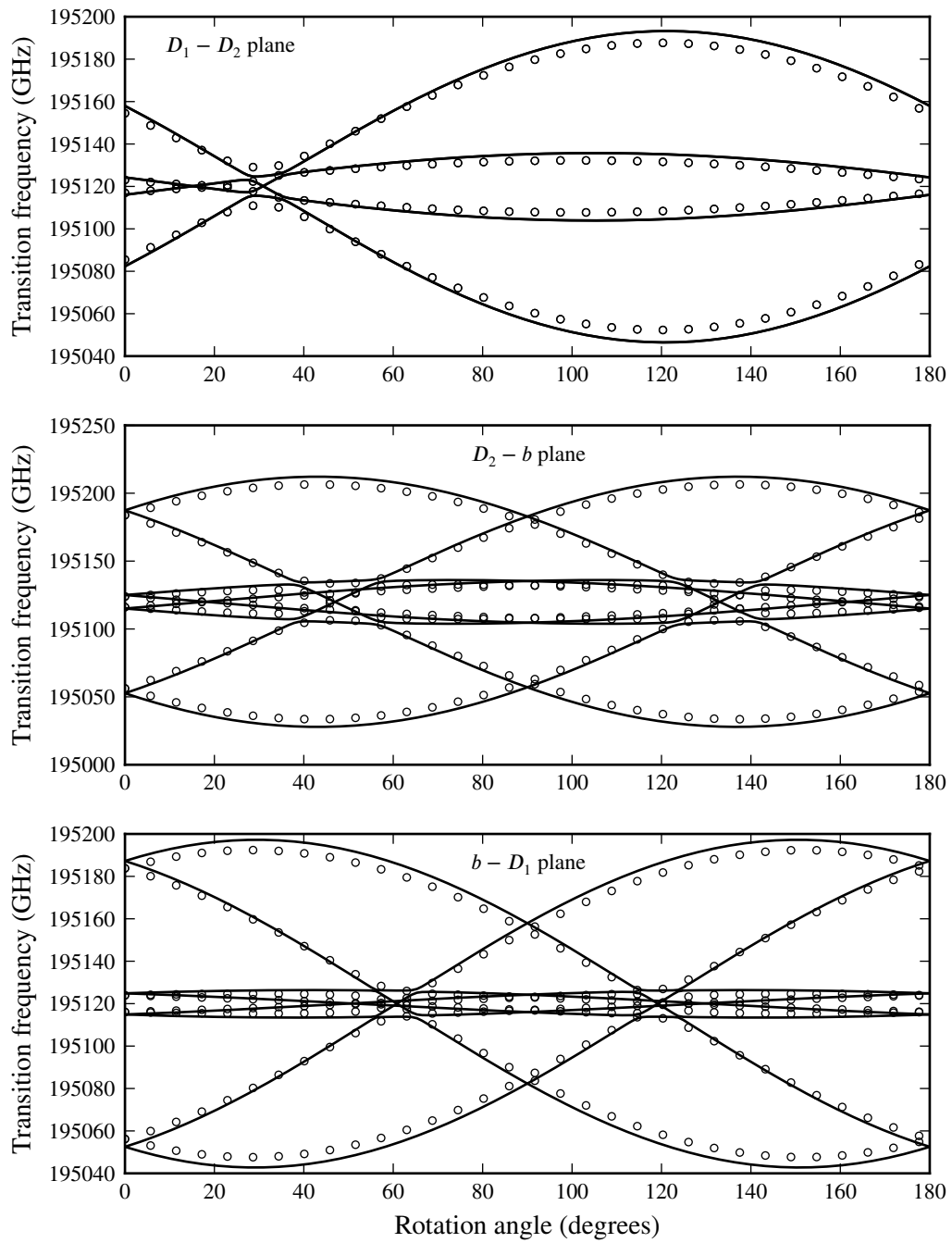
Figure 4.25: Rotation pattern for crystallographic site Y_1 of Er^{3+}:Y_2SiO_5. Energies are for the $^4I_{15/2}Z_1 \rightarrow {}^4I_{13/2}Z_2$ transition. Circles correspond to transition energies simulated using the ground and excited-state *g*-tensors due to Sun *et al.* [39], whereas solid lines are the transition energies simulated from the crystal-field Hamiltonian.
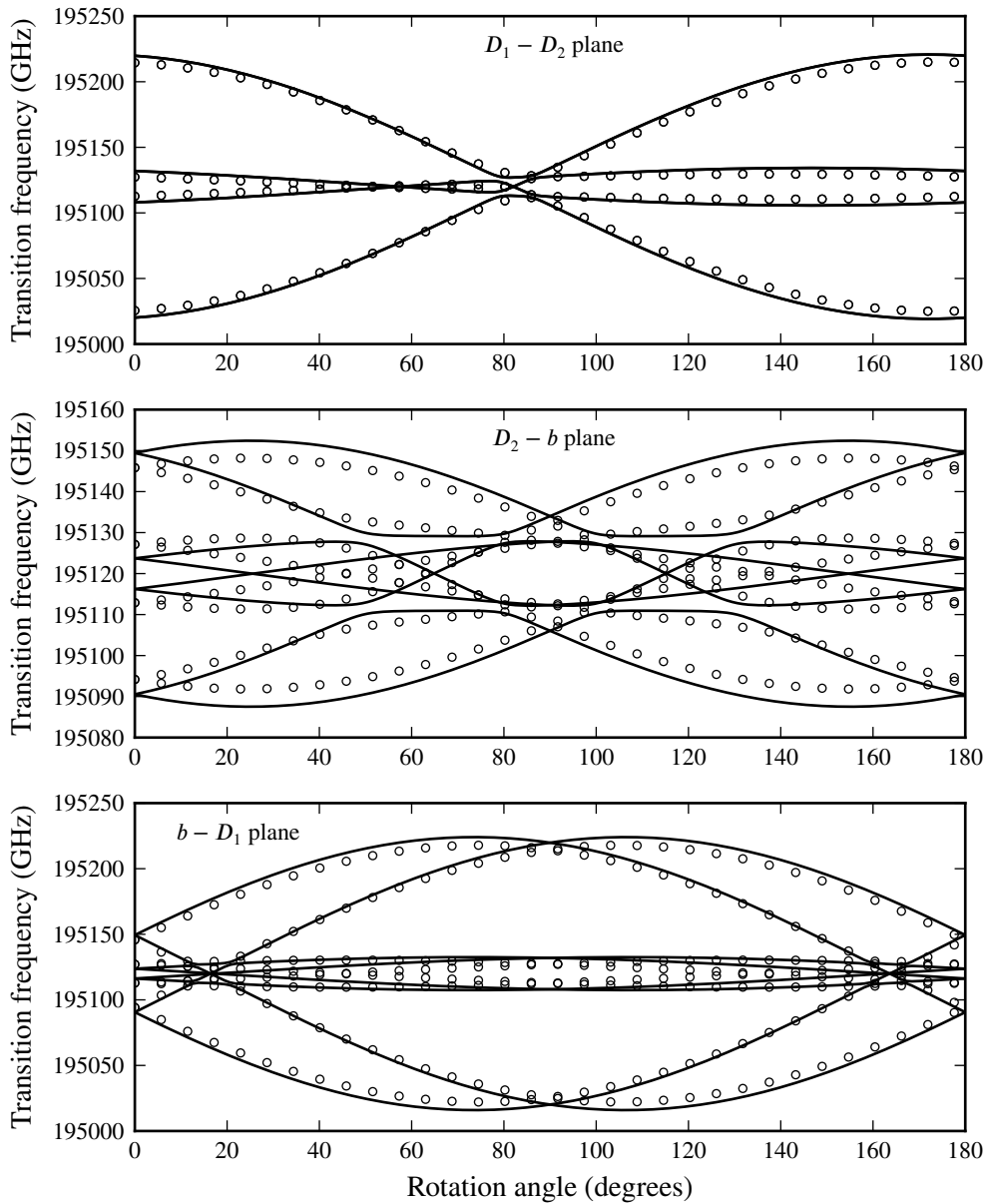
Figure 4.26: Rotation pattern for crystallographic site Y_2 of Er^{3+}:Y_2SiO_5. Energies are for the $^4I_{15/2}Z_1 \rightarrow {}^4I_{13/2}Z_2$ transition. Circles correspond to transition energies simulated using the ground and excited-state *g*-tensors due to Sun *et al.* [39], whereas solid lines are the transition energies simulated from the crystal-field Hamiltonian.

4.7 Conclusion

This chapter can effectively be divided into two separate components: the first consists primarily of experimental work, whereas the second component deals with the crystal-field analysis. The experimental work encompassed both the development and application of several high-resolution spectroscopic techniques. Specifically, the developed setup allows for single-frequency laser transmission experiments and spectral hole-burning spectroscopy to be performed in an external magnetic field of up to 7 Tesla, and with temperature control between 1.5 K to room temperature.

The first application that the developed experiment was applied to was a magnetic g-factor measurement of the $^4F_{9/2}D_1$ state in Er^{3+}:Y_2SiO_5. These measurements were performed using laser transmission spectroscopy, and yielded the magnetic splittings for the $^4I_{15/2}Z_1 \rightarrow {}^4F_{9/2}D_1$ transition. By making use of the published ground-state g-tensor it was possible to infer the excited-state g-values along the crystallographic b axis of 11.28 and 1.05 for spectroscopic sites Y_1 and Y_2, respectively.

Additional experiments performed for the $^4I_{15/2}Z_1 \rightarrow {}^4F_{9/2}D_1$ transition focused primarily on spectral hole-burning spectroscopy. This revealed that the dominant hole-burning mechanism is electron storage in the long-lived $^4I_{13/2}$ excited state. Hole lifetimes for sites 1 and 2 were determined to be 9.2 ± 0.5 ms and 7.2 ± 0.3 ms. In both instances, this is ~ 2 ms shorter than the published lifetime of the storage level. This shortening of the hole lifetime was attributed to spectral diffusion, which had been previously observed in erbium-doped insulators [131].

While excited-state storage was the dominant hole-burning mechanism, ground-state hyperfine storage was also observed, specifically at zero field. To our knowledge all previously reported instances of ground-state storage for erbium were performed in the presence of an external magnetic field in order to minimize hole filling due to spin flips of the valance electron in neighboring Er^{3+} ions. Additionally, a limited field dependent study revealed that the electron transfer efficiency to hyperfine levels was severely reduced in the presence of an external magnetic field. While a more comprehensive study of this effect is necessary in order to definitively establish the mechanism responsible for this reduction in hyperfine storage, it is conjectured that mixing of nuclear spin states results in unfavourable

selection rules for decay to different ground-state hyperfine levels.

The theoretical component of this chapter was solely focused on the application of the computational methods developed in chapter 3 to perform a crystal-field analysis for the C_1 symmetry sites of Er^{3+}:Y_2SiO_5. The only previously reported crystal-field analysis for a C_1 symmetry material was performed for Ce^{3+}:Y_2SiO_5 by Wen *et al*. [137]. However, rather than a fit directly to phenomenological data as was done here, Wen *et al*. conducted an ab initio calculation and then inferred the corresponding crystal-field parameters from the resulting solution.

The crystal-field parameters determined here accurately reproduce Zeeman splittings for arbitrary magnetic field orientations as well as energies of electronic states up to the $^2H_{11/2}$ multiplet. While the ground-state hyperfine structure is partially reproducible, the uncertainty associated with available EPR data made this analysis difficult. Future work including additional ground-state hyperfine data would overcome this issue.

5

Hyperfine structure on the $^5I_8 \rightarrow {}^5F_5$ transitions of Ho^{3+}:KY$_3$F$_{10}$

In this chapter a high-resolution excitation experiment applied to Ho^{3+}:KY$_3$F$_{10}$ in order to resolve the hyperfine splittings of states of the $^5F_5$ term as well as a detailed crystal-field analysis reproducing experimentally observed hyperfine transition intensities.

5.1 Introduction

The experimental methods and theoretical tools discussed in chapter 4 are, for the vast majority of RE^{3+} doped insulating crystals, the only method whereby one can infer the excited-state hyperfine splittings of the dopant ion. For a rare subset of materials it is, however, possible to directly resolve hyperfine splittings using high-resolution optical methods. This is most prominently the case for holmium, due to its large nuclear magnetic moment [138–141]. Such systems provide an excellent application for the theoretical tools more commonly relied on to infer the hyperfine splittings from more indirect measurements.

In this chapter, we perform high-resolution excitation spectroscopy in order to directly measure the hyperfine splitting of the $^5I_8Z_1 \rightarrow {}^5F_5D_3$ transition for holmium doped into a KY$_3$F$_{10}$ host. This, in conjunction with an analytical analysis of the ground-state pseudo-quadrupole moment, allows for the excited-state hyperfine splitting to be inferred. Using this result, along with published data for this material [142], a crystal-field analysis is performed to determine the hyperfine

coupling constant and the nuclear quadrupole coupling constant. While this work was in its initial phase, Pytalev *et al.* [141] reported the use of Fourier transform infrared absorption spectroscopy to resolve hyperfine splittings for absorption from the ground state to both the $^5I_7$ and $^5I_6$ multiplets of Ho^{3+}:KY_3F_{10}.

5.2 Experimental details

Trivalent holmium has a $4f^{10}$ configuration resulting in a total of 1001 electronic states. The only observationally stable isotope of holmium is ^{165}Ho, which has a nuclear spin of $I = 7/2$ [115] and a nuclear magnetic moment of 4.17 μ_N. When doped into KY_3F_{10}, the holmium ion substitutes for a Y^{3+} ion at a C_{4v} point-group symmetry site.

Single crystals of KY_3F_{10} doped with trivalent holmium at concentrations of 0.1 molar % and 0.02 molar % were grown using the Bridgman-Stockbarger technique, at the University of Strathclyde, Glasgow, United Kingdom. The reagents were stoichiometrically mixed and grown in graphite crucibles. In order to minimize evaporative losses, the growth chamber was filled with a positive pressure of highly purified argon gas in order to minimize evaporative losses. Crystals were oriented by cleaving along the crystallographic [111] plane [143] and polished using a 6 μm diamond-impregnated lap.

The high-resolution excitation experiment was performed using the experimental layout schematically shown in figure 5.1. A Toptica DL100 Pro, external grating stabilized diode laser was used to perform the excitation scan. Fluorescence was dispersed using a Newport Cornerstone 260 monochromator, and detected with a thermo-electrically cooled Hamamatsu R2257P photo-multiplier tube in conjunction with a Hamamatsu C9744 pre-amp/discriminator and a Hamamatsu C8855-01 photon-counting unit. Since fluorescence was monitored for the $^5F_5 \rightarrow$ $^5I_8Z_{13}$ transition, which is only separated from the excitation laser by $\sim$ 10 nm, laser scatter was a critical issue in spite of the Cornerstone 260. To alleviate this, an optical chopper was employed which alternately blocked the pump laser and the detection optics, with the C9744 triggered appropriately. While critically reliant on the excited-state lifetime, this method effectively eliminated laser scatter.

All timing aside from triggering of the C9744 photon counting unit was enforced by a computer program which was additionally responsible for stepping
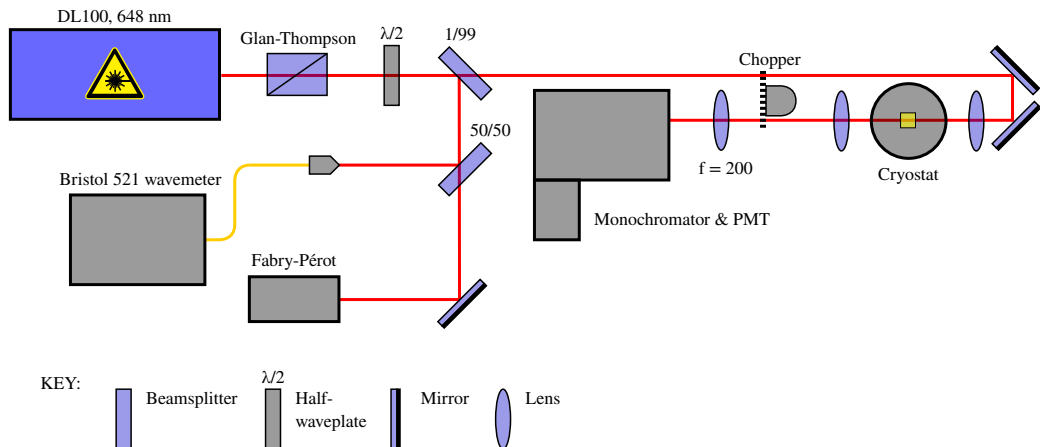
Figure 5.1: High resolution excitation experimental setup. The optical chopper is equipped with a 5 slot blade which alternately blocks the excitation pulse and the detection optics. This effectively eliminates noise due to laser scatter.

the laser wavelength. Furthermore, at each laser step, the exact DL100 wavelength was recorded using a Bristol 521 wavemeter. While the absolute accuracy of the wavemeter was limited to 10 ppm, by assuming a consistent laser step-size and least-squares fitting to the series of wavelength measurements, the accuracy could effectively be improved a factor of $\sqrt{N}$ where N is the number of steps.

Since the DL100 is limited to a maximum mode-hop free tuning range of 20 GHz, while the inhomogeneous linewidths of transitions $^4I_8 \rightarrow {}^4F_5$ of Ho^{3+}:KY_3F_{10} are of the order of several wavenumbers, it was necessary to perform excitation scans in segments. This was done by coarse tuning the DL100 to the center of a scan segment, and then optimizing the drive current to achieve the required mode-hop free scan range. To verify mode-hop free scanning was achieved, the laser frequency was monitored using a Coherent 33-6305-001 Fabry-Pérot interferometer.

Experiments were performed at zero field using a temperature of 10 K. Crystals were clamped using a copper sample mount and cooled using a Janis CCS-150 closed-cycle cryostat regulated by a Lakeshore 325 temperature controller.

5.3 Results and discussion

In order to directly observe the hyperfine splittings of Ho^{3+}:KY$_3$F$_{10}$, measurements were performed for samples of both 0.1 % and 0.02 % Ho^{3+} at 10 K. The short-wavelength coarse tuning limit of the DL100 excitation source was 646.1 nm, which restricted this study to the $^5I_8Z_1 \rightarrow {}^5F_5D_3$, the $^5I_8Z_1 \rightarrow {}^5F_5D_2$, and the $^5I_8Z_2 \rightarrow {}^5F_5D_1$ transitions. For the 0.1 % sample, no hyperfine structure was visible, and it was only possible to record the inhomogeneous lineshape. By moving to a lower concentration sample, the dopant-induced strain on the crystal structure was sufficiently reduced such that hyperfine structure was resolvable for the excitation to the D$_3\gamma_5$ doublet. The recorded fluorescence for the transition $^5F_5D_3 \rightarrow {}^5I_8Z_{13}$ is shown in figure 5.2.
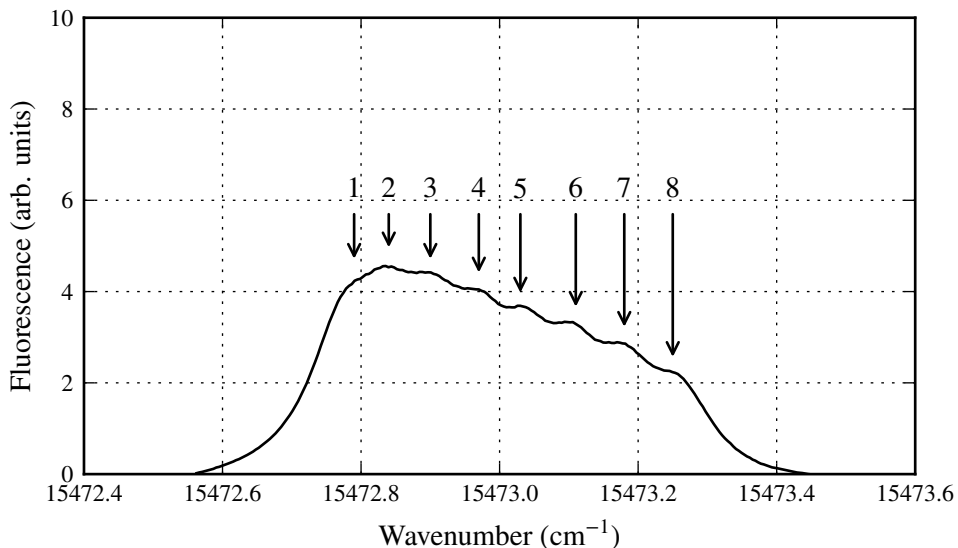
Figure 5.2: Partially resolved hyperfine excitation spectrum for 0.02 % Ho^{3+}:KY$_3$F$_{10}$, at 10 K. The excitation laser was scanned over the inhomogeneous lineshape of the $^5I_8Z_1 \rightarrow {}^5F_5D_3$ transition while fluorescence was monitored for the $^5F_5D_3 \rightarrow {}^5I_8Z_{13}$ relaxation back to the ground state. Arrows indicate transition labels used to tabulate observed splittings; see table 5.1.

Similar scans were performed for the $^5F_5$ D$_1\gamma_2$ and D$_2\gamma_1$ states but no hyperfine splittings were observed. This is attributed to γ_1 and γ_2 irreducible representations

corresponding to singlet states, such that the hyperfine interaction is dominated by the second-order pseudo-quadrupole moment. More specifically, at a C_{4v} point-group symmetry substitutional site, the dopant ground-state transforms as a singlet γ_1 irreducible representation [142]. As a consequence, the expectation value of the total angular momentum operator J_z vanishes for the ground state, which, to first order, leads to a zero Zeeman shift and no hyperfine splitting. However, due to to the nearby $Z_2\gamma_2$ singlet separated by 5.8 cm^{-1}, a second order effect referred to as pseudo-quadrupole splitting can occur, albeit at a significantly smaller magnitude than the observed splitting due to the $Z_3\gamma_5$ doublet.

These recorded excitation spectra are shown in figure 5.3. As is evident from the figure, while the hyperfine transitions are within the inhomogeneous envelope, the lineshape is clearly not Gaussian as a consequence of the underlying hyperfine splittings. In order to obtain better-resolved spectra, one would have to further lower the dopant concentration of the samples in the hope to additionally reduce the inhomogeneous lineshape. However, since the samples were grown at the University of Strathclyde in 1998, this was option was not available.

In order to deduce the excited-state hyperfine splitting it is necessary to analytically determine the ground-state splitting due to the pseudo-quadrupole hyperfine interaction. This can be done using results from second order perturbation theory. For an axial symmetry host, the magnetic dipole hyperfine Hamiltonian for a specific multiplet can be written in the form [74]:

$$H_{\mathrm{HF}} = A_{\parallel} J_z I_z + A_{\perp}(J_x I_x + J_y I_y),\tag{5.1}$$

with $A_{\parallel}$ and $A_{\perp}$ constituting the parallel and perpendicular components of the hyperfine interaction, respectively. Thus, the problem amounts to determining the matrix elements of H_{HF} and thereafter evaluating the eigenvalues. We begin with the ground-state wavefunctions. For a C_{4v} point-group symmetry substitutional site, the first two levels of the ground state transform under the irreducible representations γ_1 and γ_2, respectively, which have the general form

$$|\gamma_1\rangle = \alpha_1\left(|^5I_8, 8\rangle + |^5I_8, -8\rangle\right) + \alpha_2\left(|^5I_8, 4\rangle + |^5I_8, -4\rangle\right) + \alpha_3|^5I_8, 0\rangle$$
$$|\gamma_2\rangle = \beta_1\left(|^5I_8, 8\rangle - |^5I_8, -8\rangle\right) + \beta_2\left(|^5I_8, 4\rangle - |^5I_8, -4\rangle\right).\tag{5.2}$$
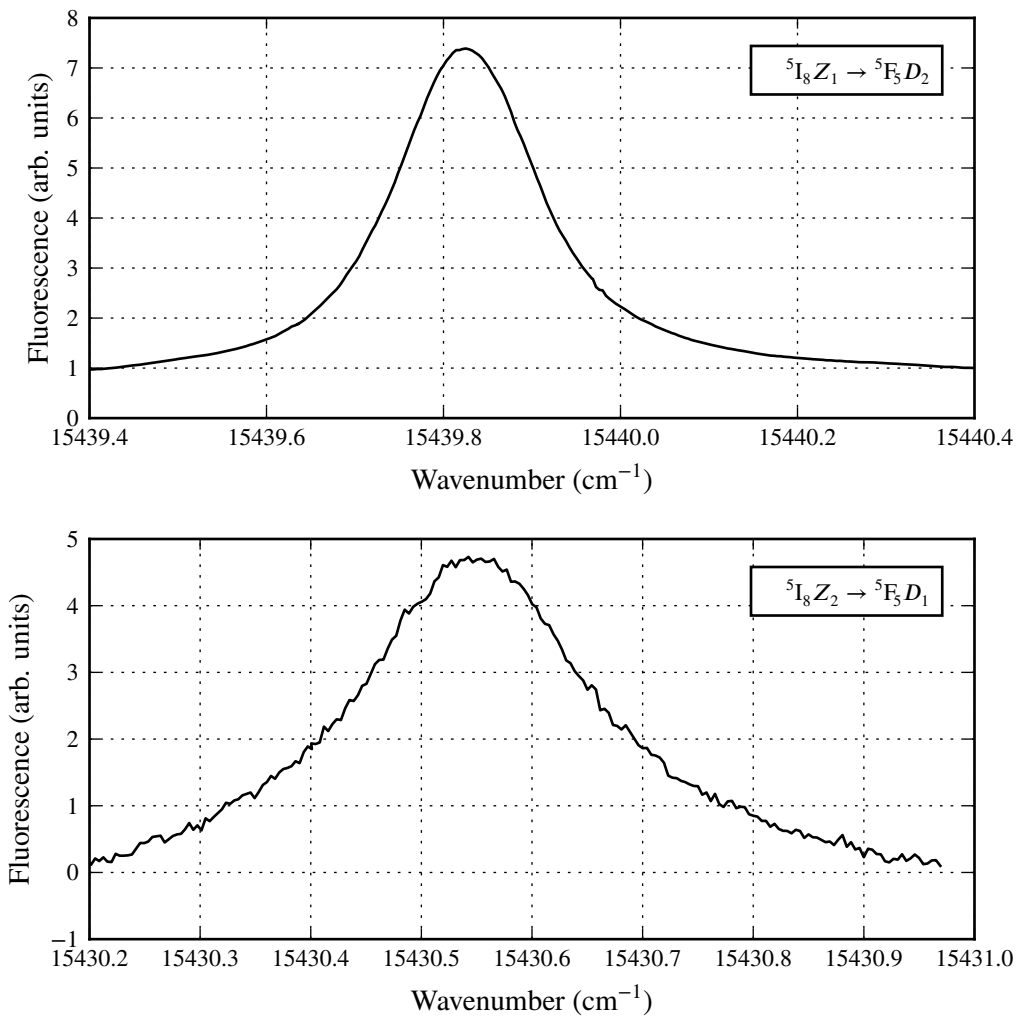
Figure 5.3: Excitation spectra for $Ho^{3+}{:}KY_3F_{10}$, at 10 K. The upper panel corresponds to excitation of the $^5I_8Z_1 \rightarrow {}^5F_5D_2$ transition and the bottom panel corresponds to excitation of the $^5I_8Z_2 \rightarrow {}^5F_5D_1$ transition. Fluorescence was monitored back to the $^5I_8Z_{13}$ state.

In order to determine the α and β coefficients, we perform a crystal-field calculation excluding the hyperfine interaction. We note that the crystal-field Hamiltonian appropriate for a C_{4v} point-group symmetry site has the form [65]:

$$H_{CF} = B_0^2 C_0^{(2)} + B_0^4 C_0^{(4)} + B_0^6 C_0^{(6)} + B_4^4 \left(C_4^{(4)} + C_{-4}^{(4)} \right) + B_4^6 \left(C_4^{(6)} + C_{-4}^{(6)} \right). \quad (5.3)$$

Taking the free-ion and crystal-field parameters published by Mujaji and Wells [142], one obtains for $Z_1\gamma_1$: $\alpha_1 = -0.0172$, $\alpha_2 = -0.6995$, and $\alpha_3 = -0.1427$. Similarly, for the $Z_2\gamma_2$ one finds: $\beta_1 = 0.0177$ and $\beta_2 = 0.7067$. To evaluate the matrix elements of (5.1), we note that it is clear by inspecting the wavefunctions (5.2) that all matrix elements of the perpendicular component necessarily vanish. This leaves the expectation value of J_z, which evaluates to

$$\langle \gamma_1 | J_z | \gamma_2 \rangle = -3.9547. \tag{5.4}$$

Thus, the matrix elements take the form

$$H_{\text{HF}} = \begin{pmatrix} -\Delta & A_{\parallel} I_z \langle J_z \rangle \\ A_{\parallel} I_z \langle J_z \rangle & \Delta \end{pmatrix}, \tag{5.5}$$

where H_{HF} is understood to be in the Heisenberg representation. Solving the resulting characteristic polynomial yields the following expression for the eigenvalues of H_{HF}

$$E(I_z) = \pm \sqrt{\Delta^2 + (A_{\parallel} \langle J_z \rangle J_z)^2}. \tag{5.6}$$

Evaluating the above equation with a magnetic hyperfine constant for the $^5I_8$ term of 812 MHz [74], one obtains the splittings indicated in figure 5.4.

Having determined the ground-state splittings due to the pseudo-quadrupole moment, the excited-state hyperfine splitting was inferred from the spectrum shown in figure 5.2. Both the estimated experimental hyperfine splittings as well as the corresponding theoretical values are summarized in table 5.1. We observe here

Table 5.1: Experimental and calculated hyperfine splittings for the $^5I_8Z_1 \rightarrow {}^5F_5D_3$ transition of Ho^{3+}:KY_3F_{10} at 10 K. Line splittings correspond to the difference between transitions due to states of the same nuclear spin, from highest to smallest. See figure 5.5 for explicit labels. All energies are reported in cm^{-1}, with an uncertainty of ± 0.005 cm^{-1}.

Line	I_z	Hyperfine calc.	Exp. splittings
1-8	$\pm 7/2$	0.499	0.440
2-7	$\pm 5/2$	0.357	0.341
3-6	$\pm 3/2$	0.214	0.205
4-5	$\pm 1/2$	0.071	0.063

$| \pm \frac{7}{2} \rangle$ ————————— 174.73 GHz

$| \pm \frac{5}{2} \rangle$ ————————— 174.85 GHz

$| \pm \frac{3}{2} \rangle$ ————————— 175.09 GHz

$Z_2\gamma_2$ ——————————

$| \pm \frac{1}{2} \rangle$ ————————— 175.45 GHz

173.88 GHz

$Z_1\gamma_1$ ——————————

$| \pm \frac{1}{2} \rangle$ ———————— 0.71 GHz

$| \pm \frac{3}{2} \rangle$ ———————— 0.59 GHz

$| \pm \frac{5}{2} \rangle$ ———————— 0.35 GHz

$| \pm \frac{7}{2} \rangle$ ———————— 0.00 GHz
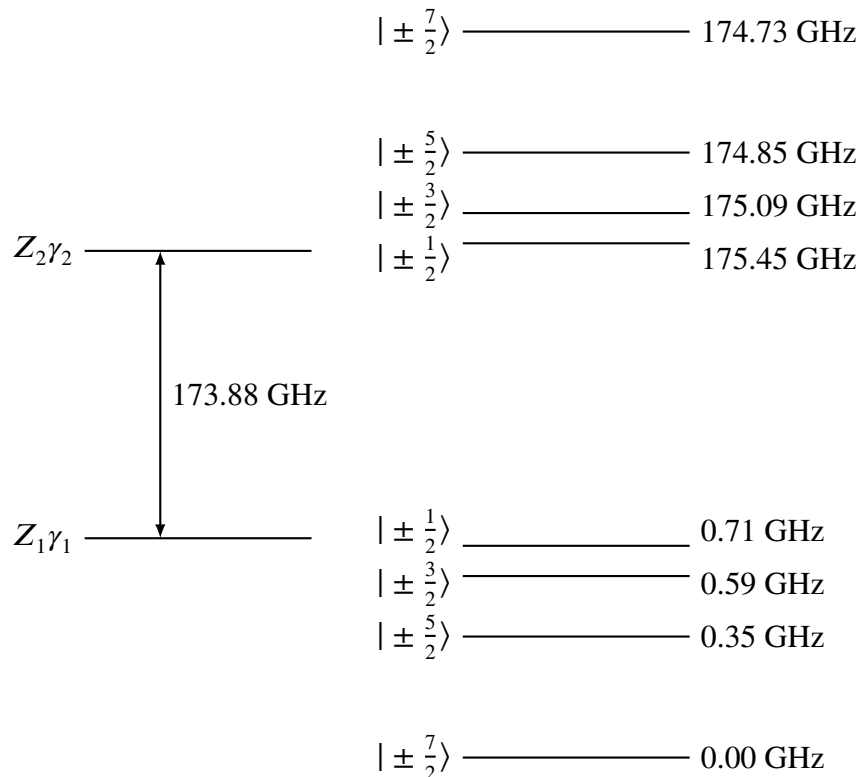
Figure 5.4: Theoretical splitting of the $Z_1\gamma_1$ and $Z_2\gamma_2$ levels of the ground-state $^5I_8$ multiplet in Ho^{3+}:KY$_3$F$_{10}$ due to the pseudo-quadrupole interaction.

that there is a very good agreement between the theoretical splitting and the corresponding experimental value for lines 2-7, 3-6, and 4-5, with all deviations less than 0.02 cm^{-1}; however, the 1-8 splitting deviates by almost three times as much.

This data was used to perform a crystal-field fit that included the nuclear magnetic dipole as well as the nuclear quadrupole interaction. The calculated free-ion, crystal-field, and hyperfine parameters are summarized in table 5.2. They have been listed alongside published crystal-field parameters for a calculation excluding hyperfine data [142]. As can be seen, the changes to the crystal-field parameters are minimal for the fit that includes hyperfine data. We note here, that the total higher-order spin dependent effect parameters M^{tot} and P^{tot} have the following

definitions:

$$M^{\text{tot}} = M^0 + 0.56 M^2 + 0.31 M^4$$
$$P^{\text{tot}} = P^2 + 0.5 P^4 + 0.1 P^6. \tag{5.7}$$

Table 5.2: Free-ion, C_{4v} crystal-field and hyperfine parameters for $Ho^{3+}:KY_3F_{10}$. Parameters in square brackets were held constant during the fit. For comparison, the crystal-field parameters determined by Mujaji and Wells [142], which did not include a fit to hyperfine splittings, are also shown.

Parameter	Fitted value (cm^{-1})	Reference [142] (cm^{-1})
F^2	94062	94063
F^4	66355	66361
F^6	51667	51637
α	[17.15]	17.15
β	[-607.9]	-607.9
γ	[1800]	1800
T^2	[400]	400
T^3	[37]	37
T^4	[105]	105
T^6	[-264]	-264
T^7	[316]	316
T^8	[336]	336
M^{tot}	[2.54]	2.54
P^{tot}	[605]	605
ζ	2141	2142
B_0^2	-669	-669
B_0^4	-1270	-1269
B_4^4	344	344
B_0^6	525	525
B_4^6	-2	9
a_l	0.038	-
a_Q	0.060	-

In order to perform the actual crystal-field fit, the energy level data published by Mujaji and Wells [142] was utilized and optimized to fit with a Hamiltonian that did not include hyperfine matrix elements. The hyperfine splittings were specified

separately as energy level differences within the ground and the excited state. This ensured that any shift of the $^5F_5$ barycenter did not completely dominate the minimization problem, since the hyperfine splittings are comparatively tiny. By using the `INTEN` program, the crystal-field parameters determined using `pycf` could be employed to generate transition intensities for both magnetic-dipole and forced electric-dipole transitions. The theoretical linewidth of individual hyperfine transitions was adjusted to 0.1 cm^{-1} to match the observed experimental spectrum, and a Boltzman factor corresponding to 10 K was used to estimate the ground-state population. The resulting theoretical lineshape is shown in blue in figure 5.5 alongside the previously shown experimental spectrum. We note that the large
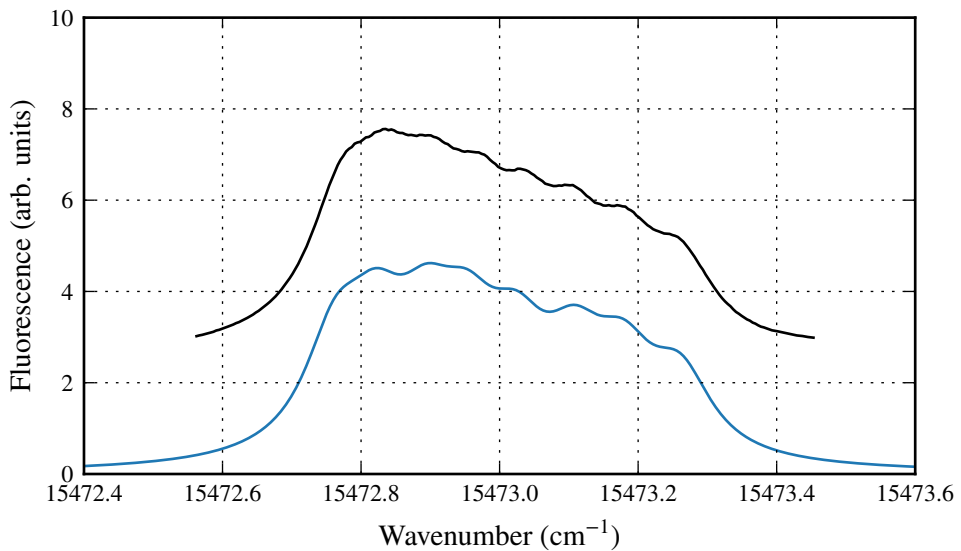
Figure 5.5: Top: resolved hyperfine excitation spectrum for 0.02 % Ho^{3+}:KY$_3$F$_{10}$, at 10 K. Bottom: the corresponding simulated spectrum showing both transition intensities due to both magnetic and electric dipole moments. The linewidth of individual hyperfine transitions was set to 0.1 cm^{-1}, whereas a temperature of 10 K was used to estimate the ground-state population levels. The simulated spectrum has been shifted by 8.8 cm^{-1} to account for a barycenter shift of the $^5F_5$ term.

dips observed in the simulated spectrum are likely due to the 0.06 cm^{-1} wavenumber disagreement between for the 1-8 splitting indicated in table 5.1.

While the reconfiguration of the optical laboratory prevented a detailed mea-

surement of the observed hyperfine splittings under the influence of an external magnetic field, it has been determined from our theoretical model that one expects to observe highly non-trivial interactions due to the Zeeman effect in the presence of the ground-state pseudo-quadruple splitting. Figure 5.6 shows simulated spectra up to 2 Tesla of the $^5I_8Z_1 \rightarrow {}^5F_5D_3$ transition. The observed splitting is due to the parallel Zeeman component which is non-zero since for a γ_5 irreducible representation J_z has a non-vanishing expectation value. It is difficult to assign a g-factor to this splitting due to the non-linearity which can be observed for the low-energy component of the splitting. This non-linearity is due to an avoided crossing with the lower-energy component of the γ_5 doublet. The disappearance
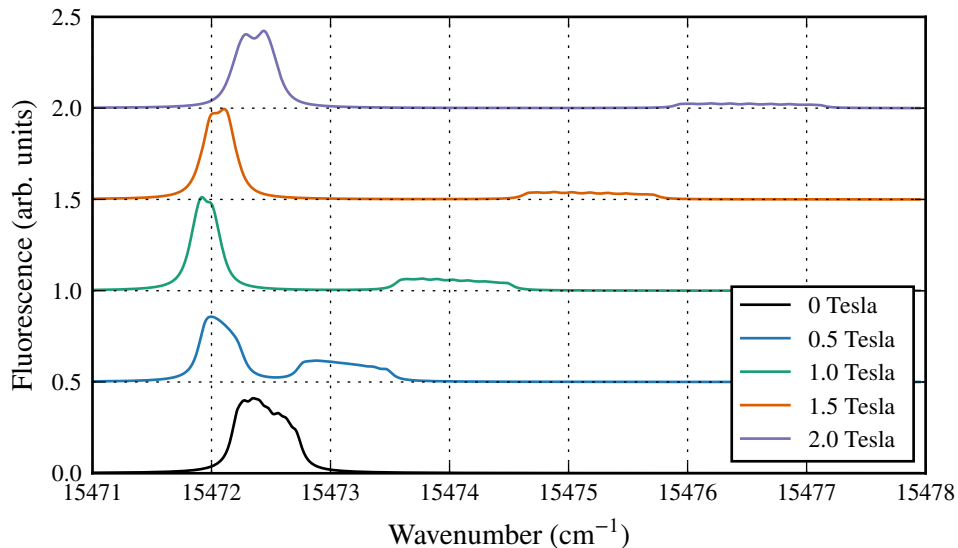
Figure 5.6: Simulated magnetic field dependence of the $^5I_8Z_1 \rightarrow {}^5F_5D_3$ transition of $Ho^{3+}:KY_3F_{10}$, at 4.2 K. Indicated field strengths are for a magnetic field parallel to the crystallographic [111] direction.

of resolvable hyperfine splittings at 0.5 Tesla in spite of a fixed linewidth can be attributed to the mixing of nuclear spin states in the $^5I_8$ multiplet. Below we show the largest components of the ground state at an external field of 1.0 Tesla along

the crystallographic [111] direction:

$$\left| Z_1 \right\rangle = (-0.5365 - 0.5365i) \left| {}^5I_8, -4, \tfrac{7}{2} \right\rangle - (0.2818 + 0.2818i) \left| {}^5I_8, 4, \tfrac{7}{2} \right\rangle$$
$$- 0.4011i \left| {}^5I_8, -4, \tfrac{5}{2} \right\rangle - 0.2188i \left| {}^5I_8, 4, \tfrac{5}{2} \right\rangle + \cdots \tag{5.8}$$

Even though the principal components of the ground state are still nuclear-spin projections $I_z = \pm 7/2$, the mixing of other nuclear spin projections is sufficient to prevent the resolution of individual hyperfine transitions. While a preliminary experimental investigation has indeed observed that there is a highly complex field dependence of this nature for the $^5I_8 Z_1 \rightarrow {}^5F_5 D_3$ transition, the to-date obtained results are not sufficiently conclusive to warrant inclusion.

5.4 Conclusion

High-resolution laser excitation spectroscopy was employed to study the optical hyperfine transitions of Ho^{3+}:KY_3F_{10}. For the available crystal doped at 0.02 molar % holmium, individual hyperfine transitions were partially resolved for the $^5I_8 Z_1 \rightarrow {}^5F_5 D_3$ transition . The observed spectra could be accurately modeled using a crystal-field Hamiltonian which included both the nuclear magnetic dipole moment as well as the nuclear quadrupole moment interactions. Additionally, a theoretical investigation employing the obtained parameters revealed a complex interaction between the nuclear spin selection rules in the presence of an external magnetic field. This provides an interesting avenue for further investigation.

6

An infrared pump-probe measurement of the $^6\mathrm{H}_{7/2}$ lifetime of Sm^{3+}:LiYF$_4$

We report a measurement of the $^6\mathrm{H}_{7/2}$ manifold lifetime in Sm^{3+}:LiYF$_4$ using pump-probe sectroscopy. Since ultra-fast techniques are rarely applied to rare-earth ions, this represents one of the few direct lifetime measurements performed for the first excited state of this class of material. A lifetime of 3.1 ps was inferred for the Y_2 level of the $^6\mathrm{H}_{7/2}$ manifold, which is substantially faster than that predicted by the commonly used exponential energy-gap law. This implies either that a non-linear energy-gap law is required, as has been suggested in the literature, or perhaps it is indicative of an inherent non-exponential component in ultra-fast non-radiative processes of rare-earth doped LiYF$_4$.

6.1 Introduction

Rare-earth doped LiYF$_4$ has been widely employed in solid-state optical devices and has been the subject of a wide variety of investigations. Yet the dynamics of low-lying energy levels of rare-earth dopants in LiYF$_4$ remain relatively unexplored to date. The dynamical properties of low-lying energy levels are of particular interest in laser systems, since the low-lying energy levels often serve as the terminal level of laser transitions.

The effective phonon energy of the LiYF$_4$ dielectric host is 560 cm^{-1} [104]; consequently, for lanthanide dopants the relaxation rate from such terminal levels is dominated by non-radiative processes. Specifically, given a total relaxation rate

W_{tot}, we can make the approximation $W_{\text{tot}} = W_{\text{r}} + W_{\text{nr}} \approx W_{\text{nr}}$, where W_{r} and W_{nr} are the radiative and non-radiative decay rates, respectively. A widely employed tool to predict such non-radiative decay rates is the exponential energy-gap law [144], which has the following functional form

$$W_{\text{nr}} = C \exp[-\alpha \Delta E]. \tag{6.1}$$

Here C and α are phenomenological parameters that are characteristic of the dielectric host material, and ΔE is the energy-gap of the transition. C is the so-called electronic factor, and strongly depends on the crystalline host. The parameter α has a dependence on the order of the phonon process and on the phonon occupation number at the selected temperature. In addition, α depends on the Huang-Rhys factor. However, as has been shown by van Dijk and Schuurmans [145], the Huang-Rhys factor generally varies by less than a factor of two for different ions and transitions; consequently, the assumption of α being primarily host dependent is justified.

A number of theoretically motivated modifications to equation (6.1) have also been proposed in the literature. These have the general form of

$$W_{\text{nr}} = C \exp[-\alpha(\Delta E - \epsilon)], \tag{6.2}$$

where ϵ is taken to range between $1.5\hbar\omega$ and $3.0\hbar\omega$, where $\hbar\omega$ the energy of the phonon mode [145–148]. These formulations have the advantage that they largely uncouple the dependence of electronic factor C from the dielectric host, and thus reduce the variation of C across different hosts to within an order of magnitude. In the original formulation of equation (6.1), for contrast, C varies by up to a factor of 10^5 across different host materials.

We here report a pump-probe measurement of the $^6H_{7/2} \rightarrow {}^6H_{5/2}$ transition in Sm^{3+}:LiYF$_4$, for which $\Delta E = 1075$ cm^{-1} [103]. This yielded a lifetime of 3.1 ps for the Y_2 level of the $^6H_{7/2}$ manifold. As such, it is among the fastest experimentally measured decay rates in a rare-earth doped insulating crystal and constitutes a direct measurement of a previously unexplored parameter space for the non-radiative decay rates of this important laser host material. Furthermore, the lifetimes substantially deviate from the exponential energy-gap law.

This result was found to be consistent with pump-probe measurements of H$^-$ modes in LiYF$_4$, in which Z vibrational modes with $\Delta E = 1122.4$ cm^{-1} were observed to have a lifetime of 2.7 ps [149]. It should be noted, however, that a direct comparison of this lifetime in the context of the energy-gap law is not valid due to the dependence of α on the Huang-Rhys factor.

6.2 Experimental details

The samples were bulk LiYF$_4$ crystals doped at 5 molar percent SmF$_3$. They were grown using the vertical Bridgman-Stockbarger technique in a positive argon gas atmosphere.

Infrared absorption measurements were performed with a Bio-Rad FTS-40 FTIR spectrometer at a maximum resolution of 0.1 cm^{-1}. The samples were cooled using a CTI-Cryogenics model 22C closed-cycle liquid-helium cryostat.

The pump-probe experiments were performed with the Dutch free-electron laser FELIX at Radboud University, Nijmegen, The Netherlands. Figure 6.1 consists of a schematic showing the key components of a free-electron laser.
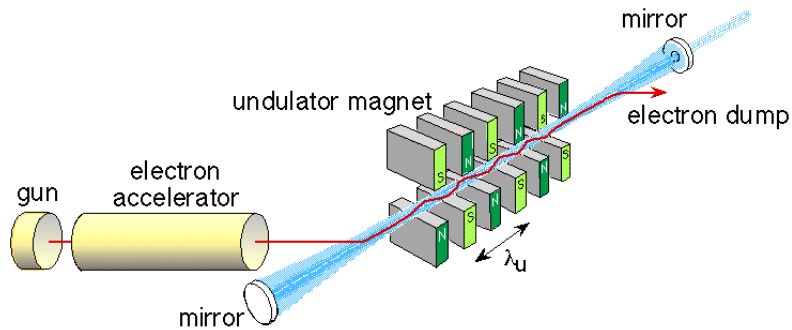
Figure 6.1: A schematic representation of a free-electron laser. Electrons are injected from the electron-gun into a series of steering magnets referred to as the undulator. The acceleration experienced by the electrons causes them to undergo synchrotron radiation, which is amplified on successive round trips between the end mirrors forming a cavity.

The optical pulse structure of FELIX inherits its defining properties from the RF pulse structure applied to the electron-gun. Since FELIX uses an RF linac accelerator, the pulse train consists of macropulses of length 8 μs each of which is in turn composed of a set of micropulses of length $\sim$ 1 ps. Figure 6.2 graphically

shows the relationship of the macropulse structure and the micropulse structure. The repetition rate of the macropulses was configured to 10 Hz, and the micropulse separation was 40 ns. Macropulse shot-to-shot power fluctuations were alleviated by the use of a three-pulse pump, probe, and reference detection scheme [150].
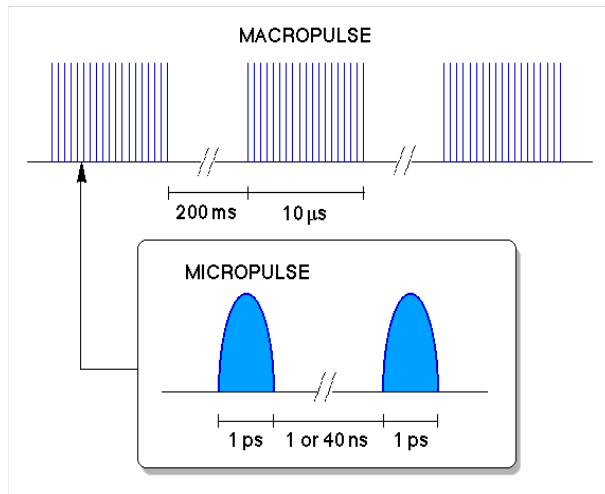
Figure 6.2: The optical pulse train of an RF linac free-electron laser.

The optical setup is shown schematically in figure 6.3. The FELIX pulse sequence was initially passed through a BaF$_2$ beam-splitter that selected 95% of the beam in order to form the pump pulse. The remaining 5% was then passed through a 50:50 beamsplitter to form the probe and reference pulses. The reference pulse is delayed from the probe pulse by 20 ns using a -1 telescope, but otherwise follows an identical beam-path. The transmission through the sample of the probe beam was then measured with respect to the delay time.

In order to minimize losses due to optical elements, uncoated gold mirrors were used throughout the experiment. All three pulses are overlapped and focused onto the sample using an $f = 15$ cm 90° off-axis diamond-turned parabolic mirror. Beam-overlap was verified using a 200 μm pinhole. By employing a Newport UTM150CC linear translation stage, the pump pulse time with respect to the probe and reference could be adjusted by up to 1 ns. The samples were cooled with an Oxford Instruments liquid helium flow "Microstat" in conjunction with an ITC503 controller. Both the probe and reference beams were then focused onto a liquid nitrogen cooled mercury cadmium telluride detector. The readout electronics con-
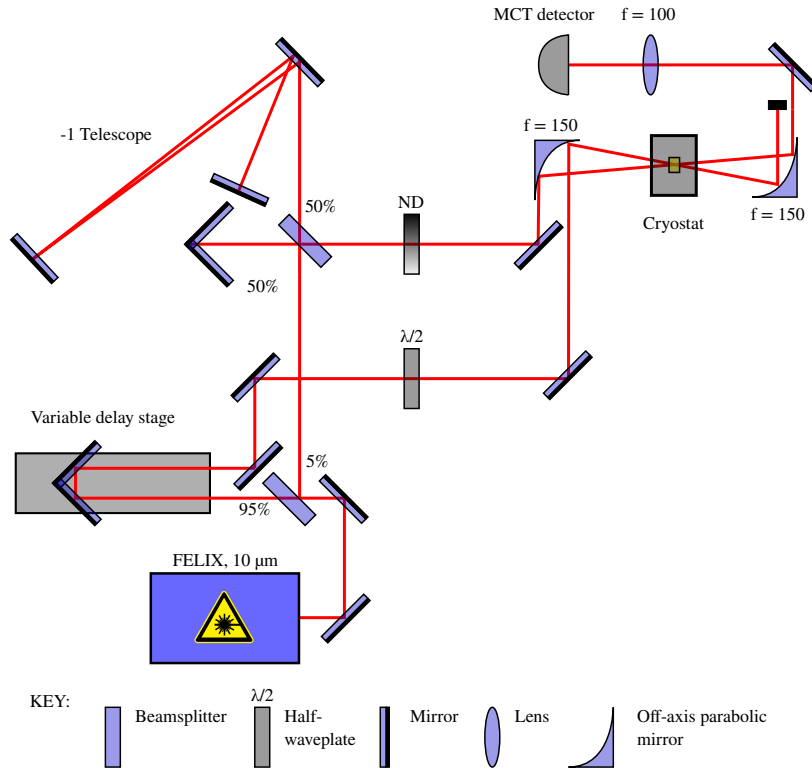
Figure 6.3: Optical arrangement used for performing infrared pico-second pump probe spectroscopy. See the text for a detailed description of key components.

sisted of a balanced detection system, an SRS boxcar averager synchronized with the FELIX macropulse trigger, and a National Instruments analog-to-digital card. The variable delay stage position that corresponded to "time-zero", that is, the time delay when the pump and probe pulses are incident on the sample simultaneously, could be identified by an interference pattern which was the result of scatter off the sample surface.

The balanced detection electronics allowed for a compensation of the macropulse power fluctuations. In brief, the detector is bias modulated at 25 MHz in sync with the FELIX micropulses, yielding signals with an opposite sign for the probe and the reference beams. By blocking the pump beam it was possible to ensure that the probe and reference pulses experienced the same attenuation due to the sample, and thus allowed one to tune the electronic bias to achieve a balanced signal strength for the probe and reference pulses.

Consequently, the integrated signal recorded by the boxcar is the difference in attenuation experience by the probe and the reference pulses, effectively cancelling the shot-to-shot macropulse power fluctuations of a few percent.

6.3 Results and discussion

Figure 6.4 shows an FTIR absorption scan of the 1 μm to 1.1 μm region which contains both the $Z_1\gamma_6 \rightarrow Y_1\gamma_6$ and $Z_1\gamma_6 \rightarrow Y_2\gamma_7$ transitions.
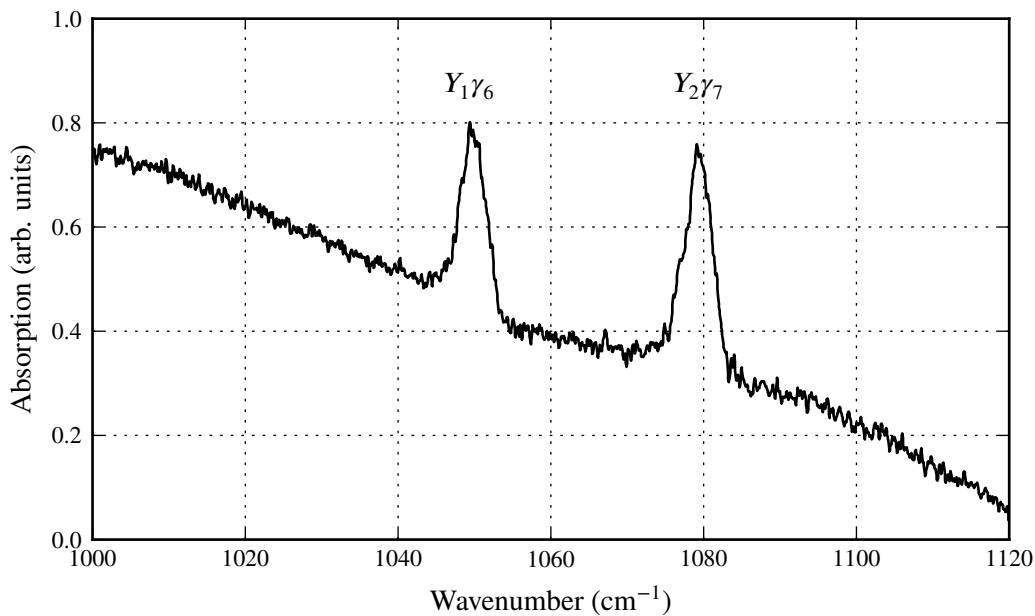
Figure 6.4: 10 K absorption spectrum of the $^6H_{7/2}$ multiplet in Sm^{3+}:$LiYF_4$. The transitions correspond to absorption from the ground-state $Z_1\gamma_6$ to the states $Y_1\gamma_6$ and $Y_2\gamma_7$, respectively. The background shoulder is due to multi-phonon absorption of the host crystal lattice.

After subtracting the multi-phonon edge background visible in figure 6.4, a Lorentzian lineshape was fit to the absorption peaks from which an absorbance of 2.5 was inferred, corresponding to an oscillator strength of $P = 9.91 \times 10^{-8}$. For comparison, using theoretical methods the oscillator strength was estimated to be of the order of $P = 8.44 \times 10^{-7}$. In order to perform this calculation, it was necessary to determine the wavefunctions of the ground and excited state for

Sm^{3+}:LiYF$_4$. The RE^{3+} substitutes at a site of D_{2d} symmetry, which can be described using a crystal-field Hamiltonian of the following form:

$$H_{CF} = B_0^2 C_0^{(2)} + B_0^4 C_0^{(4)} + B_0^6 C_0^{(6)} + B_4^4 C_4^{(4)} + B_4^6 C_4^{(6)}. \qquad (6.3)$$

The necessary free-ion and crystal-field parameters were sourced from references [67] and [151], respectively. Having diagonalized the resulting Hamiltonian, it was possible to evaluate the matrix elements of the magnetic dipole operator defined by equation (2.46) by an application of the VTRANS and INTEN programs. Having determined the magnetic dipole moment, the oscillator strength could then be calculated directly using equation (2.51).

The pump-probe experiment was performed with excitation of the $Y_2\gamma_7 \rightarrow Z_1\gamma_6$ transition in Sm^{3+}:LiYF$_4$. Figure 6.5 shows the probe transmission with respect to the delay between the pump and the probe pulse at a temperature of 5 K. In order to determine the life-time of the $^6H_{7/2}$ levels, we fit a two level rate-equation model of the following form:

$$\frac{dN_0(t)}{dt} = -\frac{\sigma_0}{\hbar\omega}I(t)N_0(t) + \frac{\sigma_0}{\hbar\omega}I(t)N_1(t) + \frac{N_1(t)}{\tau_{10}}$$

$$\frac{dN_1(t)}{dt} = \frac{\sigma_0}{\hbar\omega}I(t)N_0(t) - \frac{\sigma_0}{\hbar\omega}I(t)N_1(t) - \frac{N_1(t)}{\tau_{10}}$$

$$N = N_0(t) + N_1(t). \qquad (6.4)$$

This is a valid assumption, since the decay from the Y_2 to Y_1 excited state would be small given the phonon-distribution of LiYF$_4$ [152, 153] and the small energy difference. In equation (6.4), τ_{10} corresponds to the lifetime of the transition between the ground state and the Y_2 level. Furthermore, $N_0(t)$ and $N_1(t)$, are the population levels of the Z_1 and Y_2 levels, respectively, while N is the total electron population number, determined from the Sm^{3+} doping level. σ_0 is the cross-section for the $Z_1 \rightarrow Y_2$ transition and was inferred from our theoretically calculated oscillator strength. Finally, $I(t)$ corresponds to the FELIX pulse shape which is well approximated by $I(t) = I_0\text{sech}^2(t/0.38\tau_\omega)$, where I_0 is the peak intensity, and $\tau_\omega = 3.7$ ps the full-width at half maximum.

Solving the system of rate equations (6.4) then allows us to relate the lifetimes to the change in ground-state transmission experienced by the probe pulse. For a
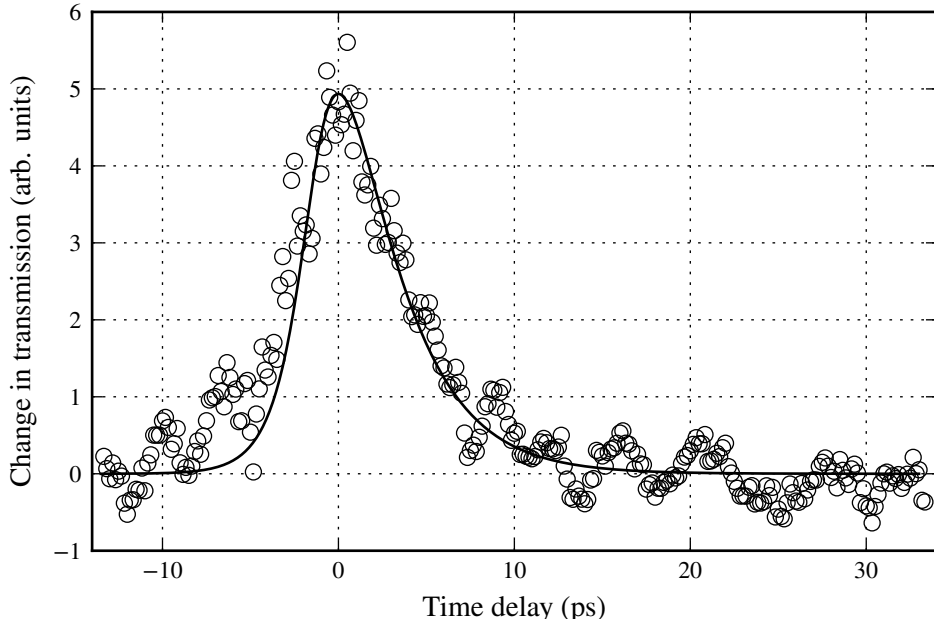
Figure 6.5: The pump-probe measurement of the $Y_2\gamma_7 \rightarrow Z_1\gamma_6$ transition in Sm^{3+}:LiYF$_4$ (circles). The solid line corresponds to the fitted rate equations (6.4). The resulting lifetime for the $Y_2\gamma_7$ level was calculated to be 3.1 ps.

given time delay, t, the probe transmission is given by

$$S(t) = -\frac{\sigma_0}{\hbar\omega} I(t) N_0(t) + \frac{\sigma_0}{\hbar\omega} I(t) N_1(t). \qquad (6.5)$$

By performing a least-squares fit of equation (6.5) with respect to the experimental data, the lifetimes of the Y_2 level was established to be $\tau_{10} = 3.1$ ps. The resulting model of the theoretical change in probe transmission is shown in figure 6.5 as a solid line. The peak change in transmittivity observed was of the order of

$$\frac{\Delta T}{T} = 10^{-3}. \qquad (6.6)$$

Figure 6.6 is a semi-log plot showing the approximate exponential relationship between the energy-gap and non-radiative decay rate for a variety of transitions of lanthanide-doped LiYF$_4$ crystals. It should be noted that all data points have been corrected to $T = 0$ K by dividing out the temperature dependent factor. As is
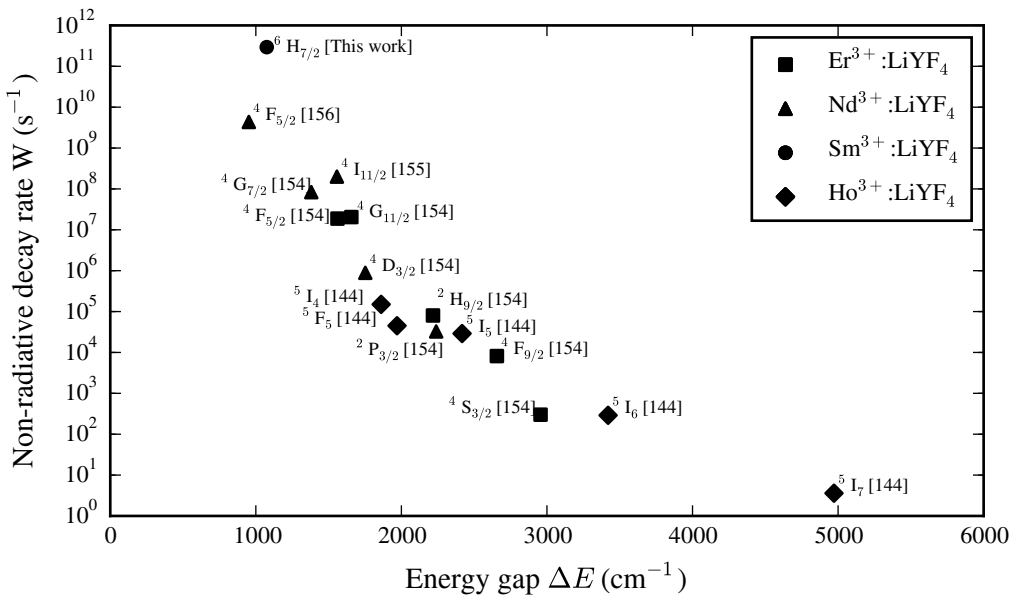
Figure 6.6: Plot of experimental non-radiative decay rates of various transitions of lanthanide doped $LiYF_4$. The data is sourced from references [144, 154–156] with specific references indicated by the square brackets after the manifold label.

evident from the figure, our measurement deviates from the empirical energy-gap law. This deviation can perhaps be explained by the non-linear model of non-radiative decay proposed by Orlovskii *et al.* [154, 157], which predicts that the energy-gap law does not consist of a single exponential for all ΔE. However, a previous measurement of $^4F_{5/2}$ relaxation rate in Nd^{3+}:$LiYF_4$ has observed a substantially lower relaxation rate for a comparable energy [156]. Thus, it is not clear from our additional data point whether the deviation can correctly be accounted for by such a non-linear model. Furthermore, given the effective phonon energy of $LiYF_4$ is of the order of $560\ cm^{-1}$ [104], we are clearly in a two phonon regime; for such processes, non-exponential behaviour with respect the energy-gap law is not without precedent. Studies in silicate and fluoroberylate glasses [152, 153] and $NdCl_3$ [158] have observed significant deviation from the energy-gap law.

6.4 Conclusion

We have presented a direct measurement of the $^6H_{7/2}$ manifold lifetime in samarium doped LiYF$_4$. The observed lifetime of 3.1 ps for the Y_2 level substantially deviate from the expectation of the energy-gap law that is commonly employed to model non-radiative decay rates in insulating crystals. Given that the measurement is effectively independent of the dopant species, this is of significance for estimating the lifetime in any two-phonon non-radiative process of rare-earth doped LiYF$_4$.

7

Conclusion

The principal aim of this thesis was to assist the search for an accurate theoretical model of the $^4\mathrm{I}_{13/2}Y_1$ state of $\mathrm{Er}^{3+}{:}\mathrm{Y}_2\mathrm{SiO}_5$ accounting for both the hyperfine structure as well as Zeeman splittings in an arbitrary magnetic field. Such a model would enable the search for ZEFOZ transitions for $\mathrm{Er}^{3+}{:}\mathrm{Y}_2\mathrm{SiO}_5$ in the 1.5 μm telecommunications wavelength region. Furthermore, there are several additional applications of $\mathrm{Er}^{3+}{:}\mathrm{Y}_2\mathrm{SiO}_5$, such as whispering-gallery mode resonators which are promising optical-microwave coupling systems with unity efficiency.

Towards this end we have successfully developed a crystal-field model which can partially reproduce the ground-state hyperfine structure as well as complex magnetic field dependent transition energies between the ground state and the $^4\mathrm{I}_{13/2}Y_1$ state. Furthermore, since it spans the entire $4f^N$ configuration, this model can be employed for predicting the hyperfine structure of any excited state. This will hopefully enable the interpretation of optical spectroscopy data for the $^4\mathrm{I}_{13/2}$ multiplet in order to achieve very accurate models of the excited-state hyperfine structure.

From a more technical standpoint this represents the first phenomenological crystal-field fit for a C_1 symmetry material. The only similar type of calculation reported previously was performed for $\mathrm{Ce}^{3+}{:}\mathrm{Y}_2\mathrm{SiO}_5$ by Wen *et al*. [137]. However, rather than fit to phenomenological data, the approach of Wen *et al*. instead employed an ab initio model to predict the expected crystal-field parameters.

As part of the effort to develop a crystal-field model for $\mathrm{Er}^{3+}{:}\mathrm{Y}_2\mathrm{SiO}_5$, a number of experiments were conducted for the ground state to the $^4\mathrm{F}_{9/2}D_1$ level transition. Specifically, spectral hole-burning spectroscopy was used to identify long-term

storage of electrons in hyperfine states at zero field. This result is surprising for a Kramers ion such as erbium, since spin flips of the unpaired electron in nearby Er^{3+} ions are understood to be the primary source for hole filling in similar materials [131]. While some preliminary field dependent measurements were performed, no definitive conclusion could be drawn to explain this surprising result.

The developed theoretical methods and experimental facilities also enabled several additional investigations. In particular, crystal-field analyses were done for an S_4 center in Ce^{3+}:LiYF4 and a C_{2v} center in Sm^{3+}:Na^+/Li^+:CaF_2/SrF_2. This yielded a good agreement between energy level data as well as EPR g-value data. In the case of Sm^{3+}:Na^+/Li^+:CaF_2/SrF_2 the calculation was additionally augmented using ground-state hyperfine data from EPR spectroscopy; however, due to the large uncertainty associated with the measured A-values, it was difficult to accurately reproduce the fit to this data simultaneously with the g-values.

The experimental development also enabled a high-resolution excitation experiment for Ho^{3+}:KY_3F_{10}. Partially resolved hyperfine splittings were directly observed in fluorescence for the $^5I_8Z_1 \rightarrow {}^5F_5D_3$ transition. The recorded values for the hyperfine splittings could be accurately reproduced using a theoretical crystal-field calculation.

Finally, a direct measurement of the $^6H_{7/2}$ excited-state lifetime of Sm^{3+}:$LiYF_4$ was completed using pico-second pump-probe spectroscopy, using a short-pulsed infrared free-electron laser. The relaxation rate from the $Y_2\gamma_7$ state to the ground state was experimentally measured to be 3.4 ps. This confirmed a previously-suggested two-gradient modification to the widely used energy-gap law. At 3.4 ps, this is one of the fastest directly measured lifetimes for any RE^{3+}-doped insulators reported in the literature, and as such is a valuable data point in order to confirm predictions at very short timescales.

A

Appendix I: pycf reference

A.1 `cfl` – python wrapper for cfl

class `cfl.StateLabels`

State label type for tensors and spin Hamiltonians. State labels are generally not entered manually but should be generated with `import_sljm.ImportSLJM`.

class `cfl.Tensor`

The Tensor class provides an interface for the creation of cfl zt objects. They are employed for the creation of both complete Hamiltonians and the projection of spin Hamiltonian interactions from complete Hamiltonians. Objects of type Tensor support standard arithmetic operations and can be added, subtracted, and scaled to yield new Tensor objects.

Tensors should typically not be created manually but imported from emp sljm output files using `import_sljm.ImportSLJM`.

Parameters

name : string

A string that uniquely identifies the tensor.

a : np.ndarray

A two dimensional array containing the matrix elements of the tensor.

Returns

t : Tensor

Methods

`get_name`(*self*)

> Get the name of this Tensor. If it has not been explicitly named (by instantiation or setting of the name attribute post creation by arithmetic), we set the Tensor's name to the name of the variable that this tensor is assigned to in the __main__ namespace. This is useful, since often new tensors are created by the scaling or addition of other Tensors, which, with out recourse to this hack, would require us to explicitly name such tensors after instantiation. If more than one variable points to the same Tensor object, get_name cannot guarantee a unique name and will raise a RuntimeError.

class `cfl.Hamiltonian`

> The crystal field Hamiltonian class. Creates a cfl zh object and provides an interface for diagonalizing zh. Can be used to calculate:
>
> > - energy levels given a list of :class:'Tensor's and corresponding coefficients;
> >
> > - spin Hamiltonian parameters from crystal field parameters;
> >
> > - crystal field parameters by fitting to either energy levels or both
> energy levels and spin Hamiltonian parameters.
>
> A summary of calculated energy levels can be generated with `cfl_util.gen_e_summary()`.
>
> Hamiltonians are iterable, returning the Tensor objects from which it is composed.
>
> > **Parameters**
> >
> > > **tensors** : list
> > >
> > > > A list with components of type Tensor; this specifies the type of interactions modeled by the Hamiltonian.
> > >
> > > **Returns**
> > >
> > > > **h** : Hamiltonian
>
> **Methods**

`diag`(*self*)

>   Diagonalize the Hamiltonian.

>   >   **Returns**

>   >   >   **(w, z)** : tuple

>   >   >   >   The eigenvalues and eigenvectors, respectively, of the diagonalized Hamiltonian.

`gen_summary`(*self,   ex=None,   nstates=2,   sigma=None, e_shift=False*)

Generate an energy level summary resulting from a diagonalization.

>   >   **Returns**

>   >   >   **ex** : np.ndarray, optional

>   >   >   >   A 2 by m array, specifying the experimental energy levels, with m the number of available experimental levels. The first column specifies the index of the corresponding entry in the complete eigenvalue vector, and the second column contains the energy level values.

>   >   >   **nstates** : int, optional

>   >   >   >   The number of constituent states to display for mixed states.

>   >   >   **sigma** : float, optional

>   >   >   >   The standard deviation for the energy level chi^2.

>   >   >   **e_shift** : bool, optional

>   >   >   >   Shift entire eigenvalue spectrum s.t. the first eigenvalue is zero.

`index`(*self, tensor*)

`set_coeff`(*self, coeff*)

>   Set the tensor coefficients.

>   >   **Parameters**

>   >   >   **coeff** : dict

>   >   >   >   Must contain an element for each tensor specified when the Hamiltonian object was instantiated. Keys have to be the same as tensor names.

class `cfl.SpinHamiltonian`

Abstraction for spin Hamiltonian data. Objects of type SpinHamiltonian are

used for calculating spin Hamiltonian parameters from crystal field parameters in conjunction with `Hamiltonian` objects.

The type of data that a SpinHamiltonian object represents depends on the specified interactions, but can be loosely thought of as the matrix elements of for all specified interactions; for Zeeman interactions, this will be three sets of matrix elements. Objects of this type are used by the function `esh_fit()` to fit crystal field parameters to spin Hamiltonian data.

> **Parameters**
>> **interactions** : list
>>> Elements are strings which specify the interactions of the spin Hamiltonian. Possible values are: 'zeeman', 'hyperfine', and 'quadrupole'.
>>
>> **level** : int
>>> The level of the complete Hamiltonian for which to project the spin Hamiltonian.
>>
>> **S** : float
>>> The spin projection S_z; if `interactions` contains 'zeeman' or 'hyperfine' this keyword argument must be specified.
>>
>> **I** : float
>>> The nuclear spin projection I_z; if `interactions` contains 'hyperfine' or 'quadrupole' this keyword argument must be specified.
>
> **Returns**
>> **object** : SpinHamiltonian

Methods

`calc_param`(*self*, *h*)

> Calculate the spin Hamiltonian parameters given a complete Hamiltonian.

>> **Parameters**
>>> **h** : Hamiltonian
>>>> The corresponding complete Hamiltonian.

Returns

param : list

Elements are nd.arrays corresponding to spin Hamiltonian tensors of interactions specified when the spin Hamiltonian object was instantiated.

`index`(*self*, *tensor*)

`set_pro_data`(*self*, *tensors*, *coupling_constants={}*)

Set the projection data for all spin Hamiltonian interactions.

Parameters

tensor : list

Elements must be of type Tensor. The list must contain Tensors for every interaction specified when the SpinHamiltonian was created. These must have the following name attributes: 'MAGX', 'MAGY', and 'MAGZ' for Zeeman interactions; 'HYP' for hyperfine interactions; 'EQHYP' for quadrupole interactions. Finally, even if the SpinHamiltonian does not describe Zeeman interactions the 'MAGZ' tensor must be provided for state-label sorting.

coupling_constants : dict, optional

If hyperfine or quadrupole interactions are present, this dictionary has to be provided, which specifies the nuclear dipole and nuclear quadrupole coupling constants, using keys 'HYP' and 'QUAD', respectively.

`cfl.zeeman_sh_coeff`(*v*, *t*)

Generate the Zeeman interaction spin Hamiltonian 'coefficient array'. This consists of a $2j + 1 \times 2j + 1$ by 3×3 array containing the matrix elements of the terms $B_a S_b$, with $a, b \in \{x, y, z\}$ and j the angular momentum of the rank one tensor S. Here the rows enumerate the $2j + 1 \times 2j + 1$ different state combinations while the columns enumerate all combinations of a and b.

Parameters

v : numpy.ndarray

A 3 by 1 vector of magnetic field strengths B_x, B_y and B_z.

t : list

Elements consist of the matrix elements of S_x, S_y and S_z.

Returns

result : numpy.ndarray

A $2j + 1 \times 2j + 1$ by 3×3 array.

cfl.**hyperfine_sh_coeff**(*t1*, *t2*)

Generate the hyperfine interaction spin Hamiltonian 'coefficient array'. This consists of a $(2j_1 + 1 \times 2j_2 + 1) \times (2j_1 + 1 \times 2j_2 + 1)$ by 3×3 array containing the matrix elements of the operators $I_a S_b$, with $a, b \in \{x, y, z\}$ and j_1 and j_2 the angular momentum of the rank one tensors I and S, respectively. Here the rows enumerate the $(2j_1 + 1 \times 2j_2 + 1) \times (2j_1 + 1 \times 2j_2 + 1)$ different state combinations while the columns enumerate all combinations of a and b.

Parameters

t1 : list

Elements consist of the matrix elements of I_x, I_y and I_z.

t2 : list

Elements consist of the matrix elements of S_x, S_y and S_z.

Returns

result : numpy.ndarray

A $(2j_1 + 1 \times 2j_2 + 1) \times (2j_1 + 1 \times 2j_2 + 1)$ by 3×3 array.

cfl.**quadrupole_sh_coeff**(*t*)

Generate the quadrupole interaction spin Hamiltonian 'coefficient array'. This consists of a $2j + 1 \times 2j + 1$ by 3×3 array containing the matrix elements of the operators $I_a I_b$, with $a, b \in \{x, y, z\}$ and j the angular momentum of the rank one tensor I. Here the rows enumerate the $2j + 1 \times 2j + 1$ different state combinations while the columns enumerate all combinations of a and b.

Parameters

t : list

Elements consist of the matrix elements of I_x, I_y and I_z.

Returns

result : numpy.ndarray

A $2j + 1 \times 2j + 1$ by 3×3 array.

class `cfl.ExData`

Experimental energy level data for Hamiltonians.

Parameters

data : np.ndarray or tuple

If data is of type np.ndarray it assumed to be a 2 by n dimensional, with the first column containing energy level indices starting at 1, and the second column containing the absolute experimental energy of the corresponding level. If data is of type tuple each element must be a np.ndarray of type specified using the key argument. Implemented types are:

- Absolute energy level data with level index (default).

- Difference energy level data with level index; np.ndarray must be 3 by n dimensions, where the first column specifies the initial energy level index, the second column specifies the final energy level index, and the third column corresponds to the energy difference.

- Absolute energy level data with state label index; of dimension m+1 by n, where m is the number of state labels. The first m elements are state labels in LS coupling with the type of label of each element specified by the labelkey argument. The (m+1)th entry contains the absolute experimental energy of the corresponding level.

- Difference energy level data with state label index; of dimension 2m+1 by n, where m is the number of state labels. The first m elements are state labels in LS coupling specifying the initial energy level. The next m elements are state labels in LS coupling specifying the final energy level. The final entry corresponds to the energy difference. The type of state label elements are given by labelkey.

Note: mixing level index data with state label index data is not supported.

key : str or tuple, optional

If data is of type np.ndarray this argument is optional; otherwise it must be specified and be of the same length as the data tuple. This argument is used to specify the type of data. Available keys are:

- 'A', absolute energy data with level index;

- 'D', difference energy data with level index;

- 'AS', absolute energy level data with state label index;

- 'DS', difference energy level data with state label index.

label_key : str, optional

This argument is only required if experimental data with state label indices is to be used. In this case, each element of label_key specifies the type of each of the m state label entries passed via the data argument. It must match the label_key of Hamiltonian to be fit to this experimental data.

class `cfl.EFitRunner`

Class used to store data required by, and to run, a crystal field fit using energy level data.

The Hamiltonian must have coefficients set with set_coeff, since these are used as initial estimates for the parameters to-be-fit. The type of each coefficient when they are set also determines whether that coefficient is fit as real or complex parameter.

Parameters

parameters : list

A list of tensor objects for which to vary the prefactor.

h : Hamiltonian

The Hamiltonian for which to fit the energy levels.

ex : np.ndarray or ExData

Either a 2 by n dimensional np.ndarray or an ExData type object. In the former case, n is the number of energy levels, with the first column containing energy level indices starting at 1, and the second column containing the absolute experimental energy of the corresponding level. In order to specify energy

level differences, or specify energies according to their SLJM
state labels, use the ExData interface.

ignore_ndof : bool, optional

Force minimization even if there are fewer observables than
parameters; use at your own peril.

Methods

`fit`(*self*, *min_object*)

Run the fit using the provided minimization object.

Parameters

min_object : CFLMin

The minimization object to be used, which sets the opti-
mization algorithm, bounds and other settings as applicable
to the selected algorithm.

Returns

result : tuple

The first element is a np.ndarray containing complex co-
efficients while the second entry contains the final value of
the objective function.

class `cfl.MHFitRunner`

Class used to store data required by, and to run, a crystal field fit using
multiple Hamiltonians. Typically, this would consist of one Hamiltonian
at zero field without hyperfine or quadrupole interactions, complemented
by a set of Hamiltonians at linearly independent magnetic field orientations
and possibly containing hyperfine interactions. The associated additional
eigenvalues can either be measured or synthetically calculated for specific
crystal field levels from spin Hamiltonian data.

The Hamiltonians must have coefficients set with set_coeff, since these are
used as initial estimates for the parameters to-be-fit. The type of each co-
efficient when they are set also determines whether that coefficient is fit as
real or complex parameter, thus they must be consistent among each Hamil-
tonian.

Parameters

parameters : list

A list of tensor objects for which to vary the prefactor.

h_list : list

A list of Hamiltonians, each containing the interactions required to match the corresponding experimental energy level data.

weights_list : list

A list of floating point weights that determine the weighting added to the chi^2 contribution of each eigenvalue vector.

ex : np.ndarray or ExData

Either a list of 2 by n dimensional np.ndarrays or a list of ExData type objects. In the former case, n is the number of energy levels, with the first column of each array containing energy level indices starting at 1, and the second column containing the absolute experimental energy of the corresponding level. In order to specify energy level differences, or specify energies according to their SLJM state labels, use the ExData interface.

ignore_ndof : bool, optional

Force minimization even if there are fewer observables than parameters; use at your own peril.

Methods

`fit`(*self*, *min_object*)

Run the fit using the provided minimization object.

Parameters

min_object : CFLMin

The minimization object to be used, which sets the optimization algorithm, bounds and other settings as applicable to the selected algorithm.

Returns

result : tuple

The first element is a np.ndarray containing complex co-
efficients while the second entry contains the final value of
the objective function.

class `cfl.ESHFitRunner`

Class used to store data required by, and to run, a crystal field fit using energy
level and spin Hamiltonian data.

The Hamiltonian must have coefficients set with set_coeff, since these are
used as initial estimates for the parameters to-be-fit. The type of each co-
efficient when they are set also determines whether that coefficient is fit as
real or complex parameter.

> **Parameters**
>
> > **parameters** : list
> >
> > > A list of tensor objects for which to vary the prefactor.
> >
> > **h** : Hamiltonian
> >
> > > The Hamiltonian for which to fit the energy levels.
> >
> > **sh** : SpinHamiltonian
> >
> > > The spin Hamiltonian object to be fit. Must have projection
> > > data set with the set_pro_data method. If it contains hyperfine
> > > or quadrupole interactions, the respective coupling constants
> > > will automatically be added to the parameters.
> >
> > **ex** : np.ndarray or ExData
> >
> > > Either a 2 by n dimensional np.ndarray or an ExData type ob-
> > > ject. In the former case, n is the number of energy levels, with
> > > the first column containing energy level indices starting at 1,
> > > and the second column containing the absolute experimental
> > > energy of the corresponding level. In order to specify energy
> > > level differences, or specify energies according to their SLJM
> > > state labels, use the ExData interface.
> >
> > **shx** : dict
> >
> > > Specifies the experimental spin Hamiltonian data. Valid keys
> > > are 'zeeman', 'hyperfine', and 'quadrupole'. Values should
> > > be 3×3 np.ndarrays corresponding to the experimental spin
> > > Hamiltonian tensor.

weights : dict

> Set the weighting for χ^2 contributions of terms to be fit. Valid keys are 'energy', 'zeeman', 'hyperfine', and 'quadrupole'; corresponding values should be floats. Any omitted values will be set to unity.

ignore_ndof : bool, optional

> Force minimization even if there are fewer observables than parameters; use at your own peril.

Methods

`fit`(*self, min_object*)

> Run the fit using the provided minimization object.

> ### Parameters

> **min_object** : CFLMin

> > The minimization object to be used, which sets the optimization algorithm, bounds and other settings as applicable to the selected algorithm.

> ### Returns

> **result** : tuple

> > The first element is a np.ndarray containing complex coefficients while the second entry contains the final value of the objective function.

class `cfl.CFLMin`

> Object for initializing and configuring minimization routines to be passed to e_fit or esh_fit.

> ### Parameters

> **method** : string

> > The minimization routine to employ. Available options are:
> > - 'basinhopping'
> > - 'nlopt_cobyla'
> > - 'nlopt_bobyqa'
> > - 'nlopt_sbplx'

- 'nlopt_crs2_lm'
- 'nlopt_esch'.

bounds : dict, optional

Parameter bounds. Keys specify the tensor name (note that tensors created by tensor arithmetic should have their name attribute set explicitly), while values correspond to tuples, the first entry of which is the lower bound and the second entry the upper bound. The number of elements in bounds must match the length of the parameters list.

cov : bool, optional

Evaluate the covariance matrix for the fit; defaults to False.

lmin : CFLMin, optional

The local minimization routine to be used by the basinhopping algorithm; defaults to nlopt_bobyqa. Implemented options fall into two categories, routines from gsl, and routines from nlopt. For the former, available algorithms are:

- 'gsl_nmsimplex2'
- 'gsl_conjugate_fr'
- 'gsl_conjugate_pr'
- 'gsl_vector_bfgs2'

For the latter, available algorithms are:

- 'nlopt_cobyla'
- 'nlopt_bobyqa'
- 'nlopt_sbplx'.

stepsize : dict, optional

The stepsize for parameter variation; presently only supported for the basinhopping algorithm. Keys specify the tensor name, while values correspond to the stepsize. If adaptive stepsize is enabled (default, see CFLMin doc for details), then this dictionary is used as the starting stepsize, and all step sizes are scaled by the same factor in order to achieve the target acceptance rate. In other words, this kwarg is then used to set the relative proportion between the step sizes.

niter : int, optional

    The number of basinhopping iterations to complete. Defaults to 100.

xtol : float, optional

    If either the global optimization or a local basinhopping minimization routine is from nlopt, the `xtol` argument can be used to set the relative tolerance in parameters x to be used as a stopping criteria. Defaults to 1e-5.

Methods

`minimize`(*self*, *fit_obj*, *x0*)

    Run the minimization.

Parameters

fit_obj : EFitRunner or ESHFitRunner

    The object for which to perform the fit.

x0 : np.ndarray

    Real valued vector. Upon entry, these are the initial guesses for the parameters; if minimization is successful, x0 will be overwritten with the solution.

`cfl.e_fit`(*parameters*, *h*, *ex*, *cfl_min*, ***kwargs*)

Fit parameters to energy level data.

The Hamiltonian must have coefficients set with set_coeff, since these are used as initial estimates for the parameters to-be-fit. The type of coefficients when the are set also determines whether they are fit as real or complex parameters.

Parameters

parameters : list

    A list of tensor objects for which to vary the prefactor.

h : Hamiltonian

    The Hamiltonian for which to fit the energy levels.

ex : np.ndarray

    Either a 2 by n dimensional np.ndarray or an ExData type object. In the former case, n is the number of energy levels, with

the first column containing energy level indices starting at 1, and the second column containing the absolute experimental energy of the corresponding level. In order to specify energy level differences, or specify energies according to their SLJM state labels, use the ExData interface.

cfl_min : CFLMin

The minimization object which sets the optimization algorithm and corresponding options.

ignore_ndof : bool, optional

Force minimization even if there are fewer observables than parameters; use at your own peril.

`cfl.`**`mh_fit`**(*parameters*, *h_list*, *weights_list*, *ex_list*, *cfl_min*, ***kwargs*)

Class used to store data required by, and to run, a crystal field fit using multiple eigenvalue vectors. Typically, this would consist of one vector of energy levels at zero field without hyperfine or quadrupole interactions, complemented by a set of eigenvalue vectors at linearly independent magnetic field orientations and possibly containing hyperfine interactions. These additional eigenvalues can either be measured or synthetically calculated for specific crystal field levels from spin Hamiltonian data.

The Hamiltonians must have coefficients set with set_coeff, since these are used as initial estimates for the parameters to-be-fit. The type of coefficients when they are set also determines whether they are fit as real or complex parameters, thus they must be consistent among each Hamiltonian.

Parameters

parameters : list

A list of tensor objects for which to vary the prefactor.

h_list : list

A list of Hamiltonians, each containing the interactions required to match the corresponding experimental energy level data.

weights_list : list

A list of floating point weights that determine the weighting added to the chi^2 contribution of each eigenvalue vector.

      ex_list : list

          Either a list of 2 by n dimensional np.ndarrays or a list of ExData type objects. In the former case, n is the number of energy levels, with the first column of each array containing energy level indices starting at 1, and the second column containing the absolute experimental energy of the corresponding level. In order to specify energy level differences, or specify energies according to their SLJM state labels, use the ExData interface.

      ignore_ndof : bool, optional

          Force minimization even if there are fewer observables than parameters; use at your own peril.

`cfl.`**`esh_fit`**(*parameters*, *h*, *sh*, *ex*, *shx*, *weights*, *cfl_min*, ***kwargs*)

    Fit parameters to energy level data.

    The Hamiltonian must have coefficients set with set_coeff, since these are used as initial estimates for the parameters to-be-fit. The type of coefficients when they are set also determines whether they are fit as real or complex parameters.

      Parameters

      parameters : list

          A list of tensor objects for which to vary the prefactor.

      h : Hamiltonian

          The Hamiltonian for which to fit the energy levels.

      sh : SpinHamiltonian

          The spin Hamiltonian object to be fit.

      ex : np.ndarray

          Either a 2 by n dimensional np.ndarray or an ExData type object. In the former case, n is the number of energy levels, with the first column containing energy level indices starting at 1, and the second column containing the absolute experimental energy of the corresponding level. In order to specify energy level differences, or specify energies according to their SLJM state labels, use the ExData interface.

shx : dict

Specifies the experimental spin Hamiltonian data. Valid keys are 'zeeman', 'hyperfine', and 'quadrupole'. Values should be 3×3 np.ndarrays corresponding to the experimental spin Hamiltonian tensor.

weights : dict

Set the weighting for χ^2 contributions of terms to be fit. Valid keys are 'energy', 'zeeman', 'hyperfine', and 'quadrupole'; corresponding values should be floats. Any omitted values will be set to unity.

cfl_min : CFLMin

The minimization object which sets the optimization algorithm and corresponding options.

ignore_ndof : bool, optional

Force minimization even if there are fewer observables than parameters; use at your own peril.

A.2 `import_sljm` – parse emp sljm matrix elements

class `import_sljm.ImportSLJM`(*name*)

Import the matrix elements and state labels from an SLJM calc plain text file.

Parameters

name : string

The path/name of the SLJM calc output files, specifically, the files `name.txt` containing the matrix elements in plain text, `name.mi_` containing the tensor dimensions, and the states file `name.st_`.

dim : int

The dimension of the tensors.

Methods

`print_names()`

> Print the names of all the tensors that have been loaded.

`import_sljm.`**`get_state_number`**(*source*)

> Generator for extracting the number of states from a `*.st_` file.

`import_sljm.`**`get_tensor_dim`**(*source*)

> Generator for extracting tensor dimensions from `*.mi_` files.

A.3 `cfl_util` – utility functions for `cfl`

`cfl_util.`**`L2term`**(*i*)

> Convert an L quantum number numerical value to its term character.
>
> > **Parameters**
> >
> > > **i** : integer
> > >
> > > > The L quantum number numerical value to be converted.

`cfl_util.`**`bal_bounds`**(*coeff*, *bounds*)

> Helper function for creating balanced bounds dictionary. That is, the bounds are are some constant, symmetric, ± offset from the starting coefficient values.
>
> > **Parameters**
> >
> > > **coeff** : dict
> > >
> > > > Coefficient initial value dictionary.
> > >
> > > **bounds** : dict
> > >
> > > > Dictionary of single bounds values for each parameter to be fit, which will be added/subtracted from the initial coeff value.
> > >
> > > **Returns** :
> > >
> > > **bal_bounds** : dict
> > >
> > > > The balanced bounds dictionary.

`cfl_util.`**`e_fit_sigma`**(*e*, *ex*, *ndof*, *z=None*, *labels=None*)

> Calculate the standard deviation of an energy level fit assuming a model fit. See Chapter 15 (page 780) of Numerical Recipes, 3rd edition.
>
> > **Parameters**
> >
> > > **e** : np.ndarray
> > >
> > > > The energies of fitted levels.

       ex : np.ndarray

          Either a 2 by n dimensional np.ndarray or an ExData type object. In the former case, n is the number of energy levels, with the first column containing energy level indices starting at 1, and the second column containing the absolute experimental energy of the corresponding level. In order to specify energy level differences, or specify energies according to their SLJM state labels, use the ExData interface.

       ndof : int

          The number of degrees of freedom of the chi-squared distribution, that is, the number of experimental data points minus the number of parameters.

       z : np.ndarray, optional

          The eigenvector array the principal components of which are used to sort state-labels. This must be specified if ex is an ExData object.

       labels : list, optional

          A list of state labels. This must be specified if ex is an ExData object.

`cfl_util.`**`ex_parse_helper`**(*ex*, *z*, *labels*)

    Helper for creating print-compatible ex array from ExData object.

       Parameters

       ex : ExData

          The objected to be parsed.

       z : np.ndarray

          The eigenvector array the principal components of which are used to sort state-labels.

       labels : list

          A list of state labels.

`cfl_util.`**`gen_e_summary`**(*w*, *z*, *labels*, *label_key*, *ex=None*, *nstates=2*, *sigma=None*, *e_shift=False*)

    Generate energy level summary given eigenvalues and eigenvectors.

       Parameters

w : np.ndarray

The eigenvalue vector, of length n.

z : np.ndarray

The eigenvectors in an n by n matrix.

labels : list

A list of state labels.

label_key : str

String identifying the type of label. Valid characters are S, L, J, M, I, T, and F and their position in label_key specifies the location in each label.

ex : np.ndarray, optional

Either a 2 by n dimensional array or a 3 by n dimensional array, with n the number of available experimental energy level observables. The two column case is used to specify only absolute energy levels. In this instance, the first column contains energy level indices starting at 1, and the second column contains the absolute experimental energy of the corresponding level. The three column case is used to specify a combination of absolute energy levels and energy differences. For absolute energies, the first column again contains energy level indices starting at 1, while the second column should be set to -1, and the third column contains the corresponding absolute experimental energy. For energy differences, the first column specifies the initial energy level index, the second column specifies the final energy level index, and the third column corresponds to the energy difference.

nstates : int, optional

The number of constituent states to display for mixed states.

sigma : float, optional

The standard deviation for the energy level chi^2.

e_shift : bool, optional

Shift entire eigenvalue spectrum s.t. the first eigenvalue is zero.

`cfl_util.`**`gen_fit_summary`**(*coeff*, *fit_obj*, *method*, *fmin*, *sigma=None*,
                              ***kwargs*)

    Create a string summarizing a crystal-field Hamiltonian fitting run.

      Parameters

        coeff : dict

          Contains the fitted interaction coefficients.

        fit_obj : EFitRunner, MevFitRunner, or ESHFitRunner

          Must have __iter__ method that iterates over names of tensors.

        method : str

          The optimization algorithm used for the fit.

        sigma : float, optional

          The total uncertainty for both the energy level and spin Hamiltonian fits; must be specified if 'cov'=True in kwargs.

        kwargs: dict :

          Additional, optimization algorithm specific, settings to print.

`cfl_util.`**`gen_pycf_summary`**()

    Print the pycf version and date/time.

`cfl_util.`**`gen_sh_summary`**(*param*, *sh*, *shx=None*, *sigma=None*)

    Generate a spin Hamiltonian summary displaying calculated and experimental spin Hamiltonian data.

      Parameters

        param : list

          Elements must be 3×3 np.ndarrays corresponding to the spin Hamiltonian parameters. Output from `cfl.SpinHamiltonian.calc_param()` is appropriately formated to be passed as param.

        sh : SpinHamiltonian

          Generally the spin Hamiltonian object used to generate the param list.

        shx : dict, optional

          Specifies the experimental spin Hamiltonian data for comparison. Valid keys are 'zeeman', 'hyperfine', and 'quadrupole'. Values should be 3×3 np.ndarrays corresponding to the ex-

perimental spin Hamiltonian tensor.

> **sigma** : float, optional
>
> > The standard deviation for the spin Hamiltonian chi^2.

`cfl_util.`**`print_as_c_array`**(*a*)

> Print a two dimensional numpy array in a form that makes it easy to include in a C program, using row major ordering.

`cfl_util.`**`print_as_fortran_array`**(*a*)

> Print a two dimensional numpy array in a form that makes it easy to include in a c program, using column major ordering.

`cfl_util.`**`sh_fit_sigma`**(*param*, *sh*, *shx*, *ndof*)

> Calculate the standard deviation of a spin Hamiltonian fit assuming a model fit. See Chapter 15 (page 780) of Numerical Recipes, 3rd edition.
>
> > **Parameters**
> >
> > > **param** : list
> > >
> > > > Elements must be 3×3 np.ndarrays corresponding to the spin Hamiltonian parameters. Output from `cfl.SpinHamiltonian.calc_param()` is appropriately formated to be passed as param.
> > >
> > > **sh** : SpinHamiltonian
> > >
> > > > Generally the spin Hamiltonian object used to generate the param list.
> > >
> > > **shx** : dict
> > >
> > > > Specifies the experimental spin Hamiltonian data. Valid keys are 'zeeman', 'hyperfine', and 'quadrupole'. Values should be 3×3 np.ndarrays corresponding to the experimental spin Hamiltonian tensor.
> > >
> > > **ndof** : int
> > >
> > > > The number of degrees of freedom of the chi-squared distribution, that is, the number of experimental data points minus the number of parameters.

`cfl_util.`**`term2L`**(*c*)

> Convert an L quantum number term character to its numerical value.
>
> > **Parameters**
> >
> > > **c** : string

The L quantum number term character to be converted.

`cfl_util.`**`uline_char`**(*s*)

Underline all non-whitespace characters in a string, except for single spaces between non-whitespace characters.

A.4 `pyemp` – emp python wrapper

class pyemp.**`BaseEmp`**(*spectrum*, *process=None*, *infiles=None*, ***kwargs*)

Base class for `GenericErun` and `SpectrumData`. Ensures the first argument is an instance of `Spectrum`, and whether all necessary input files have been provided.

class pyemp.**`Cfit`**(*spectrum*, ***kwargs*)

Generate a cfit.dat input file and execute the cfit program.

Parameters

spectrum : Spectrum

The object must have attributes `name`, `emproot`, and keys `addtensors`, and `addassign` and optionally `states` and `tensors`; see the Spectrum docstring for a more detailed description of these attributes.

states : string, optional

The .st_ input file name; must be provided if it was not specified when the Spectrum object was instantiated.

tensors : string, optional

The .mi_ and .mm_ input file name; must be provided if it was not specified when the Spectrum object was instantiated.

Returns

object : Cfit

Notes   Instantiating an object of this type automatically sets the `tvals` keyword of the provided `Spectrum` object. Furthermore, the Cfit log file can be displayed using the print_log() method.

class pyemp.`GenericErun`(*spectrum*,   *process=None*,   *infiles=None*,
                              **kwargs)

> Base class for `Cfit`, `Vtrans`, `Inten` and `SpectrumErun`. Sets up input files
> and handles execution of erun programs, along with erun log files.

> **Methods**
>
> `add_input`(*data*)
>
> > Append data to erun program input file 'name_process.dat'.
>
> `erun`(*spectrum=None*, *outfiles=None*)
>
> > A wrapper for the erun script. Any subclasses of GenericErun must
> > have attributes `self.name` and `self.process`. Additionally, this method
> > writes the logfile output to the file `name_process_log.txt` and ap-
> > pends names of created data files to the `Spectrum` instance.
> >
> > > **Parameters**
> > >
> > > > **spectrum** : Spectrum
> > > >
> > > > > An instance of the Spectrum class.
> > > >
> > > > **outfiles** : list
> > > >
> > > > > The names of files created by the specific erun program.
>
> `print_log`()
>
> > Print the log file generated by by erun for a given GenericErun object.

class pyemp.`Inten`(*spectrum*, ***kwargs*)

> Generate an inten.dat input file and execute the inten program.

> > **Parameters**
> >
> > > **spectrum** : Spectrum
> > >
> > > > The object must have attributes `name`, `emproot`, and keys `edipoletensor`,
> > > > `edipole`, `mdipole`, and `levels` and optionally for `states`,
> > > > `tvals` and `trans`; see the Spectrum docstring for a more de-
> > > > tailed description of these attributes.
> > >
> > > **states** : string, optional
> > >
> > > > The .st_ input file name; must be provided if it was not spec-
> > > > ified when the Spectrum object was instantiated, or for a pre-
> > > > vious `cfit()` of `vtrans()` call.
> > >
> > > **tvals** : string, optional

The .vi_ and .vm_ input file name; must be provided if it was not specified when the Spectrum object was instantiated, or for a previous `vtrans()` call.

trans : string, optional

The .ti_ and .tm_ input file name; must be provided if it was not specified when the Spectrum object was instantiated.

Returns

object : Inten

Notes   Instantiating an object of this type automatically sets the `plt` keyword of the provided `Spectrum` object. Furthermore, the Inten log file can be displayed using the print_log() method.

class pyemp.`Spectrum`(***kwargs*)

Implements all the defining parameters of a Spectrum object.

Parameters

name : string

The name for log and output files.

emproot : string

The path to the linuxemp directory.

states : string

The .st_ input file name - can also be specified when instantiating a `Cfit` object.

tensors : string

The .mi_ and .mm_ input file names - can also be specified when instantiating a `Cfit`, `Vtrans` or `Inten` object.

addtensor : string

Newline separated `addten` statements following cfit input file syntax.

addassign: string :

Newline separated `addassign` statements following cfit input file syntax.

expparams : string, optional

Specifies values for `exptval`, `delta` and `lsq` with their usual cfit input file meaning.

splitplot : dictionary, optional

If specified, `Cfit` will generate and parse splitplot data. Required keys are `energy`, `var` and `range`; see the `SpectrumAxes.splitplot()` method for further details.

spinh : dictionary, or list of dictionaries, optional

If specified, `Cfit` will generate and parse spin Hamiltonian data. Required dictionary keys are

- `terms`, a list of strings with possible values of 'bgs', 'ias' and 'iqi', which enable, respectively, Zeeman interactions, magnetic dipole hyperfine interactions and electric quadrupole hyperfine interactions;

- `levels`, a tuple of integers specifying the lower and upper energy levels for which to generate the spin Hamiltonian.

If the argument is a list of dictonaries then spin Hamiltonian data will be generated for each element.

edconstruct : string

String using the vtrans EDCONSTRUCT input syntax to use transformed tensors to construct the A tensors.

levels : array

Of the form:

```
['initstart', 'initend', 'finstart', 'finend',


'initname', 'finname']
```

where 'initstart' to 'initend' spans the range of initial energy levels, etc.

edipoletensor: string :

>> Newline separated electric dipole tensor assignments passed to the vtrans input file - can also be specified when instantiating a `Vtrans` object.

> **tvals** : string

>> The .vi_ and .vm_ input file names - can also be specified when instantiating a `Vtrans` or `Inten` object.

> **matel** : string

>> The vtrans matrix element .mi_ and .mm_ input file names - can also be specified when instantiating a `Vtrans` object.

> **trans** : string

>> The .ti_ and .tm_ input file names - can also be specified when instantiating an `Inten` object.

> **plotargs** : dictionary

>> Keys of `polarization`, `temp`, `linewidth`, `npoints`, `xrange` and `linewidth`, with some arguments optional depending on which plotting method is used, see the `SpectrumData` and `SpectrumErun` docstrings for details.

> **plt** : string

>> The SpectrumErun input data file, the existence of which is also checked by SpectrumData to ensure Inten was run successfully.

Returns

> **object** : Spectrum

Notes   The following list details attributes of Spectrum objects that need to be called explicitly for certain applications.

sh_terms[list] Elements are dictionaries containing spin Hamiltonian data, set by `Cfit` if the provided Spectrum object was instantiated with the `spinh` kwarg. Keys correspond to the `terms` specified by `spinh` kwarg and values are the respective spin Hamiltonian terms. For the term `bgs` this is a list of three terms for a magnetic field along 'x', 'y' and 'z', respectively.

sh_energies[np.ndarray] Contains spin Hamiltonian energy level data read

from expthelp files, intended for use with `spinhamiltonian.sh_lsq_func()`.

sh_bl[np.ndarray] Contains spin Hamiltonian block and level numbers.

line_energies[np.ndarray] Set by `SpectrumData` or `SpectrumErun`; energy data for individual transitions in wavenumbers, useful for scripting plotting procedure.

line_inten[np.ndarray] Set by `SpectrumData` or `SpectrumErun`; intensity data for individual transitions, useful for scripting plotting procedure.

curve_energies[np.ndarray] Set by `SpectrumData` or `SpectrumErun`; energy data for lineshapes in wavenumbers, useful for scripting plotting procedure.

curve_inten[np.ndarry] Set by `SpectrumData` or `SpectrumErun`; intensity data for lineshapes, useful for scripting plotting procedure.

Methods

`cfit`(***kwargs*)

Generate and return object of type `Cfit`. See the `Cfit` documentation for further details.

`inten`(***kwargs*)

Generate and return object of type `Inten`. See the `Inten` documentation for further details.

`print_log`(*mode='brief'*)

Generate a log of the executed erun programs.

> **Parameters**
>> **mode** : string
>>
>> Allowed values are 'brief' and 'full'. 'brief' will return the erun input parameters of all executed erun programs, whereas 'full' will return the log files of all executed erun programs.
>
> **Returns**
>> **log** : string
>>
>> The log output.

`spectrum_data`(***kwargs*)

> Generate and return object of type SpectrumData. See the SpectrumData documentation for further details.

`spectrum_erun`(***kwargs*)

> Generate and return object of type SpectrumErun. See the SpectrumErun documentation for further details.

`vtrans`(***kwargs*)

> Generate and return object of type Vtrans. See the Vtrans documentation for further details.

class pyemp.`SpectrumAxes`(*fig*, *rect*, *axisbg=None*, *frameon=True*, *sharex=None*, *sharey=None*, *label=u''*, *xscale=None*, *yscale=None*, ***kwargs*)

The SpectrumAxes matplotlib projection; when instantiating an axis object, add the `projection = 'spectrum'` kwarg, then run the spectrumplot method of the returned axis instance which takes as an argument an object of type Spectrum.

To create an axis object one calls the figure constructor, which in turn instantiates the axis object. As a consequence one does not directly instantiate the axis object so that the easiest workaround for adding a plotting method to the axis class is by using the projection option of the figure class.

Notes   In order for the figure class to be aware of the spectrum projection one must run `register_projection(SpectrumAxes)` which requires the `matplotlib.projections.register_projection` module. Importing all of the pycf module automatically handles this.

Methods

`spectrumplot`(*spectrum*, **args*, ***kwargs*)

> Create a spectrum plot from a Spectrum object.

> > **Parameters**

> > > **spectrum** : Spectrum

> > > > The object should have the following spectrum plot specific keywords:

- ●`transitionlabels` enables or disables explicit labels for all plotted transitions - allowed values are `False` (default) or `True`;
- ●`labelsize` the fontsize for transition labels;
- ●`intencutoff` the minimum intensity for transitions to be plotted, primarily useful for suppressing uninteresting transition labels;
- ●`energylabels` if transition labels are enabled, then this option appends the transition energy - allowed values are `False` (default) or `True`.

*args, optional :

Additional arguments are passed passed to the vlines and plot routines have their usual functions.

**kwargs, optional :

Additional keyword arguments are passed passed to the vlines and plot routines have their usual functions.

`splitplot`(*spectrum*, **args*, ***kwargs*)

Create a splitplot from a `Spectrum` object.

Parameters

spectrum : Spectrum

The object must have the `splitplotdata` attribute. This is achieved by adding the `splitplot` keyword to the `Spectrum` object prior to instantiating the `Cfit` object; `splitplot` is a dictionary with keys:

- ●`energy` a list of the form `[min, max]`, where `min` and `max` are integer values of the energy levels to be plotted;
- ●`var` a string of the variable name to be a varied;
- ●`range` a list of the form `[min, max]` where `min` and `max` are floating point numbers indicating the range over which `var` wil be varied.

*args, optional :

Additional arguments are passed to the vlines and plot routines have their usual functions.

> ****kwargs, optional** :
>> Additional keyword arguments are passed to the vlines and plot routines have their usual functions.

class `pyemp.`**`SpectrumData`**(*spectrum*, ***kwargs*)

> Natively generate spectrum data. Intensity data is mined from the inten log file, which provides information such as the initial and final state of a transition.

> ### Parameters
>> **spectrum** : Spectrum
>>> The object must have attributes `plotargs` - a dictionary that must have values for:
>>>> - `polarization` a string, with possible values of `isotropic`, `axial`, `sigma` or `pi`;
>>>> - `temp` an int or float specifying the temperature;
>>>> - `linewidth` an int or float specifying the Lorentzian linewidth;
>>>> - `npoints` an optional argument specifying the number of points for the spectrum curve;
>>>
>>> and optionally `plt` - the filename of the data created by inten, which while unused is employed as an indicator of whether inten executed successfully.
>>
>> **plt** : string
>>> The filename of the data created by inten, which must be specified here if it is not a Spectrum attribute.

> ### Returns
>> **object** : SpectrumData

Notes Instantiating an object of this type adds a `transitions` attribute to the provided Spectrum object, which returns a list of dictionaries, corresponding to distinct transitions, where each transition has keys:

initialstate[string] The initial state label.

finalstate[string] The final state label.

energy[string] The transition energy.

isotropic[string] The isotropic dipole strength.

axial[string] The axial dipole strength.

sigma[string] The sigma dipole strength.

pi[string] The pi dipole strength.

class pyemp.`SpectrumErun`(*spectrum*, ***kwargs*)

Facilitates the loading of c spectrum output files, or the execution of the c spectrum program and the subsequent loading of output files.

Parameters

spectrum : Spectrum

The object must have attributes `plotargs`, a dictionary with values:

- `polarization` a string, with possible values of `isotropic`, `axial`, `sigma` or `pi`;

- `temp` an int or float specifying the temperature, required if `action = exec` (see below);

- `linewidth` an int or float specifying the Lorentzian linewidth, required if `action = exec` (see below);

- `xrange` a list of the form [`min`, `max`] where `min` and `max` specify the lower and upper bound of the spectrum curve, respectively, required if `action = exec` (see below);

and optionally `plt` - the filename of the data created by inten.

plt : string

The filename of the data created by inten, which must be specified here if it is not a Spectrum attribute.

action : string

Kwarg, with allowed values of `load` (default) and `exec`, to change between loading existing `lines.gp` and `curves.gp_` files or first executing the c spectrum program and then loading the resulting files.

Returns

object : SpectrumErun

Notes   The SpectrumErun log file can be displayed using the print_log()
method.

class pyemp.`Vtrans`(*spectrum*, ***kwargs*)

Generate a vtrans.dat input file and execute the vtrans program.

Parameters

spectrum : Spectrum

The object must have attributes `name`, `emproot`, and keys
`edconstruct`, and `levels` and optionally for `states`, `tvals`
and `matel`; see the Spectrum docstring for a more detailed
description of these attributes.

states : string, optional

The .st_ input file name; must be provided if it was not spec-
ified when the Spectrum object was instantiated, or for a pre-
vious `cfit()` call.

tvals : string, optional

The .vi_ and .vm_ input file name; must be provided if it was
not specified when the Spectrum object was instantiated.

matel : string, optional

The vtrans matrix element .mi_ and .mm_ input file name;
must be provided if it was not specified when the Spectrum
object was instantiated.

Returns

object : Vtrans

Notes   Instantiating an object of this type automatically sets the `trans` key-
word of the provided `Spectrum` object. Furthermore, the Vtrans log file can
be displayed using the print_log() method.

A.5 `spinh` – spin Hamiltonian calculations

class spinh.`SpinH`(*terms*, ***kwargs*)

>Container for holding data about the spin Hamiltonian. Can either be used to calculate the full spin Hamiltonian from individual terms, or to invert the spin Hamiltonian and recover the spin Hamiltonian parameters. If used for the former, the object is instantiated and then spin Hamiltonian terms are added with the `add_term()` method. The full Hamiltonian can then be returned using the `get_H()` method. If used for the latter, terms are added as arrays with dimensions of the full Hamiltonian using the `add_H_term()` method. The spin Hamiltonian parameters can then be calculated using the `inv_term()` method.

>**Parameters**

>>**terms** : list

>>>Elements are strings with possible values 'bgs', 'ias' and 'iqi'. The choice of elements affects what other keyword arguments are required; see below.

>>**B** : numpy.ndarray or list with numpy.ndarray elements

>>>A 3 by 1 vector containing values for the magnetic field strengths B_x, B_y and B_z; if `terms` contains 'bgs' this keyword argument must be specified. Furthermore, if `'inv' = True`, this must be a list of magnetic field strength vectors, with a minimum of three linearly independent vectors required for a fully determined solution.

>>**S** : float

>>>The spin projection S_z; if `terms` contains 'bgs' or 'ias' this keyword argument must be specified.

>>**I** : float

>>>The nuclear spin projection I_z; if `terms` contains 'ias' or 'iqi' this keyword argument must be specified.

>>**inv** : boolean, optional

>>>If True, the coefficient arrays for term inversion are pre-computed.

>**Returns**

object : SpinH

Methods

`add_H_term`(*term*, *val*)

Extract the specified term from the full Hamiltonian and update the appropriate term value of the SpinH object.

Parameters

term : string

Specifies the term; must be one of the values of the `term` list specified when the SpinH object was instantiated.

val : numpy.ndarray or list

The value of the specified term. For 'bgs' this must be a list of numpy.ndarrays, with elements in the list in the same order as the B list used to instantiate the SpinH object.

`add_term`(*term*, *m*)

Add the specified term to the spin Hamiltonian.

Parameters

term : string

Specifies the term; must be one of the values of the `term` list provided when the SpinH object was instantiated.

m : numpy.ndarray

A 3 by 3 matrix providing the parameters for the specified spin Hamiltonian term.

`get_H`()

Calculate the full Hamiltonian and return the result.

`inv_term`(*term*, *sym=False*)

Invert the specified term of this spin Hamiltonian.

Parameters

term : string

Specifies the term; must be one of the values of the `term` list specified when the SpinH object was instantiated.

sym : bool

Set to True to enable spin Hamiltonian parameter symme-
terization.

Returns

term_parameters : numpy.ndarray

A 9 by 1 vector consisting of stacked rows of the corre-
sponding 3 by 3 term parameter matrix.

spinh.**bgs**(v, m, t)

Generate the BgS term, an array of size $(2 \times j + 1)$ by $(2 \times j + 1)$, with j
the angular momentum of the rank one tensor S.

Parameters

v : numpy.ndarray

A 3 by 1 vector of magnetic field strengths B_x, B_y and B_z.

m : numpy.ndarray

The 3 by 3 Zeeman parameter matrix g.

t : list

Elements consist of the matrix elements of S_x, S_y and S_z.

Returns

result : array

spinh.**bgs_coeff_array**(v, t)

Generate the BgS coefficient array. This consists of a $2j + 1 \times 2j + 1$ by
3×3 array containing the matrix elements of the terms $B_a S_b$, with $a, b \in$
$\{x, y, z\}$ and j the angular momentum of the rank one tensor S. Here the
rows enumerate the $2j + 1 \times 2j + 1$ different state combinations while the
columns enumerate all combinations of a and b. This array is independent
of S and is intended to be computed once, then employed with numpy's
lstsq() function to calculate S given a BgS matrix.

Parameters

v : numpy.ndarray

A 3 by 1 vector of magnetic field strengths B_x, B_y and B_z.

t : list

Elements consist of the matrix elements of S_x, S_y and S_z.

Returns

result : numpy.ndarray

A $2j + 1 \times 2j + 1$ by 3×3 array.

`spinh.ias`(*t1*, *m*, *t2*)

Generate the IAS term, an array of size $(2 \times j_1 + 1) \times (2 \times j_2 + 1)$ by $(2 \times j_1 + 1) \times (2 \times j_2 + 1)$, with j_1 and j_2 the angular momentum of the rank one tensors A and I, respectively.

Parameters

t1 : list

Elements consist of the matrix elements of I_x, I_y and I_z.

m : numpy.ndarray

The 3 by 3 dipole parameter matrix A.

t2 : list

Elements consist of the matrix elements of S_x, S_y and S_z.

Returns

result : array

`spinh.ias_coeff_array`(*t1*, *t2*)

Generate the IAS coefficient array. This consists of a $2j_1 + 1 \times 2j_2 + 1$ by 3×3 array containing the matrix elements of the operators $I_a S_b$, with $a, b \in \{x, y, z\}$ and j_1 and j_2 the angular momentum of the rank one tensors I and S, respectively. Here the rows enumerate the $2j_1 + 1 \times 2j_2 + 1$ different state combinations while the columns enumerate all combinations of a and b. This array is independent of A and is intended to be computed once, then employed with numpy's `lstsq()` function to calculate A given an IAS matrix.

Parameters

t1 : list

Elements consist of the matrix elements of I_x, I_y and I_z.

t2 : list

Elements consist of the matrix elements of S_x, S_y and S_z.

Returns

result : numpy.ndarray

A $2j_1 + 1 \times 2j_2 + 1$ by 3×3 array.

`spinh.invert_term`(*coeff_a*, *b*)

Invert a spin Hamiltonian term.

Parameters

term : np.ndarray

The matrix elements of the term.

coeff_a : np.ndarray

The appropriate coefficient array, generated with either `bgs_coeff_array()`, `ias_coeff_array()` or `iqi_coeff_array()`.

b : numpy.ndarray

For a 'BgS' term, b must be a $3 \times 2 \times 2$ array, corresponding to individual 'BgS' matrix elements for a field along three linearly independent directions. For an 'IAS' term, b must be a $2(I + 1) \times 2$ np.ndarray corresponding to the IAS matrix elements.

Returns

result : numpy.ndarray

A 9 by 1 vector, consisting of stacked rows of the 3 by 3 term parameter matrix.

spinh.`iqi`(t, m)

Generate the IQI term, an array of size $(2 \times j + 1)$ by $(2 \times j + 1)$, with j the angular momentum of the rank one tensor I.

Parameters

t : list

Elements consist of the matrix elements of I_x, I_y and I_z.

m : numpy.ndarray

The 3 by 3 quadrupole parameter matrix Q.

Returns

result : array

spinh.`iqi_coeff_array`(t)

Generate the IQI coefficient array. This consists of a $2j + 1 \times 2j + 1$ by 3×3 array containing the matrix elements of the operators $I_a I_b$, with $a, b \in \{x, y, z\}$ and j the angular momentum of the rank one tensor I. Here the rows enumerate the $2j + 1 \times 2j + 1$ different state combinations while the columns enumerate all combinations of a and b. This array is independent of Q and is intended to be computed once, then employed with numpy's

`lstsq()` function to calculate Q given an IQI matrix.

Parameters

t : list

Elements consist of the matrix elements of I_x, I_y and I_z.

Returns

result : numpy.ndarray

A $2j + 1 \times 2j + 1$ by 3×3 array.

`spinh.`**`su2_rz`**(p, m)

Apply an SU(2) rotation about the z-axis of the spin-half matrix elements of a spin Hamiltonian term, specifically, a Zeeman interaction term or a magnetic dipole hyperfine interaction term.

Parameters

p : float

The phase ϕ of an SU(2) rotation $\mathscr{D}_z(\phi)$.

m : ndarray

A 2×2 Zeeman interaction term, or a $2 \times (I + 1) \times 2$ by $2 \times (I + 1) \times 2$ magnetic dipole hyperfine interaction term.

Returns

m : ndarray

The transformed matrix.

`spinh.`**`su2_rz_lsq_f`**$(p, coeff\_a, b)$

Helper function for least squares fitting of the SU(2) rotation required to symmetrize spin Hamiltonian terms containing spin half matrix elements.

Parameters

p : float

The phase to be varied.

coeff_a : np.ndarray

The appropriate coefficient array, generated with either `bgs_coeff_array()` or `ias_coeff_array()`.

b : numpy.ndarray

For a 'BgS' term, b must be a $3 \times 2 \times 2$ array, corresponding to individual 'BgS' matrix elements for a field along three linearly independent directions. For an 'IAS' term, b must be

a $2(I + 1) \times 2$ np.ndarray corresponding to the IAS matrix elements.

Returns

> **r** : float
>
> > The residue; calculated from the differences between the off diagonal elements of the spin Hamiltonian tensor.

A.6 `matel` – Matrix element function

`matel.matel`(c, j)

Calculate the matrix elements for $\langle jm_1|J_a|jm_2\rangle$, where $a \in \{x, y, z\}$ for $m_1 = j, j - 1 \ldots - j$ and $m_2 = j, j - 1, \ldots - j$.

Parameters

> **j** : integer or half-integer
>
> > The value of j.
>
> **c** : string
>
> > The component label, a value of either 'jx', 'jy', or 'jz'.

Returns

> **matel** : numpy array
>
> > A $2j + 1$ by $2j + 1$ array, with rows and columns enumerated by m_1 and m_2 respectively.

`matel.t_q`$(j1, j2, m1, m2, q)$

Calculate the matrix element $\langle j_1 m_1|T_q^{(1)}|j_2 m_2\rangle$, where $T_q^{(1)}$ is a rank one tensor.

Parameters

> **j1** : integer or half-integer
>
> > The value of j_1.
>
> **j2** : integer or half-integer
>
> > The value of j_2.
>
> **m2** : integer or half-integer
>
> > The value of m_2.
>
> **m2** : integer or half-integer
>
> > The value of m_2.

q : integer or half-integer

The value of q.

Returns

element : complex

The matrix element $\langle j_1 m_1 | T_q^{(1)} | j_2 m_2 \rangle$.

A.7 `njsymbols` – njsymbol functions

`njsymbols.`**`tricon_ck`**(a, b, c)

Triangular condition check; returns True if the triangular condition on the three integers or half-integers a, b and c is satisfied.

`njsymbols.`**`wigner_3j`**$(j1, j2, j3, m1, m2, m3)$

Calculate the Wigner 3j symbol, give in terms of the Clebsch-Gordon coefficents as

$$\begin{pmatrix} j_1 & j_2 & j_3 \\ m_1 & m_2 & m_3 \end{pmatrix} = \frac{(-1)^{(j_1 - j_2 - m_3)}}{\sqrt{2j_3 + 1}} \langle j_1 m_1 j_2 m_2 | j_3 - m_3 \rangle.$$

Parameters

j1 : integer or half-integer

The value of j_1.

j2 : integer or half-integer

The value of j_2.

j3 : integer or half-integer

The value of j_3.

m1 : integer or half-integer

The value of m_1.

m2 : integer or half-integer

The value of m_2.

m3 : integer or half-integer

The value of m_3.

Returns

result : float

The numerical value of the 3j symbol.

Notes   Uses the recursive algorithm for Clebsch-Gordon coefficients from page 44, Edmonds - Angular Momentum in Quantum Mechanics.

njsymbols.`wigner_6j`(a, b, c, d, e, f)

Calculate the Wigner 6j symbol

$$\begin{Bmatrix} j_1 & j_2 & j_3 \\ l_1 & l_2 & l_3 \end{Bmatrix}.$$

Parameters

a : integer or half-integer

The value of j_1.

b : integer or half-integer

The value of j_2.

c : integer or half-integer

The value of j_3.

d : integer or half-integer

The value of l_1.

e : integer or half-integer

The value of l_2.

f : integer or half-integer

The value of l_3.

Returns

result : float

The numerical value of the 6j symbol.

Notes   Uses the algorithm on page 99 of Edmonds - Angular Momentum in Quantum Mechanics.

njsymbols.`wigner_9j`$(a, b, c, d, e, f, g, h, i)$

Calculate the Wigner 9j symbol

$$\begin{Bmatrix} j_{11} & j_{12} & j_{13} \\ j_{21} & j_{22} & j_{23} \\ j_{31} & j_{32} & j_{33} \end{Bmatrix}.$$

Parameters

a : integer or half-integer

The value of j_{11}.

b : integer or half-integer

The value of j_{12}.

c : integer or half-integer

The value of j_{13}.

d : integer or half-integer

The value of j_{21}.

e : integer or half-integer

The value of j_{22}.

f : integer or half-integer

The value of j_{23}.

g : integer or half-integer

The value of j_{31}.

h : integer or half-integer

The value of j_{32}.

i : integer or half-integer

The value of j_{33}.

Returns

result : float

The numerical value of the 9j symbol.

Notes   Uses the definition on page 101 in terms of 6j symbols of Edmonds
- Angular Momentum in Quantum Mechanics.

References

[1] M. A. Nielsen and I. L. Chuang, *Quantum Computation and Quantum Information* (Cambridge University Press, 2010).

[2] T. D. Ladd, F. Jelezko, R. Laflamme, Y. Nakamura, C. Monroe, and J. L. O'Brien, "Quantum computers," Nature **464**, 45 (2010).

[3] R. M. Macfarlane, "High-resolution laser spectroscopy of rare-earth doped insulators: a personal perspective," Journal of Luminescence **100**, 1 (2002).

[4] P. Goldner, A. Ferrier, and O. Guillot-Noël, "Rare Earth-Doped Crystals for Quantum Information Processing," in *Handbook on the Physics and Chemistry of Rare Earths*, Vol. 46, edited by J.-C. G. Bünzli and V. K. Pecharsky (Elsevier, 2015).

[5] E. Knill, R. Laflamme, and G. J. Milburn, "A scheme for efficient quantum computation with linear optics," Nature **409**, 46 (2001).

[6] A. I. Lvovsky, B. C. Sanders, and W. Tittel, "Optical quantum memory," Nature Photonics **3**, 706 (2009).

[7] J. F. Dynes, H. Takesue, Z. L. Yuan, A. W. Sharpe, K. Harada, T. Honjo, H. Kamada, O. Tadanaga, Y. Nishida, M. Asobe, and A. J. Shields, "Efficient entanglement distribution over 200 kilometers," Optics Express **17**, 11440 (2009).

[8] J. Yin, J.-G. Ren, H. Lu, Y. Cao, H.-L. Yong, Y.-P. Wu, C. Liu, S.-K. Liao, F. Zhou, Y. Jiang, X.-D. Cai, P. Xu, G.-S. Pan, J.-J. Jia, Y.-M. Huang, H. Yin, J.-Y. Wang, Y.-A. Chen, C.-Z. Peng, and J.-W. Pan, "Quantum teleportation and entanglement distribution over 100-kilometre free-space channels," Nature **488**, 185 (2012).

[9] H.-J. Briegel, W. Dür, J. I. Cirac, and P. Zoller, "Quantum Repeaters: The Role of Imperfect Local Operations in Quantum Communication," Physical Review Letters **81**, 5932 (1998).

[10] L.-M. Duan, M. D. Lukin, J. I. Cirac, and P. Zoller, "Long-distance quantum communication with atomic ensembles and linear optics," Nature **414**, 413 (2001).

[11] M. Zhong, M. P. Hedges, R. L. Ahlefeldt, J. G. Bartholomew, S. E. Beavan, S. M. Wittig, J. J. Longdell, and M. J. Sellars, "Optically addressable nuclear spins in a solid with a six-hour coherence time," Nature **517**, 177 (2015).

[12] B. Henderson and R. H. Bartram, *Crystal-Field Engineering of Solid-State Laser Materials* (Cambridge University Press, 2005).

[13] R. W. Equall, Y. Sun, R. L. Cone, and R. M. Macfarlane, "Ultraslow optical dephasing in Eu^{3+}:Y_2SiO_5," Physical Review Letters **72**, 2179 (1994).

[14] Y. Sun, C. W. Thiel, R. L. Cone, R. W. Equall, and R. L. Hutcheson, "Recent progress in developing new rare earth materials for hole burning and coherent transient applications," Journal of Luminescence Proceedings of the Seventh International Meeting on Hole Burning, Single Molecules and Related Spectroscopies: Science and Applications, **98**, 281 (2002).

[15] T. W. Mossberg, "Time-domain frequency-selective optical data storage," Optics Letters **7**, 77 (1982).

[16] R. M. Macfarlane and R. M. Shelby, "Coherent transient and holeburning spectroscopy of rare earth ions in solids," in *Spectroscopy of solids containing rare earth ions*, edited by A. A. Kaplyanskii and R. M. Macfarlane (North-Holland, Amsterdam, 1987).

[17] N. W. Carlson, L. J. Rothberg, A. G. Yodh, W. R. Babbitt, and T. W. Mossberg, "Storage and time reversal of light pulses using photon echoes," Optics Letters **8**, 483 (1983).

[18] H. Lin, T. Wang, G. A. Wilson, and T. W. Mossberg, "Experimental demonstration of swept-carrier time-domain optical memory," Optics Letters **20**, 91 (1995).

[19] H. Lin, T. Wang, G. A. Wilson, and T. W. Mossberg, "Heterodyne detection of swept-carrier frequency-selective optical memory signals," Optics Letters **20**, 928 (1995).

[20] X. A. Shen and R. Kachru, "Experimental demonstration of impulse-equivalent time-domain optical memory," Optics Letters **21**, 2020 (1996).

[21] Y. Li, A. Hoskins, F. Schlottau, K. H. Wagner, C. Embry, and W. R. Babbitt, "Ultrawideband coherent noise lidar range-Doppler imaging and signal processing by use of spatial-spectral holography in inhomogeneously broadened absorbers," Applied Optics **45**, 6409 (2006).

[22] W. R. Babbitt and J. A. Bell, "Coherent transient continuous optical processor," Applied Optics **33**, 1538 (1994).

[23] "S2 corporation," http://www.s2corporation.com/, accessed: 2015-12-25.

[24] T. L. Harris, K. D. Merkel, R. K. Mohan, T. Chang, Z. Cole, A. Olson, and W. R. Babbitt, "Multigigahertz range-Doppler correlative signal processing in optical memory crystals," Applied Optics **45**, 343 (2006).

[25] T. Chang, M. Tian, R. K. Mohan, C. Renner, K. D. Merkel, and W. R. Babbitt, "Recovery of spectral features readout with frequency-chirped laser fields," Optics Letters **30**, 1129 (2005).

[26] M. Colice, F. Schlottau, and K. H. Wagner, "Broadband radio-frequency spectrum analysis in spectral-hole-burning media," Applied Optics **45**, 6393 (2006).

[27] J. Ruggiero, J.-L. Le Gouët, C. Simon, and T. Chanelière, "Why the two-pulse photon echo is not a good quantum memory protocol," Physical Review A **79**, 053851 (2009).

[28] N. Sangouard, C. Simon, J. Minář, M. Afzelius, T. Chanelière, N. Gisin, J.-L. Le Gouët, H. de Riedmatten, and W. Tittel, "Impossibility of faithfully storing single photons with the three-pulse photon echo," Physical Review A **81**, 062333 (2010).

[29] S. A. Moiseev and S. Kröll, "Complete reconstruction of the quantum state of a single-photon wave packet absorbed by a doppler-broadened transition," Physical Review Letters **87**, 173601 (2001).

[30] M. Nilsson and S. Kröll, "Solid state quantum memory using complete absorption and re-emission of photons by tailored and externally controlled inhomogeneous absorption profiles," Optics Communications **247**, 393 (2005).

[31] M. P. Hedges, J. J. Longdell, Y. Li, and M. J. Sellars, "Efficient quantum memory for light," Nature **465**, 1052 (2010).

[32] H. de Riedmatten, M. Afzelius, M. U. Staudt, C. Simon, and N. Gisin, "A solid-state light–matter interface at the single-photon level," Nature **456**, 773 (2008).

[33] I. Usmani, M. Afzelius, H. de Riedmatten, and N. Gisin, "Mapping multiple photonic qubits into and out of one solid-state atomic ensemble," Nature Communications **1**, 12 (2010).

[34] B. Kraus, W. Tittel, N. Gisin, M. Nilsson, S. Kröll, and J. I. Cirac, "Quantum memory for nonstationary light fields based on controlled reversible inhomogeneous broadening," Physical Review A **73**, 020302 (2006).

[35] E. Fraval, M. J. Sellars, and J. J. Longdell, "Method of Extending Hyperfine Coherence Times in Pr^{3+}:Y_2SiO_5," Physical Review Letters **92**, 077601 (2004).

[36] E. Fraval, M. J. Sellars, and J. J. Longdell, "Dynamic decoherence control of a solid-state nuclear-quadrupole qubit," Physical Review Letters **95**, 030506 (2005).

[37] O. Guillot-Noël, P. Goldner, Y. L. Du, E. Baldit, P. Monnier, and K. Bencheikh, "Hyperfine interaction of Er^{3+} ions in Y_2SiO_5: An electron paramagnetic resonance spectroscopy study," Physical Review B **74**, 214409 (2006).

[38] T. Böttger, Y. Sun, C. W. Thiel, and R. L. Cone, "Spectroscopy and dynamics of Er^{3+}:Y_2SiO_5 at 1.5 μm," Physical Review B **74**, 075107 (2006).

[39] Y. Sun, T. Böttger, C. W. Thiel, and R. L. Cone, "Magnetic g tensors for the $I_{15/24}$ and $I_{13/24}$ states of Er^{3+}:Y_2SiO_5," Physical Review B **77**, 085124 (2008).

[40] T. Böttger, C. W. Thiel, R. L. Cone, and Y. Sun, "Controlled compositional disorder in Er^{3+}:Y_2SiO_5 provides a wide-bandwidth spectral hole burning material at 1.5μm," Physical Review B **77**, 155125 (2008).

[41] B. Lauritzen, S. R. Hastings-Simon, H. de Riedmatten, M. Afzelius, and N. Gisin, "State preparation by optical pumping in erbium-doped solids using stimulated emission and spin mixing," Physical Review A **78**, 043402 (2008).

[42] T. Böttger, C. W. Thiel, R. L. Cone, and Y. Sun, "Effects of magnetic field orientation on optical decoherence in Er^{3+}:Y_2SiO_5," Physical Review B **79**, 115104 (2009).

[43] E. Baldit, K. Bencheikh, P. Monnier, S. Briaudeau, J. A. Levenson, V. Crozatier, I. Lorgeré, F. Bretenaker, J. L. Le Gouët, O. Guillot-Noël, and P. Goldner, "Identification of Λ-like systems in Eu^{3+}:Y_2SiO_5 and observation of electromagnetically induced transparency," Physical Review B **81**, 144303 (2010).

[44] B. Lauritzen, J. Minář, H. de Riedmatten, M. Afzelius, N. Sangouard, C. Simon, and N. Gisin, "Telecommunication-Wavelength Solid-State Memory at the Single Photon Level," Physical Review Letters **104**, 080502 (2010).

[45] B. Lauritzen, J. Minář, H. de Riedmatten, M. Afzelius, and N. Gisin, "Approaches for a quantum memory at telecommunication wavelengths," Physical Review A **83**, 012318 (2011).

[46] F. Bussières, C. Clausen, A. Tiranov, B. Korzh, V. B. Verma, S. W. Nam, F. Marsili, A. Ferrier, P. Goldner, H. Herrmann, C. Silberhorn, W. Sohler, M. Afzelius, and N. Gisin, "Quantum teleportation from a telecom-wavelength photon to a solid-state quantum memory," Nature Photonics **8**, 775 (2014).

[47] M. Lovrić, P. Glasenapp, and D. Suter, "Spin hamiltonian characterization and refinement for Pr^{3+}:$YAlO_3$ and Pr^{3+}:Y_2SiO_5," Physical Review B **85**, 014429 (2012).

[48] F. Könz, Y. Sun, C. W. Thiel, R. L. Cone, R. W. Equall, R. L. Hutcheson, and R. M. Macfarlane, "Temperature and concentration dependence of optical dephasing, spectral-hole lifetime, and anisotropic absorption in Eu^{3+}:Y_2SiO_5," Physical Review B **68**, 085109 (2003).

[49] J. J. Longdell, M. J. Sellars, and N. B. Manson, "Hyperfine interaction in ground and excited states of praseodymium-doped yttrium orthosilicate," Physical Review B **66**, 035101 (2002).

[50] M. Lovrić, P. Glasenapp, D. Suter, B. Tumino, A. Ferrier, P. Goldner, M. Sabooni, L. Rippe, and S. Kröll, "Hyperfine characterization and spin coherence lifetime extension in Pr^{3+}:$La_2(WO_4)_3$," Physical Review B **84**, 104417 (2011).

[51] P. C. Hansen, M. J. M. Leask, B. M. Wanklyn, Y. Sun, R. L. Cone, and M. M. Abraham, "Spectral hole burning and optically detected nuclear quadrupole resonance in flux-grown stoichiometric europium vanadate crystals," Physical Review B **56**, 7918 (1997).

[52] J. J. Longdell, A. L. Alexander, and M. J. Sellars, "Characterization of the hyperfine interaction in europium-doped yttrium orthosilicate and europium chloride hexahydrate," Physical Review B **74**, 195101 (2006).

[53] J. J. Longdell and M. J. Sellars, "Experimental demonstration of quantum-state tomography and qubit-qubit interactions for rare-earth-metal-ion-based solid-state qubits," Physical Review A **69**, 032307 (2004).

[54] L. Rippe, M. Nilsson, S. Kröll, R. Klieber, and D. Suter, "Experimental demonstration of efficient and selective population transfer and qubit distillation in a rare-earth-metal-ion-doped crystal," Physical Review A **71**, 062328 (2005).

[55] J. H. Wesenberg, K. Mølmer, L. Rippe, and S. Kröll, "Scalable designs for quantum computing with rare-earth-ion-doped crystals," Physical Review A **75**, 012304 (2007).

[56] A. Walther, B. Julsgaard, L. Rippe, Y. Ying, S. Kröll, R. Fisher, and S. Glaser, "Extracting high fidelity quantum computer hardware from random systems," Physica Scripta **2009**, 014009 (2009).

[57] I. Roos and K. Mølmer, "Quantum computing with an inhomogeneously broadened ensemble of ions: Suppression of errors from detuning variations by specially adapted pulses and coherent population trapping," Physical Review A **69**, 022321 (2004).

[58] N. Ohlsson, R. Krishna Mohan, and S. Kröll, "Quantum computer hardware based on rare-earth-ion-doped inorganic crystals," Optics Communications **201**, 71 (2002).

[59] R. L. Ahlefeldt, D. L. McAuslan, J. J. Longdell, N. B. Manson, and M. J. Sellars, "Precision Measurement of Electronic Ion-Ion Interactions between Neighboring Eu^{3+} Optical Centers," Physical Review Letters **111**, 240501 (2013).

[60] R. L. Ahlefeldt, W. D. Hutchison, N. B. Manson, and M. J. Sellars, "Method for assigning satellite lines to crystallographic sites in rare-earth crystals," Physical Review B **88**, 184424 (2013).

[61] C. Yin, M. Rancic, G. G. de Boo, N. Stavrias, J. C. McCallum, M. J. Sellars, and S. Rogge, "Optical addressing of an individual erbium ion in silicon," Nature **497**, 91 (2013).

[62] T. Damhus, R. M. Hartshorn, and A. T. Hutton, *Nomenclature of inorganic chemistry: IUPAC recommendations 2005* (Royal Society of Chemistry, 2005).

[63] K. W. H. Stevens, "Matrix Elements and Operator Equivalents Connected with the Magnetic Properties of Rare Earth Ions," Proceedings of the Physical Society. Section A **65**, 209 (1952).

[64] B. R. Judd, *Operator techniques in atomic spectroscopy*, Vol. 963 (McGraw-Hill New York, 1963).

[65] B. G. Wybourne, *Spectroscopic properties of rare earths* (Interscience Publishers, 1965).

[66] G. H. Dieke and H. Crosswhite, *Spectra and energy levels of rare earth ions in crystals* (Interscience Publishers, 1968).

[67] W. T. Carnall, G. L. Goodman, K. Rajnak, and R. S. Rana, "A systematic analysis of the spectra of the lanthanides doped into single crystal LaF_3," The Journal of Chemical Physics **90**, 3443 (1989).

[68] R. Withnall and J. Silver, "Physics of Light Emission from Rare-Earth Doped Phosphors," in *Handbook of Visual Display Technology*, edited by J. Chen, W. Cranton, and M. Fihn (Springer Berlin Heidelberg, 2012).

[69] M. Weissbluth, *Atoms and molecules* (Academic Press, 1978).

[70] M. Teplov, "Proton magnetic resonance in thulium ethyl sulfate," Soviet Physics JETP **28**, 872 (1969).

[71] G. F. Koster and H. Statz, "Method of Treating Zeeman Splittings of Paramagnetic Ions in Crystalline Fields," Physical Review **113**, 445 (1959).

[72] B. Henderson and G. Imbush, *Optical Interaction of Inorganic Solids* (Clarendon Press, Oxford, 1989).

[73] G. Liu and B. Jacquier, *Spectroscopic properties of rare earths in optical materials*, Vol. 83 (Springer Science & Business Media, 2006).

[74] A. Abragam and B. Bleaney, *Electron paramagnetic resonance of transition ions* (Oxford University Press, 2012).

[75] G. Liu, "Electronic Energy Level Structure," in *Spectroscopic Properties of Rare Earths in Optical Materials*, edited by G. Liu and B. Jacquier (Springer Science & Business Media, 2006).

[76] A. R. Edmonds, *Angular momentum in quantum mechanics* (Princeton University Press, 1996).

[77] C. Nielson and G. F. Koster, *Spectroscopic Coefficients for the p^n, d^n, and f^n Configurations* (MIT press, 1963).

[78] M. F. Reid, "Transition Intensities," in *Spectroscopic Properties of Rare Earths in Optical Materials*, edited by G. Liu and B. Jacquier (Springer Science & Business Media, 2006).

[79] M. F. Reid and F. S. Richardson, "Electric dipole intensity parameters for lanthanide 4f → 4f transitions," The Journal of Chemical Physics **79**, 5735 (1983).

[80] "Hannah crosswhite's fortran code and data files," `http://chmwls.chm.anl.gov/downloads/`, accessed: 2016-03-31.

[81] W. T. Carnall, H. Crosswhite, H. M. Crosswhite, and J. G. Conway, "Energy level analysis of Pm^{3+}:$LaCl_3$," The Journal of Chemical Physics **64**, 3582 (1976).

[82] S. v. d. Walt, S. C. Colbert, and G. Varoquaux, "The NumPy Array: A Structure for Efficient Numerical Computation," Computing in Science Engineering **13**, 22 (2011).

[83] J. D. Hunter, "Matplotlib: A 2d Graphics Environment," Computing in Science Engineering **9**, 90 (2007).

[84] S. Behnel, R. Bradshaw, C. Citro, L. Dalcin, D. S. Seljebotn, and K. Smith, "Cython: The Best of Both Worlds," Computing in Science Engineering **13**, 31 (2011).

[85] "Compressed row storage, Netlib," http://netlib.org/linalg/html_
      templates/node91.html#SECTION0093110000000000000, accessed:
      2016-01-19.

[86] J. E. Hopcroft and R. E. Tarjan, "Efficient algorithms for graph manipula-
      tion," Tech. Rep. (Stanford, CA, USA, 1971).

[87] "OpenMP application program interface version 3.0," http://www.
      openmp.org/mp-documents/spec30.pdf, accessed: 2016-01-19.

[88] E. Anderson, Z. Bai, C. Bischof, S. Blackford, J. Demmel, J. Don-
      garra, J. Du Croz, A. Greenbaum, S. Hammarling, A. McKenney, and
      D. Sorensen, *LAPACK Users' Guide*, 3rd ed. (Society for Industrial and
      Applied Mathematics, Philadelphia, PA, 1999).

[89] E. Gabriel, G. E. Fagg, G. Bosilca, T. Angskun, J. J. Dongarra, J. M.
      Squyres, V. Sahay, P. Kambadur, B. Barrett, A. Lumsdaine, R. H. Castain,
      D. J. Daniel, R. L. Graham, and T. S. Woodall, "Open MPI: Goals, concept,
      and design of a next generation MPI implementation," in *Proceedings, 11th
      European PVM/MPI Users' Group Meeting* (Budapest, Hungary, 2004) pp.
      97–104.

[90] D. J. Wales and J. P. K. Doye, "Global optimization by basin-hopping and
      the lowest energy structures of lennard-jones clusters containing up to 110
      atoms," The Journal of Physical Chemistry A **101**, 5111 (1997).

[91] D. J. Wales and H. A. Scheraga, "Global optimization of clusters, crystals,
      and biomolecules," Science **285**, 1368 (1999).

[92] N. Metropolis, A. W. Rosenbluth, M. N. Rosenbluth, A. H. Teller, and
      E. Teller, "Equation of State Calculations by Fast Computing Machines,"
      The Journal of Chemical Physics **21**, 1087 (1953).

[93] B. Gough, *GNU Scientific Library Reference Manual*, 3rd ed. (Network
      Theory Ltd., 2009).

[94] S. G. Johnson, "The NLopt nonlinear-optimization package," http://
      ab-initio.mit.edu/nlopt.

[95] L. Van Pieterson, M. F. Reid, R. T. Wegh, S. Soverna, and A. Meijerink, "$4f^n \rightarrow 4f^{n-1}5d$ transitions of the light lanthanides: Experiment and theory," Physical Review B **65**, 045113 (2002).

[96] J. Verweij, C. Pedrini, D. Bouttet, C. Dujardin, H. Lautesse, and B. Moine, "Fluorescence of Ce^{3+} in $LiReF_4$ (RE = Gd, Yb)," Optical Materials **4**, 575 (1995).

[97] V. Pavlov, M. Marisov, V. Semashko, A. Nizamutdinov, L. Nurtdinova, and S. Korableva, "A new technique of the excited-state photoionization studies in $Ce:LiYF_4$ and $Ce:LiLuF_4$ crystals," Journal of Luminescence **133**, 73 (2013).

[98] F. Okada, S. Togawa, K. Ohta, and S. Koda, "Solid-state ultraviolet tunable laser: A Ce^{3+} doped $LiYF_4$ crystal," Journal of applied physics **75**, 49 (1994).

[99] C. Combes, P. Dorenbos, C. Van Eijk, C. Pedrini, H. Den Hartog, J. Gesland, and P. Rodnyi, "Optical and scintillation properties of Ce^{3+} doped $LiYF_4$ and $LiLuF_4$ crystals," Journal of luminescence **71**, 65 (1997).

[100] P. S. Peijzel, P. Vergeer, A. Meijerink, M. F. Reid, L. A. Boatner, and G. W. Burdick, "$4f^{n-1}5d \rightarrow 4f^n$ emission of Ce^{3+}, Pr^{3+}, Nd^{3+}, Er^{3+} and Tm^{3+} in $LiYF_4$ and YPO_4," Physical Review B **71**, 045116 (2005).

[101] T. Yosida, M. Yamaga, D. Lee, T. Han, H. Gallagher, and B. Henderson, "The electron spin resonance and optical spectra of Ce^{3+} in $LiYF_4$," Journal of Physics: Condensed Matter **9**, 3733 (1997).

[102] G. F. Koster, *Properties of the thirty-two point groups*, Vol. 24 (The MIT Press, 1963).

[103] J.-P. R. Wells, M. Yamaga, T. P. J. Han, H. G. Gallagher, and M. Honda, "Polarized laser excitation, electron paramagnetic resonance, and crystal-field analyses of Sm^{3+}-doped $LiYF_4$," Physical Review B **60**, 3849 (1999).

[104] S. A. Miller, H. E. Rast, and H. H. Caspers, "Lattice Vibrations of $LiYF_4$," The Journal of Chemical Physics **52**, 4172 (1970).

[105] A. Ellens, H. Andres, M. L. H. ter Heerdt, R. T. Wegh, A. Meijerink, and G. Blasse, "Spectral-line-broadening study of the trivalent lanthanide-ion series.II. The variation of the electron-phonon coupling strength through the series," Physical Review B **55**, 180 (1997).

[106] L. Esterowitz, F. J. Bartoli, R. E. Allen, D. E. Wortman, C. A. Morrison, and R. P. Leavitt, "Energy levels and line intensities of Pr^{3+} in $LiYF_4$," Physical Review B **19**, 6442 (1979).

[107] L. van Pieterson, M. F. Reid, R. T. Wegh, S. Soverna, and A. Meijerink, "$4f^n \rightarrow 4f^{n-1}5d$ transitions of the light lanthanides: Experiment and theory," Physical Review B **65**, 045113 (2002).

[108] Y. Mei, W.-C. Zheng, and Y.-G. Yang, "Studies of the crystal field energy levels and g factors for Ce^{3+} in $LiYF_4$ crystal," Optik - International Journal for Light and Electron Optics **124**, 3949 (2013).

[109] M. J. Weber and R. W. Bierig, "Paramagnetic Resonance and Relaxation of Trivalent Rare-Earth Ions in Calcium Fluoride. I. Resonance Spectra and Crystal Fields," Physical Review **134**, A1492 (1964).

[110] C. A. Freeth and G. D. Jones, "Zeeman infrared spectra of calcium and strontium fluoride crystals containing cerium and neodymium," Journal of Physics C: Solid State Physics **15**, 6833 (1982).

[111] J.-P. R. Wells and R. J. Reeves, "Polarized laser-selective excitation and Zeeman infrared absorption of Sm^{3+} centers in CaF_2 and SrF_2 crystals," Physical Review B **61**, 13593 (2000).

[112] H. K. Welsh, "Dielectric relaxation in defect clusters in calcium fluoride doped with trivalent rare earths," Journal of Physics C: Solid State Physics **18**, 5637 (1985).

[113] M. Yamaga, S. Yabashi, Y. Masui, M. Honda, H. Takahashi, M. Sakai, N. Sarukura, J. P. R. Wells, and G. D. Jones, "Optical, infrared and EPR spectroscopy of CaF_2:Ce^{3+} crystals co-doped with Li^+ or Na^+," Journal of Luminescence **108**, 307 (2004).

[114] M. Yamaga, M. Honda, N. Kawamata, K. Samejima, and J.-P. R. Wells, "The role of Li^+ and Na^+ charge compensators in Sm^{3+}-doped CaF_2 and SrF_2," in *EPR in the 21st Century*, edited by A. Kawamori, J. Yamauchi, and H. Ohta (Elsevier Science B.V., Amsterdam, 2002) pp. 201–206.

[115] G. Audi, O. Bersillon, J. Blachot, and A. H. Wapstra, "The Nubase evaluation of nuclear and decay properties," Nuclear Physics A The 2003 NUBASE and Atomic Mass Evaluations, **729**, 3 (2003).

[116] C. Li, C. Wyon, and R. Moncorge, "Spectroscopic properties and fluorescence dynamics of Er^{3+} and Yb^{3+} in Y_2SiO_5," IEEE Journal of Quantum Electronics **28**, 1209 (1992).

[117] J. L. Doualan, C. Labbe, P. L. Boulanger, J. Margerie, R. Moncorge, and H. Timonen, "Energy levels of the laser active Er^{3+} ion in each of the two crystallographic sites of yttrium orthosilicate," Journal of Physics: Condensed Matter **7**, 5111 (1995).

[118] R. M. Macfarlane, T. L. Harris, Y. Sun, R. L. Cone, and R. W. Equall, "Measurement of photon echoes in $Er:Y_2SiO_5$ at 1.5 μm with a diode laser and an amplifier," Optics Letters **22**, 871 (1997).

[119] T. Böttger, C. W. Thiel, Y. Sun, and R. L. Cone, "Optical decoherence and spectral diffusion at 1.5 μm in $Er^{3+}:Y_2SiO_5$ versus magnetic field, temperature, and Er^{3+} concentration," Physical Review B **73**, 075101 (2006).

[120] S. R. Hastings-Simon, B. Lauritzen, M. U. Staudt, J. L. M. van Mechelen, C. Simon, H. de Riedmatten, M. Afzelius, and N. Gisin, "Zeeman-level lifetimes in $Er^{3+}:Y_2SiO_5$," Physical Review B **78**, 085410 (2008).

[121] B. Maksimov, V. Ilyukhin, Y. A. Kharitonov, and N. Belov, "Crystal structure of yttrium oxyorthosilicate $Y_2O_3 \cdot SiO_2 = Y_2SiO_5$," Kristallografiya **15**, 926 (1970), Soviet Physics Crystallography **15**, 806 (1971).

[122] "New X-Ray Powder Diffraction Patterns from the JCPDS Associateship," Powder Diffraction **1**, 77 (1986).

[123] The HDF Group, "Hierarchical Data Format, version 5," (1997-NNNN), http://www.hdfgroup.org/HDF5/.

[124] G. C. Bjorklund, "Frequency-modulation spectroscopy: a new method for measuring weak absorptions and dispersions," Optics Letters **5**, 15 (1980).

[125] G. C. Bjorklund, M. D. Levenson, W. Lenth, and C. Ortiz, "Frequency modulation (FM) spectroscopy," Applied Physics B **32**, 145 (1983).

[126] M. Cardona, F. Seitz, D. Turnbull, and H. Ehrenreich, *Solid State Physics: Advances in Research and Applications. Modulation Spectroscopy. Supplement 11* (Academic Press, 1969).

[127] M. Gehrtz, E. A. Whittaker, and G. C. Bjorklund, "Quantum-limited laser frequency-modulation spectroscopy," Journal of the Optical Society of America B **2**, 1510 (1985).

[128] R. M. Macfarlane, "Optical Spectral Linewidths in Solids," in *Lasers, spectroscopy and new ideas: a tribute to Arthur L. Schawlow*, edited by W. M. Yen and M. D. Levenson (Springer, 1987).

[129] R. M. Macfarlane, "Inhomogeneous broadening of spectral lines in doped insulators," Journal of Luminescence **45**, 1 (1990).

[130] R. M. Macfarlane and J. C. Vial, "Spectral hole burning by population storage in Zeeman sublevels of $LaF_3:Nd^{3+}$," Physical Review B **36**, 3511 (1987).

[131] R. Wannemacher, R. S. Meltzer, and R. M. Macfarlane, "Time-resolved spectral holeburning in $LaF_3:Ho^{3+}$ and $YLiF_4:Er^{3+}$," Journal of Luminescence **45**, 307 (1990).

[132] D. M. Boye, R. M. Macfarlane, Y. Sun, and R. S. Meltzer, "Spectral hole burning of Eu^{2+} in CaF_2," Physical Review B **54**, 6263 (1996).

[133] G. K. Liu, J. Huang, R. L. Cone, and B. Jacquier, "Spectral hole burning, Zeeman effect, and hyperfine structure for $Tb^{3+}:LiYF_4$," Physical Review B **38**, 11061 (1988).

[134] B. S. Ham, S. M. Shahriar, and P. R. Hemmer, "Electromagnetically induced transparency over spectral hole-burning temperature in a rare-earth–doped solid," Journal of the Optical Society of America B **16**, 801 (1999).

[135] M. Afzelius, M. U. Staudt, H. de Riedmatten, N. Gisin, O. Guillot-Noël, P. Goldner, R. Marino, P. Porcher, E. Cavalli, and M. Bettinelli, "Efficient optical pumping of Zeeman spin levels in Nd^{3+}:YVO_4," Journal of Luminescence Special Issue based on the Proceedings of the Tenth International Meeting on Hole Burning, Single Molecule, and Related Spectroscopies: Science and Applications - Issue dedicated to Ivan Lorgere and Oliver Guillot-Noel, **130**, 1566 (2010).

[136] P. Goldner, Private communication.

[137] J. Wen, C.-K. Duan, L. Ning, Y. Huang, S. Zhan, J. Zhang, and M. Yin, "Spectroscopic Distinctions between Two Types of Ce^{3+} Ions in X2-Y_2SiO_5: A Theoretical Investigation," The Journal of Physical Chemistry A **118**, 4988 (2014).

[138] N. I. Agladze and M. N. Popova, "Hyperfine structure in optical spectra of $LiYF_4$-Ho," Solid State Communications **55**, 1097 (1985).

[139] N. I. Agladze, M. N. Popova, G. N. Zhizhin, V. J. Egorov, and M. A. Petrova, "Isotope structure in optical spectra of $LiYF_4$:Ho^{3+}," Physical Review Letters **66**, 477 (1991).

[140] J.-P. R. Wells, G. D. Jones, M. F. Reid, M. N. Popova, and E. P. Chukalina, "Hyperfine patterns of infrared absorption lines of Ho^{3+} C_{4v} centres in CaF_2," Molecular physics **102**, 1367 (2004).

[141] D. S. Pytalev, E. P. Chukalina, M. N. Popova, G. S. Shakurov, B. Z. Malkin, and S. L. Korableva, "Hyperfine interactions of Ho^{3+}:KY_3F_{10}: Electron paramagnetic resonance and optical spectroscopy studies," Physical Review B **86**, 115124 (2012).

[142] M. Mujaji and J.-P. R. Wells, "Spectroscopy and crystal-field analysis of KY_3F_{10}:Ho^{3+}," Journal of Physics: Condensed Matter **21**, 255402 (2009).

[143] A. Grzechnik, J. Nuss, K. Friese, J.-Y. Gesland, and M. Jansen, "Refinement of the crystal structure of potassium triyttrium decafluoride, KY_3F_{10}," Zeitschrift für Kristallographie-New Crystal Structures **217**, 460 (2002).

[144] A. Kaminskii, *Crystalline Lasers: Physical Processes and Operating Schemes* (CRC Press, 1996).

[145] J. M. F. v. Dijk and M. F. H. Schuurmans, "On the nonradiative and radiative decay rates and a modified exponential energy gap law for 4f–4f transitions in rare-earth ions," The Journal of Chemical Physics **78**, 5317 (1983).

[146] M. F. H. Schuurmans and J. M. F. van Dijk, "On radiative and non-radiative decay times in the weak coupling limit," Physica B+C **123**, 131 (1984).

[147] F. Pellé and F. Auzel, "Saturation effect on multiphonon relaxation rates of rare earth ions in glasses at high excitation power," Journal of Alloys and Compounds **300–301**, 131 (2000).

[148] F. S. Ermeneux, C. Goutaudier, R. Moncorgé, Y. Sun, R. L. Cone, E. Zannoni, E. Cavalli, and M. Bettinelli, "Multiphonon relaxation in YVO_4 single crystals," Physical Review B **61**, 3915 (2000).

[149] G. D. Jones and J.-P. R. Wells, "Picosecond lifetimes and infrared spectroscopy of hydrogenic sites in KY_3F_{10} and $LiYF_4$," Journal of Luminescence Proceedings of the 2002 International Conference on Luminescence and Optical Spectroscopy of Condensed Matter, **102–103**, 169 (2003).

[150] P. C. Findlay, C. R. Pidgeon, R. Kotitschke, A. Hollingworth, B. N. Murdin, C. J. G. M. Langerak, A. F. G. van der Meer, C. M. Ciesla, J. Oswald, A. Homer, G. Springholz, and G. Bauer, "Auger recombination dynamics of lead salts under picosecond free-electron-laser excitation," Physical Review B **58**, 12908 (1998).

[151] C. Görller-Walrand and K. Binnemans, "Handbook on the physics and chemistry of rare earths," North-Holland, Amsterdam , 123 (1998).

[152] C. B. Layne and M. J. Weber, "Multiphonon relaxation of rare-earth ions in beryllium-fluoride glass," Physical Review B **16**, 3259 (1977).

[153] C. B. Layne, W. H. Lowdermilk, and M. J. Weber, "Multiphonon relaxation of rare-earth ions in oxide glasses," Physical Review B **16**, 10 (1977).

[154] Y. V. Orlovskii, R. J. Reeves, R. C. Powell, T. T. Basiev, and K. K. Pukhov, "Multiple-phonon nonradiative relaxation: Experimental rates in fluoride crystals doped with Er^{3+} and Nd^{3+} ions and a theoretical model," Physical Review B **49**, 3821 (1994).

[155] C. Bibeau, S. A. Payne, and H. T. Powell, "Direct measurements of the terminal laser level lifetime in neodymium-doped crystals and glasses," Journal of the Optical Society of America B **12**, 1981 (1995).

[156] B. M. van der Ende, R. L. Brooks, H. F. Tiedje, H. Sun, and H. K. Haugen, "Measurement of the $^4F_{5/2}$ and $^2H(2)_{9/2}$ manifold lifetime in Nd^{3+}:$YLiF_4$," Journal of Luminescence **117**, 13 (2006).

[157] Y. V. Orlovskii, K. K. Pukhov, T. T. Basiev, and T. Tsuboi, "Nonlinear mechanism of multiphonon relaxation of the energy of electronic excitation in optical crystals doped with rare-earth ions," Optical Materials **4**, 583 (1995).

[158] E. Cohen and H. W. Moos, "Vibronic Transitions of Hexagonal Rare-Earth Trichlorides. I. Pr^{3+}, and Nd^{3+} in $NdCl_3$," Physical Review **161**, 258 (1967).